Fakultät für Mathematik und
Naturwissenschaften

Bergische Universität Wuppertal

Dissertation
zur Erlangung des Doktorgrades
(Dr. rer. nat.)

Measuring acoustic ice properties for the Enceladus Explorer

Der Fachgruppe Physik vorgelegt von

Ruth Hoffmann

15. Juli 2019

BERGISCHE
UNIVERSITÄT
WUPPERTAL

The PhD thesis can be quoted as follows:

urn:nbn:de:hbz:468-20200902-094503-5
[http://nbn-resolving.de/urn/resolver.pl?urn=urn%3Anbn%3Ade%3Ahbz%3A468-20200902-094503-5]

DOI: 10.25926/009b-6y76
[https://doi.org/10.25926/009b-6y76]

Contents

List of Figures

List of Tables

Chapter 1

Introduction

The search for extraterrestrial life is one of the most interesting challenges of our time. The discovery of life on another planet or moon would change our view of the world forever. Even proving the existence of microbiological life on a different celestial body would be a huge step towards answering questions about the origin and development of life as well as how rare life really is. Within our solar system there are very few places which are promising places to search for life. One of them is Saturn's moon Enceladus.

As early as 1981 the Voyager 2 mission captured the first high resolution pictures of Enceladus' surface and discovered that its South polar region showed fewer impact craters than its northern hemisphere. An effect which is likely caused by geological activity resulting in fresh snow which covers the craters in the southern regions [8].
The south polar region is also where the so called "Tiger stripes" are located. For further exploration of these four, nearly parallel linear 130 km long crevasses, Cassini performed several close flybys starting in 2005 to take more detailed pictures [9]. Thermal images show that the "Tiger stripes" are warmer than the surrounding ice. Supposedly, this heat is transported through the crevasses from a liquid subsurface ocean to the surface [3]. This theory is supported by the active cryovolcanism in that region which can be seen in the form of about 100 jets with heights of up to 400 km, which originate in the "Tiger stripes" [3]. Currently, the energy source for the ocean is thought to be a combination of tidal forces and radiogenic effects [10, 11]. In March 2008 a flyby through one of the plumes made also a composition analysis of the ejected material and revealed the presence of organic molecules in the jets [12].
So despite its distance from the sun and beeing only 504 km in diameter, Enceladus is very geologically active and in possession of a salt water ocean around its core, which potentially provides acceptable conditions for the development of alien bacteria [13].
A much more detailed exploration of this ocean could be achieved by sending a lander to Enceladus. The feasibility of such a mission and the development of the technology necessary is the purpose of the Enceladus Explorer (EnEx) initiative of the German Aerospace Center (Deutsches Zentrum für Luft- und Raumfahrt DLR).

In a lander mission to Enceladus, the spacecraft would land close to the "Tiger stripes" and then deploy a probe at its landing site which would melt into the ice. The probe would approach the crevasse, take a sample of the liquid before it freezes and do some in-situ microbiological analysis. Critical to such a mission are both, a clean sampling method to avoid contamination of the water reservoir or the taken sample and a maneuverable probe. That probe needs to be able to avoid possible obstacles on its way and also to recognize the crevasse before reaching it. Due to the low data rate between Earth and Enceladus and the time delay of 70 to 90 minutes, the probe also needs to be

autonomous [14]. In order to reach these goals a suitable positioning system is required, one of these is the acoustic positioning system (APS).
The main operating principle of the acoustic positioning system is trilateration. To do this tranducers are deployed at known locations distributed over the surface of the site and the probe is equipped with multiple receivers. The distances between the probe and the transducers are then calculated from the known speed of sound of the ice and the measured propagation times between transducers and receivers. For this method to work, a sufficiently long range of the acoustic signals has to be ensured, which can be limited through attenuation or by cracks in the ice. Additionally in order to reach the required precision of the probes position, a very accurate time measurement and a good understanding of possible variations of the speed of sound is required.

The efforts taken to improve the understanding of the properties of the ice are the main focus of this thesis. A more detailed description of the scenario on Enceladus and an overview of the complete mission concept are given in Chapter 2, along with a description of the technical aspects of the APS. An estimation of the influence of possible uncertainty sources can be found in Chapter 3. This is followed by a short description of the theory of acoustic wave propagation, attenuation, generation and detection in Chapter 4. Chapter 5 describes the various test campaigns performed throughout the project. The focus of Chapter 6 is on the measurements performed to improve the understanding of the system's properties, such as the comparison of different transducers, the characterization of the electronics, a comparison between the receivers in the IceMole-Head and the influence of the coupling between the transducers and ice. In Chapter 7 an analysis of the ice properties can be found, with a description of the data processing, followed by a section on the influence of cracks. Afterwards different methods for determining the sound speed with results is given. The chapter closes with an analysis on acoustic attenuation in ice. The results are then summarized in Chapter 8.

Chapter 2

Enceladus Explorer

The Enceladus Explorer project is a feasibility study on the search for extraterrestrial life on Saturn's moon Enceladus. Its main goal is the development of the technology for a mission to Enceladus with a special focus on in-ice navigation solutions.
The core componet of the lander design is a minimal invasive system, that is able to autonomously drill its way through ice, find an active crevasse and take a sample to be analyzed inside the probe.

2.1 Search for extraterrestrial life

Already in the antique people have been thinking about the possibility of life on other celestial bodies [15]. Since the first exoplanet was discovered in 1992, hundreds more have been found motivating further speculation about alien life [16, 17].
There are currently three methods beeing explored in the search for extraterrestrial life. The first is to look for signs of extraterrestrial technology like the SETI project (Search for Extra Terrestrial Intelligence) has been doing since 1960 [18]. The second is the examination of planetary atmospheres for evidence of chemical signatures, e.g. like the JWST (James Webb Space Telescope) is planing to do [19]. The last is to send a space mission to search in situ, which also offers the option of returning samples to Earth [20]. At the moment, this is only possible for clestial bodies within our solar system, e.g. Enceladus.
For the two last options, a critical requirement is a scientific definition of life itself, and of what is required for the development and survival of life in order to pick promising locations in which to search. However, until now an explicit definition which includes all life forms one could think of has not been agreed upon yet. This is the reason most experiments to date search for "life as we know it" instead of a more general approach. This means, they search for life that is similar to that observed on Earth and is therfore carbon based.
Conventionally astrobiologists speak of four requirements for "life as we know it":

- chemical building blocks,
- liquid medium,
- energy,
- stability.

The chemical building blocks for life on earth are carbon, nitrogen, oxygen and hydrogen. These atoms are able to form single, double, triple and quadrupole chemical bonds making complex chemistry possible. Although there are other elements in the periodic table which are able to form the same number of chemical bonds (e.g. silicon instead of

carbon) there seems to be no other combination so well suited for the development of life due to various reasons. Silicon for example does not form double bonds as readily as carbon and it converges to glass (SiO_2) when in contact with oxygen. Other elements like phosphorus and sulfur do not have the right aggregation state in a reasonable temperature range (below 100 °C) [21].
In order to build an organism from the molecules formed out of the elements above, a medium (liquid) is needed in which the molecules can be transported. Moreover, life requires a liquid as a mediator for its chemical reactions. On Earth water in its liquid state fulfills the task of the medium and of the mediator, but in general there are other options like ammonia, methane or ethane.
All life forms need an energy source of some kind. For life on earth today, that source is mainly the sun. Plants harvest energy from the sunlight and animals eat the plants or one another. The secondary energy source on earth is the result of geothermal activity. Examples are bacteria living in the abyssal zone of the oceans or in volcanoes. For celestial candidates that means they either need to be close enough to a star or they need to be geologically active.
Biologists believe that life on Earth started around 3.8 billion years ago. That means that after the formation of Earth 4.5 billion years ago, it took a few hundred million years for the first bacteria to develop. For this reason, the last requirement for a potential candidate to harbor extraterrestrial life is that it has stable conditions (radiation shielded, constant supply of the first three) for a time period of at least a few tens millions years [22].
According to these requirements, a search for "life as we know it" should focus on planets or moons that posses the right chemical building blocks along with the presence of liquid water. That means celestial bodies which are either positioned within the habitable zone of a star or offer enough energy from geological activity. The habitable zone of a star is defined as the orbital range around a star in which liquid water on an Earth-like planet could occur. Of course that definition does not include all viable options because the surface temperature of a planet or moon does not only depend on its distance from its star and the luminosity of that star, but also on the planets atmosphere, and reflectivity, atmospheric and oceanic circulations and possible geological activity [23]. One example for a candidate outside this habitable zone is Enceladus.

2.2 Enceladus

Enceladus was discovered on the 28th of August in 1789 by William Herschel. It is a moon of Saturn with a small diameter of 504 km and in a close orbit of 238000 km [13]. Because Enceladus surface is covered with water ice, it reflects 99% of sunlight, making it one of the brightest objects in our solar system [24, 25, 26]. This leads to a mean surface temperature of 72 K which is significantly lower than on Saturn's other moons meaning Enceladus should be frozen through.
Yet, the Voyager 2 mission's observation of unexpected surface features indicates geological activity. Currently the best images yet taken of Enceladus surface were recorded by the Cassini-Huygens mission (Figure 2.1). In these one can see large areas without any craters indicating recent ($10^7 - 10^8$ years) geological activity as well as huge ridges and crevasses, especially in the south polar region, where four parallel crevasses are situated forming the so called "Tiger stripes" [27, 28].

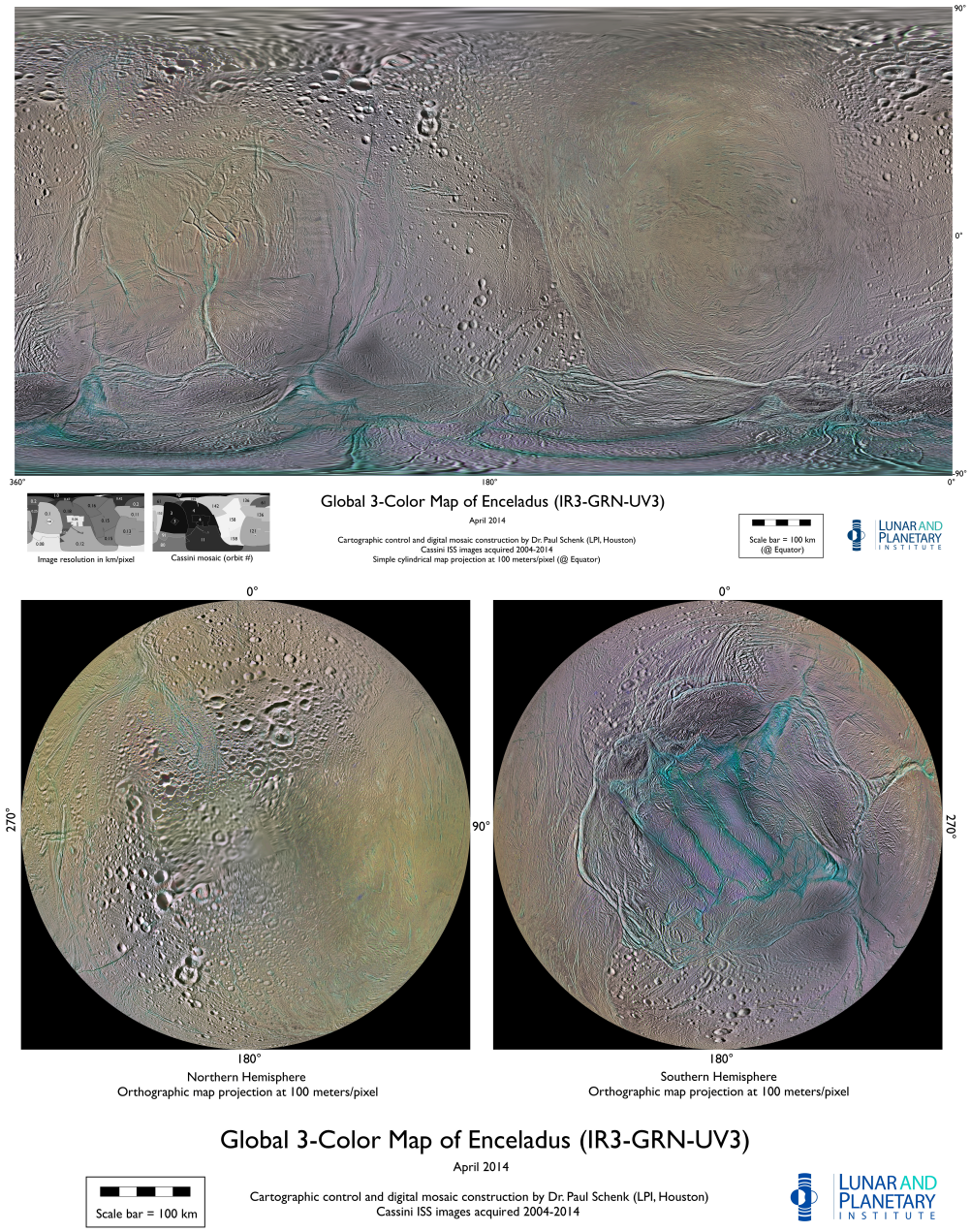

FIGURE 2.1: Global color maps produced from Cassini data with a broad spectrum from infrared to ultraviolet. Yellowish and magenta tones mean differences in surface deposits and blueish areas correspond to stronger ultraviolet signatures, meaning they are brighter [1].

This region is particularly interesting for astrobiology since traces of simple organics and CO2 have been found there [29]. On the images taken by CASSINI's Imaging Science Subsystem (ISS) one can see, that the "Tiger stripes" are linear depressions with a typical dimension of 130 km in length, 500 m in depth and 2 km in width, positioned $\sim$ 35 km from each other [9]. These crevasses are believed to be the origin of the dust ring at the same distance from Saturn as Enceladus called E-ring [30]. On the heat map shown in Figure 2.2, the "Tiger stripes" are recognizable with a temperature of at least 180 K as hot regions when compared to the surrounding ice [2].

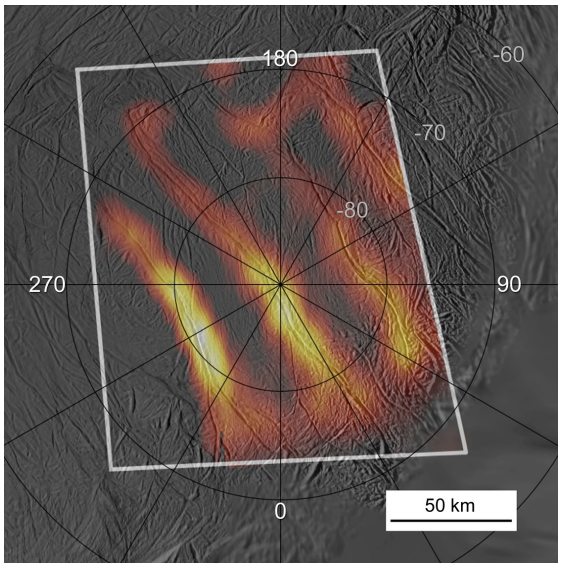

FIGURE 2.2: Heat map of Enceladus south polar region recorded by CASSINIs Composite Infrared Spectrometer on the March 12, 2008 superimposed with an image of Enceladus' surface taken on July 14, 2005 by one of CASSINIs cameras with an infrared scale of $12 - 16$ µm [2].

The reason for the occurrence of these hot crevasses is believed to by cryovolcanism. The current best model for Enceladus can be seen in Figure 2.3, predicting an ocean of salt water situated around Enceladus' rock-core. Due to high eccentricity (0.0047) an close proximity of Enceladus' orbit, the moon is exposed to immense tidal forces which heat up the ice enabling its oceans to stay in the liquid phase. Via cracks, the water can rise through the $30 - 40$ km thick ice layer to the surface where it escapes through the "Tiger stripes" in geysers. Most of the refrozen water then falls back on the surface covering the south polar region with fresh snow and with only ~ 1 % escaping Enceladus' gravity to form the E-ring of Saturn [3].

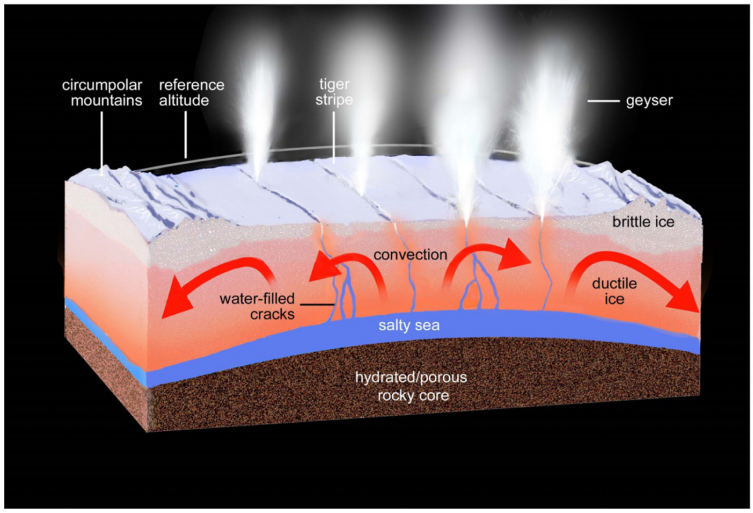

FIGURE 2.3: Visualization of the cold geyser model for Enceladus. The subsurface salty ocean is shown together with the water filled cracks through which the water rises to the surface where it refreezes and evaporates forming the geysers [3].

A composition analysis of the ejected material, also done by Cassini, has shown the presence of the organic molecules in the jets [12]. Overall Enceladus has all the features, that are required for the development of life. In addition, to the relevant chemical building blocks, a stable ocean around its core is present that is heated by a combination of radiogenic effects and tidal forces [10, 11].

2.3 EnEx lander system

The EnEx lander consists of a carrier probe with several subsystems hosted inside along with a number of surface components. On board the probe is a dead reckoning system consisting of an IMU (Inertial Measurement Unit) and a magnetometer, a decontamination system and an acoustic box that contains a reconnaissance system based on sonography and the receiving part of the acoustic positioning system (APS). Situated on the surface is a reference magnetometer, the probe control system and of course the acoustic positioning system beacons.

2.3.1 IceMole

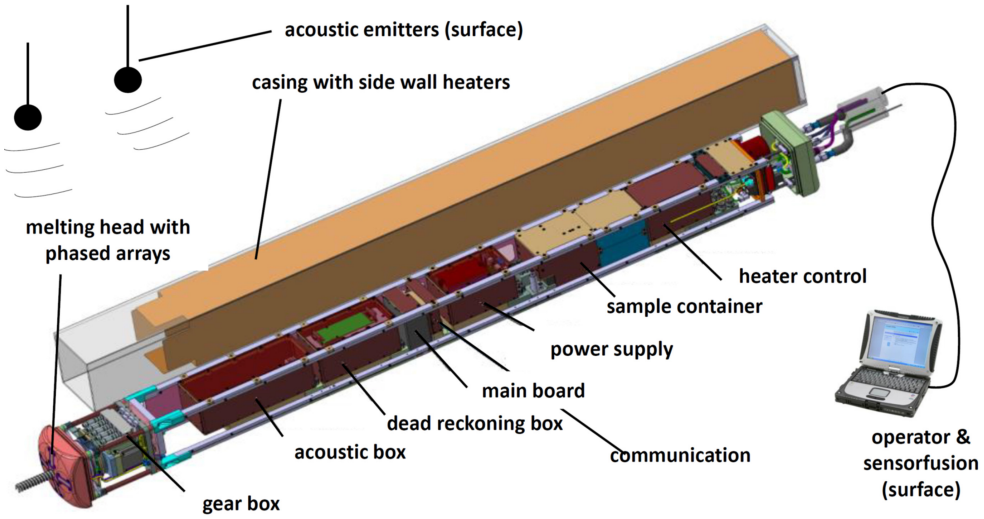

FIGURE 2.4: Overview of the EnEx system including surface components and on board systems. All payload subsystems inside the probe are contained in customized boxes that are easily removable for servicing reasons. All systems essential for operating the probe itself like the heating system, drive and communication and power control are permanently installed in the probe. The connection to the surface consists of a power cable, data cables for communication with the surface control and a water sampling tube. The surface control and the acoustic transmitters are also shown [4].

A sketch of the EnEx lander system is shown in Figure 2.4. The carrier probe, named the IceMole, has a length of 2 m and a quadratic cross-section with an edge length of 15 cm. In total, it weighs $\sim$ 60 kg and is a combination of a conventional melt down probe and a mechanical ice-drill. The melting part it is equipped with 16 heating cartridges arranged in four sets in the head providing a total melting power of 2.88 kW, which results in an average velocity of $\sim$ 1 m/h. Additionally each side of the probe is equipped with one

wall heater to prevent the probe from freezing to the surrounding ice. As can be seen in Figure 2.5, to ensure contact between the probe and the ice, a 6 cm long ice-screw driven by a stopper motor is mounted in the center of the melting head. All heating-sets in the head and each side wall heater are separately adjustable so that through control of the heaters the melting course can be steered with a minimum curve radius of 10 m. Combined with the ice-screw, this steerability enables the probe to drill in every required direction, including even upwards against gravity. The maximum range of the system is currently 40 m, as fixed by the length of the cable between the probe and the surface station [4].

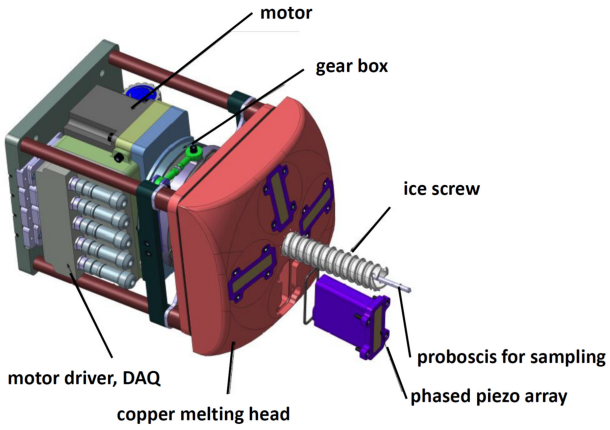

FIGURE 2.5: Sketch of the melting head as a front view [4].

For reasons of planetary protection, the probe is equipped with an in-situ decontamination system. Also since two of the field tests were conducted in Antarctica, this system was also necessary to prevent a contamination of the ecosystems there [31]. Once the probe has reached the target area the remaining melt water is pumped to the surface and the melting channel is flooded with a 3% hydrogen peroxide solution through four orifices in the melting head and the sampling proboscis (see Figure 2.5). After approximately 15 minutes the H_2O_2 has dissolved and the probe is ready to take a sample. To make sure there is no hydrogen peroxide left, before taking a sample into the probe's internal, sterile, gas-tight sample bags, first a brine sample is pumped to the base station at the surface [4].

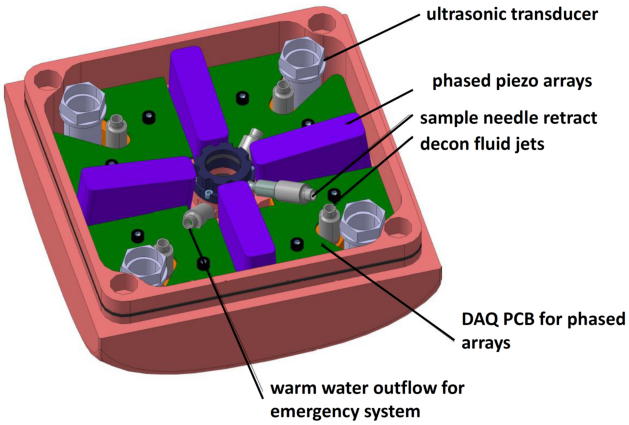

FIGURE 2.6: Sketch of the inside of the melting head [4].

2.3.2 Dead reckoning system

As mentioned earlier, the dead reckoning system uses two independent attitude measurements. One from the Attitude and Heading Reference System (AHRS) which uses an IMU and the other from the comparison of two magnetometers. The IMU and one magnetometer share a compartment in the probe (Figure 2.7) while the other magnetometer is placed on the glaciers surface. For positioning, both independent heading measurements are combined with their individual uncertainties resulting in the drift stabilized attitude of the probe. The distance traveled is determined from the motor steps of the ice screw, the ice screw pitch and the motor gear ratio. Based on this attitude and distance traveled, the position of the probe is predicted. After a long travel distance, the uncertainty on this prediction becomes large as the errors add up over time without regular updates. Therefore, the predicted position is updated with measurements from the APS yielding an improved estimate of the location and orientation of the probe [4].

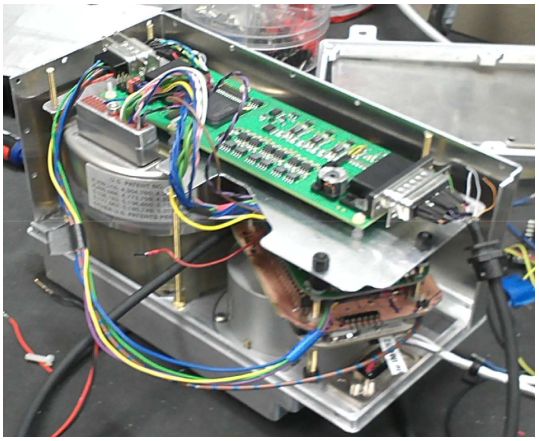

FIGURE 2.7: Magnetometer and IMU assembled in the AHRS compartment including electronics [5].

Due to the spatial limitations and the unusually slow movement of the probe, the Northrop Grumman LN-200 was chosen for the IMU. It uses fiber-optic gyroscopes, has the advantage of being small enough, only 8.89 cm in diameter and 8.51 cm in height, to fit into the probe, and has a precision of $1 - 3°/\text{h}$ even at slow motions [5, 32]. The IMU measures rotation rates and acceleration and then uses this information to propagate the known initial position, velocity and attitude vectors. This means, that its accuracy depends strongly on the precision of the initial position and that its uncertainties on the current position will also increase over time.

Both magnetometers are flux-gate magnetometers with a resolution of 7.75 pT and a range of up to 65 µT (65 µT is larger than the strength of the Earth's magnetic field). Neither the magnetic field on Enceladus nor the Earth's magnetic field close to the South Pole are sufficiently stable and well-known necessitating the use of a reference magnetometer. The requirements on the use of a reference magnetometer are a magnetic clean environment and a stable position at a constant attitude. Durings tests on sunny days, the ice underneath the legs of the reference magnetometer can melt, resulting in a slow tilt which needs to be corrected for. This correction can be achieved by using independent gravity measurements from the IMU. To account for the distortion of the magnetic field inside of the probe due to secondary magnetic fields induced by magnetic materials or electro-magnetic sources, a magnetic baseline model was designed. For

this all known disturbers (e.g. motor, electronic boards) are measured individually in a calibration unit with a clean background and the readings are stored in a matrix. For every state of the probe, the matrices corresponding to the active disturbers are then multiplied and applied to the raw magnetometer data. However, this can only be done for known disturbers and the influence of local sources of magnetic noise remain. During the field test at the Dry Valleys in Antarctica relative variations of 0.1 % were observed over a time period of 8 hours which corresponds to a heading error of 1°.

2.3.3 Acoustic reconnaissance system

Since there are no existing maps of the test area the timely detection of crevasses and obstacles in the way is a crucial step towards autonomy. The acoustic reconnaissance system (ARS) was build to both provide this information and to find interesting targets in the fore field region. It uses sonography, which is already successfully used for medical applications [33, 34] and material inspection [35]. The system used for EnEx consists of four linear phased arrays each consisting of 16 piezo elements. As can be seen in Figure 2.5 the arrays are arranged crosswise around the ice-screw. They are leaning to the outside with an angle of 7.2° to cover the area in front of the probe. In consideration of the high temperature gradient and the high pressure on the active surface, the array's design differs from that of typical products used for other applications. The placement of the arrays in the IceMole-head the arrays decreases the melting speed. To minimize this influence on the melting performance, the housing of the arrays was made of the same material as the melting head itself. Also to ensure a good coupling between the arrays and the surrounding ice, the active area was made of epoxy resin, with an impedance that matches that of the surrounding ice.
The idea behind the ARS is to use phased acoustic signals to form an directed acoustic beam that is reflected by objects like rocks or water-/air-filled pockets in the ice. The direction and focus of the beam can be adjusted by phase shifts between the individual piezo elements. In one scan each array covers an angular range of ±45° with a step size of 1°. This leads to an overlap of the field of view in front of the probe. The maximum range of the ARS is limited to approximately 15 m. The arrays are operated at their resonance frequency of 780 kHz which is considerably higher than the frequencies used in the APS. This leads to an even higher influence of the acoustic properties of the ice on its results and the expected attenuation is higher than for the APS [5].

2.3.4 Acoustic Positioning System (APS)

The task of the APS is to provide the absolute position of the probe. This is used to update the AHRS and leading to better knowledge of the probes position.

Principle

The operating principle of the APS is shown in Figure 2.8. The idea is to measure the signal propagation times between at least three transducers on the surface of the glacier and the receiver in the probes head. Assuming the speed of sound is known, from these times one can calculate the distance between each transducer and the probe. Since the transducers are located on the glaciers surface their positions are relatively easy to determine. Therefore the absolute position of the probe can be derived from the measured distances using trilateration algorithms.

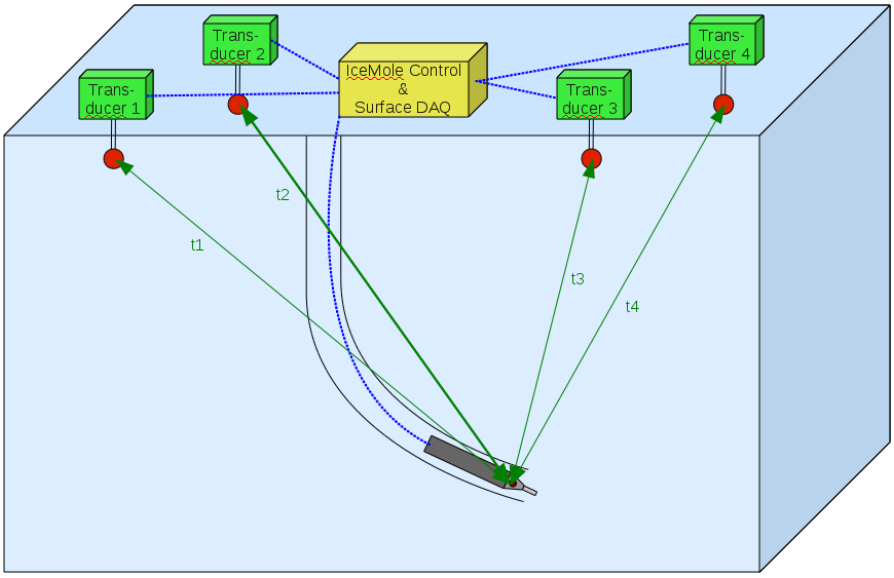

FIGURE 2.8: Principle of the APS. The control system and the DAQ are situated on the surface surrounded by the transducer stations In the ice below is the probe at the end of its melting channel with the receiver in its head.

Transducer system

The first part of the APS is the transducer system. This system is responsible for generating the acoustic pulses that propagate from the surface through the ice to the IceMole. It also provides additional data on the ice quality at the site, such as directional dependencies of the speed of sound or the attenuation length of the acoustic signals using measurements made between the transducers on the surface.

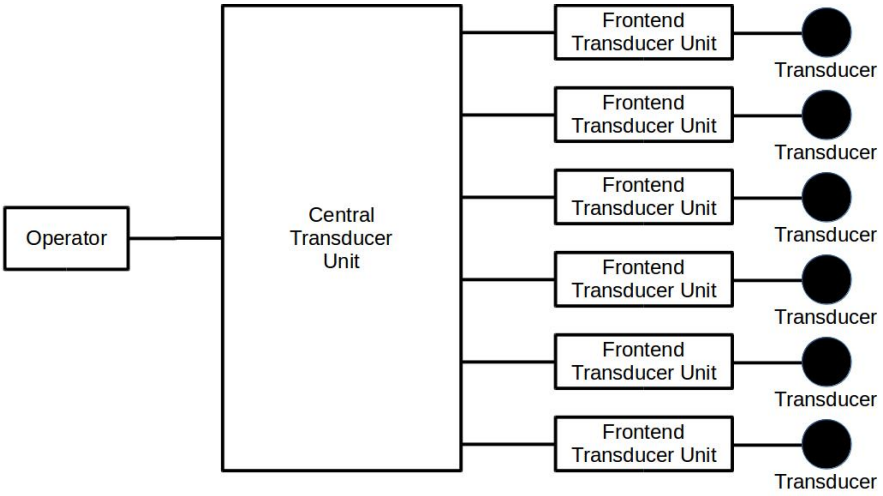

FIGURE 2.9: Structure of the Pinger Module.

The system consists of three components, a Central Transducer Unit (CTU), six Frontend Transducer Units (FTU) and six transducers. A general overview of the system is shown in Figure 2.9. The CTU and the FTUs are located on top of the ice, while the transducers themselves are inserted into the ice at a depth of at least 1 m. The central component of the system is the CTU and the FTUs are then distributed around it via 75 m cables

providing a maximum distance from each other of 150 m. This setup allows for a very flexible transducer array geometry. The transducers are then connected to the FTUs via 3 m long cables.

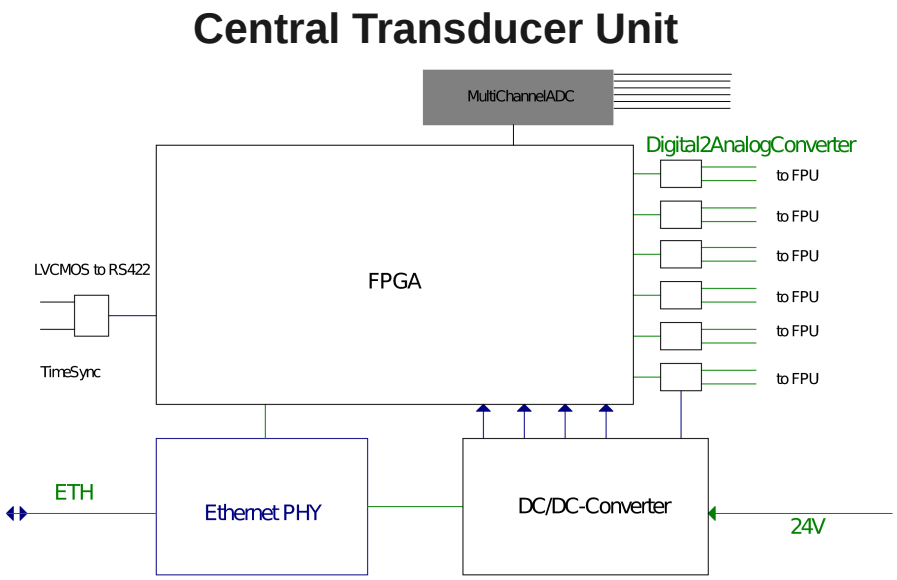

FIGURE 2.10: Schematic of the Central Transducer Unit. [36]

A schematic view of the CTU can be found in Figure 2.10. For data aquisition of the signals received by the transducers the CTU is equipped with a multi channel ADC. An ethernet connection ensures the communication with the probe while the RS422 port is used for time synchronization. A DC/DC converter distributes the 24V, applied from a battery, to the FTUs and also to the field progammable gate array (FPGA). The FPGA (Xilinx Spartan 6) is the central component and is responsible for the generation of the control signals for the transducers. The control signals are then sent through digital-to-analog converters to the FTUs.

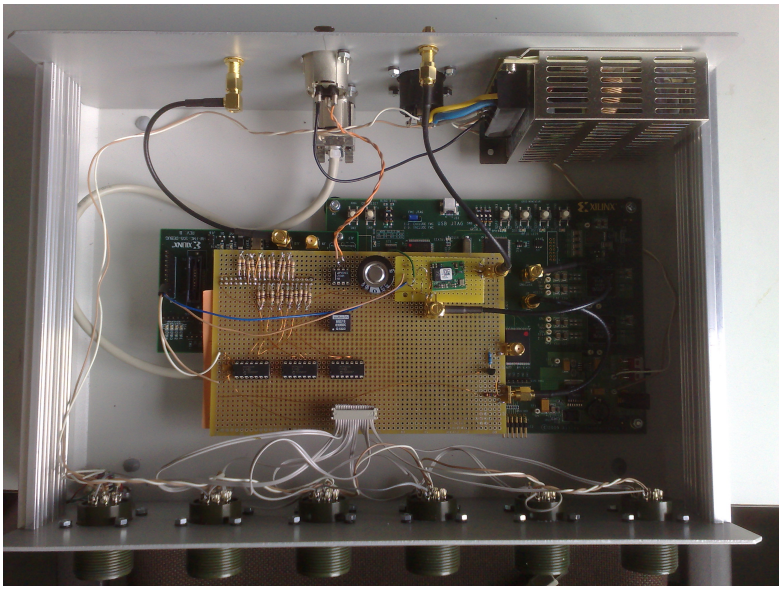

FIGURE 2.11: Photograph of the Central Transducer Unit.

The main tasks of the CTU are to control the transducers at a given time and to provide a synchronization signal for the receiver system in the probe. For the synchronization signal, the FPGA generates a square-wave pulse with an amplitude of 5 V every second and sends this to the data aquisition system of the APS in the probe. From the, by the operator, given length and oscillation period the FPGA generates the control signals for the transducers, which are then send to their respective FTUs. When no control parameters are given, signals with a length of 11 periods and a frequency of 18 kHz are generated and repeated 64 times every 50 ms. In addition, when measuring signals between the transducers at the surface, a trigger signal is also generated.

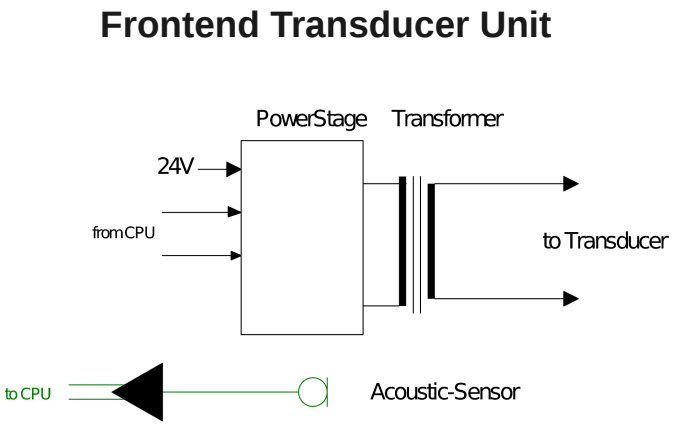

FIGURE 2.12: Schematic of the Frontend Transducer Unit. [36]

The schematic of the FTU is shown in Figure 2.12. It consists of a power stage and a transformer which are used to amplify the control signals from the CTU up to ±75 V before transmitting them to the actual transducer. In addition, it is equipped with an amplifier for receiving signals.

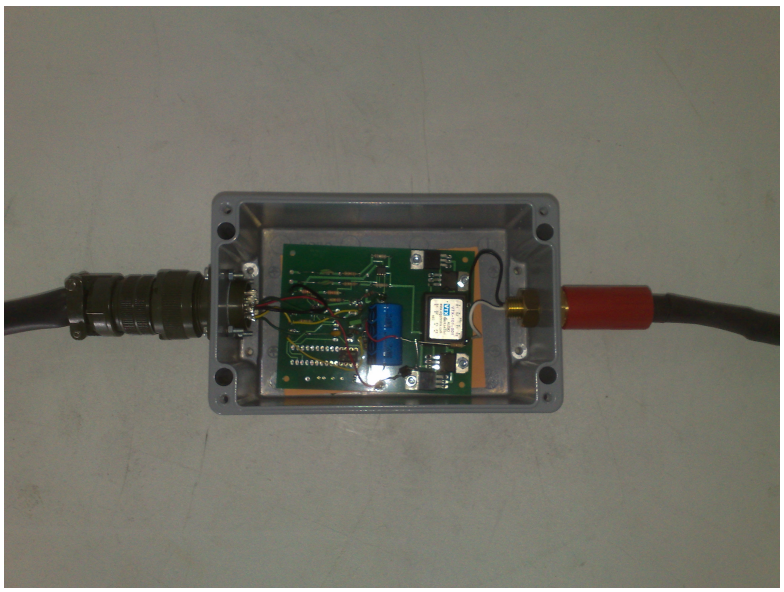

FIGURE 2.13: Photograph of one Frontend Transducer Unit.

The chosen transducer is the ITC-1001, which is a hollow sphere with a diameter of 10 cm which is made out of lead zirconate titanate (PZT) ceramic covered in plastic. A

photograph is shown in Figure 2.14 and more details can be found in Chapter 6.1.

FIGURE 2.14: Photograph of an ITC-1001.

Receiver system

The receiver system consists of four acoustic sensors that are mounted in the probe's head as well as some electronics for readout of the signals. For the sensors, two different designs were evaluated. Both designs consist of a piezo-electrical sound converter which is mounted in a metal housing that is then placed in round depressions on the head each with a diameter of 20 mm. For the actual sound converters, PZT discs with a diameter of 16 mm and a height of 3 mm are used. The resonance frequency of these discs in longitudinal direction is 670 kHz and 125 kHz in transverse direction. For the first design, the disc was glued to the housing. In the later design a screw was used to press the disc to the bottom of the casing.
The electronics of the receiver system are split in two parts. One part is mounted directly behind the sensors in the metal housing and the other is located in the acoustic box installed in the IceMole. The part directly behind the sensors consists of an analoge amplifier followed by a digitalisation module. These modules are then connected to the data aquisition module in the acoustic box, which is also based on a FPGA (Xilinx Spartan 6). The data aquisition module then filters and stores the data locally in RAM before they are sent to the central database at the surface.

Chapter 3

Simulation

To assess the performance of the trilateration algorithm in the phase space of the relevent uncertainties simulation is needed. The algorithm and the testing simulation are described in this chapter.

3.1 Uncertainties on Acoustic Positioning

The main purpose of the simulation was to estimate the influence of uncertainties on the speed of sound, signal propagation time and transducer positions on the absolute positioning of the probe. In addition, it can be used to test different geometric transducer arrangements.

3.1.1 Trilateration

The position of the probe can be found as the intersection point of at least three spheres around the n transducers with radii $d_i(P)$ of the exact distance between each transducer at point $T_i(x_i, y_i, z_i)$ and the probe at location $P(x, y, z)$. These spheres are described by equation 3.1.

$$d_i(P)^2 = (x - x_i)^2 + (y - y_i)^2 + (z - z_i)^2 \tag{3.1}$$

with $\quad i = 1, ..., n$

Since these equations are non-linear but quadratic, simultaneous solving them is not feasible for practical applications. By linearizing the system as described in [37], via the utilization of one transducer as a reference point $R(x_r, y_r, z_r)$, the problem can be solved at the cost of increasing the minimum number of required transducers to four. Equation 3.1 is then changed to:

$$d_i(P)^2 = (x - x_r + x_r - x_i)^2 + (y - y_r + y_r - y_i)^2 + (z - z_r + z_r - z_i)^2.$$

Which can be expressed as:

$$d_i(P)^2 - d_r(P)^2 - d_i(T_r)^2 = 2\left[(x - x_r)(x_r - x_i) + (y - y_r)(y_r - y_i) + (z - z_r)(z_r - z_i)\right] \tag{3.2}$$

In the following simulation, the coordinates (x_i, y_i, z_i) of the transducers are randomized coordinates of transducer i, the distance $d_i(P)$ between transducer i and the probe P is obtained from the randomized speed of sound and the randomized signal propagation time, while the distance $d_i(T_r)$ between the reference transducer and the other transducers is calculated from the randomized transducer coordinates.

Without a loss of generality, transducer 1 can be used as the reference point. That means that equation 3.2 can be written as the linear equation system 3.3

$$\mathbf{A}\widetilde{\mathbf{x}} \approx \mathbf{b}. \tag{3.3}$$

In the case of four transducers the Matrix $\mathbf{A}$ and the vectors $\widetilde{\mathbf{x}}$ and $\mathbf{b}$ are given by the following expressions:

$$\mathbf{A} = \begin{pmatrix} x_1 - x_2 & y_1 - y_2 & z_1 - z_2 \\ x_1 - x_3 & y_1 - y_3 & z_1 - z_3 \\ x_1 - x_4 & y_1 - y_4 & z_1 - z_4 \end{pmatrix}, \quad \widetilde{\mathbf{x}} = \begin{pmatrix} x - x_1 \\ y - y_1 \\ z - z_1 \end{pmatrix}, \quad \mathbf{b} = \begin{pmatrix} b_{21} \\ b_{31} \\ b_{41} \end{pmatrix}$$

with $\quad b_{i1} = \frac{1}{2}\left(d_i(P)^2 - d_1(P)^2 - d_i(T_1)^2\right) \quad (i = 2, 3, 4).$

To minimize the sum of residuals, the normal equation 3.4 can be solved as described in [37]:

$$\mathbf{A}^T\mathbf{A}\widetilde{\mathbf{x}} = \mathbf{A}^T\mathbf{b} \tag{3.4}$$

There are several methods for solving this equation. In this work QR-decomposition was chosen, because it is quite possible that $\mathbf{A}^T\mathbf{A}$ may become singular or ill-conditioned. After calculating the QR-decomposition of $\mathbf{A}$ using Householder transformations, equation 3.3 is equivalent to 3.5 and $\widetilde{\mathbf{x}}$ can be determined via substitution.

$$\mathbf{R}\widetilde{\mathbf{x}} = \mathbf{Q}\mathbf{b} \tag{3.5}$$

with $\quad \mathbf{A} = \mathbf{QR},$

where $\mathbf{Q}$ is a orthonormal $(n-1)\times(n-1)$ matrix and $\mathbf{R}$ is an upper triangular $(n-1)\times 3$ matrix. The absolute position of the probe can then be calculated from $\widetilde{\mathbf{x}}$ by adding the coordinates of the reference transducer.

3.1.2 Monte Carlo Simulation

The first step of the simulation sequence is to start out with ideal placement of the transducers and probe. This default geometry of the probe and transducers is summarized in Table 3.1 and shown in Figure 3.1. The z-coordinates of transducer 2 and 3 were chosen to be non-zero. If all transducers were placed at $z = 0$ the matrix in equation 3.3 would be ill-conditioned, which would lead to large errors of the z-coordinate of the probe, makeing a reliable determination of the probes z-coordinate impossible.

TABLE 3.1: Choosen positions of the transducers and the probe.

	x [m]	y [m]	z [m]
Transducer 1	0	0	0
Transducer 2	100	0	2
Transducer 3	0	100	2
Transducer 4	100	100	0
Probe	50	50	-50

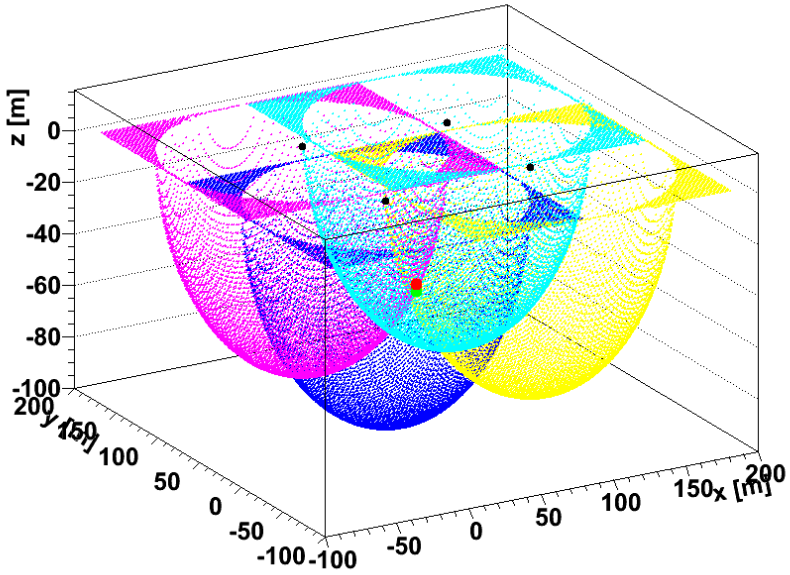

FIGURE 3.1: Geometry used in the Monte Carlo simulation. The transducers are shown as black dots and the spheres around each transducer indicate the allowed positions due to that transducer. The green point at the intersection of the spheres shows the real position of the probe and the red point above one example of the calculated position of the probe.

After the choosen geometry is fixed, the transducers are displaced by a Gaussian offset with the choosen coordinates as the mean and the assumed geometric uncertainties as the RMS. The initial uncertainty of the coordinates was assumed to be 5 cm. The same gaussian sampling is done to obtain the simulated "measured" velocity of the sound waves starting with an assumed choosen velocity of 3700 m/s and a default measurement error of 40 m/s. For the simulation of the synchronization between the transducers and receiver in the probe, the real signal propagation times between each transducer and the probe were calculated using the choosen transducer positions and the real speed of sound in ice, with an assumed default error of 1 µs.

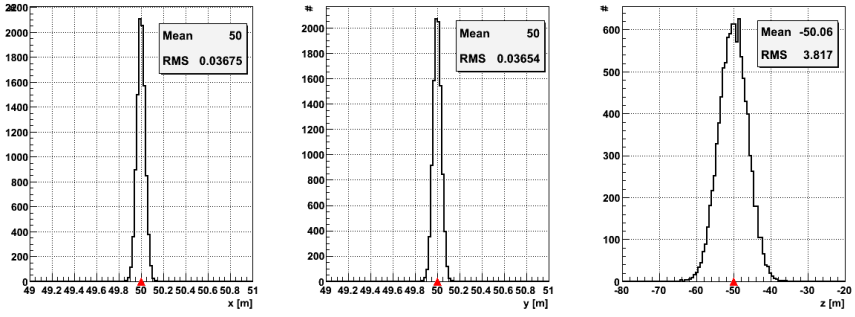

FIGURE 3.2: Distributions of the simulated coordinates of the probe. Every entry in the histograms corresponds to one estimation of the probes position. The red triangles indicate the real position of the probe and lie well in the center of each distribution.

The "measured" coordinates of the probe for each randomized Monte Carlo simulation are then calculated using the trilateration algorithm described in section 3.1.1. In order to gain a good estimate the uncertainty on the calculated position, 10000 Monte Carlo simulations are performed, resulting in the distributions shown in Figure 3.2. The total uncertainty of the calculated coordinates is then given by the RMS of these distributions.

3.1.3 Individual Uncertainties

In order to get limits on the individual error sources, the uncertainties on transducer position, timing and speed of sound were simulated separately. This means that in each plot all uncertainties but the one displayed on the x-axis were set to zero. The results of this procedure are shown in Figure 3.3, 3.4 and 3.5.

Transducer position

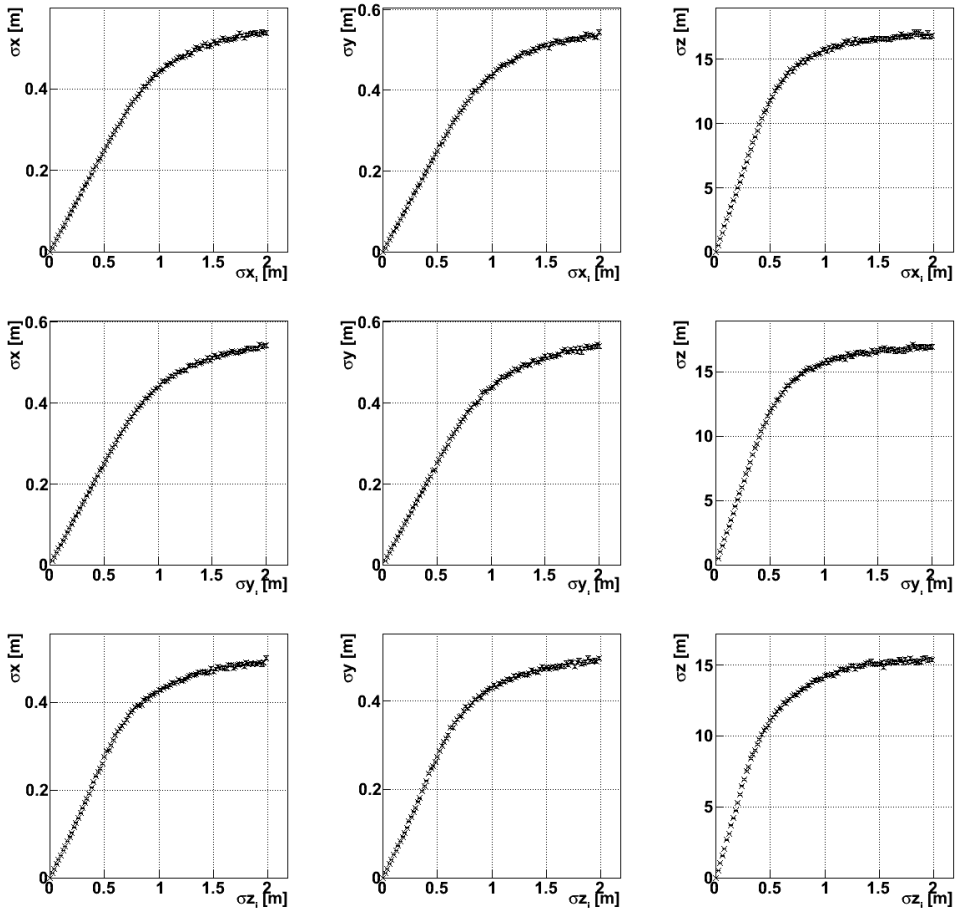

FIGURE 3.3: Accuracy of the probe's position depending on the uncertainties in the transducer positions. From left to right, the uncertainties on x-, y- and z-coordinate of the probe are displayed and from top to bottom the impact of the uncertainty on the x-, y- and z-coordinates of the transducers.

As expected the error of the probes position increases with growing uncertainties of all variables, the x- and y-coordinate of the probe behave alike and the largest error is always on the probes z-coordinate.

The typical error of the transducer position during the field tests was estimated to be between a few cm and 1 m. Therefore the simulated range of this uncertainty was choosen to range from 0 m to 2 m. As can be seen in Figure 3.3, all curves feature a steep rise with small transducer uncertainties which flatten out for larger values. The values for x- and y-coordinate are very similar and well below 1 m at all times. However, the value for the z-coordinate is much larger and crosses the required limit of 1 m at an uncertainty of ~ 5 cm.

Arrival time

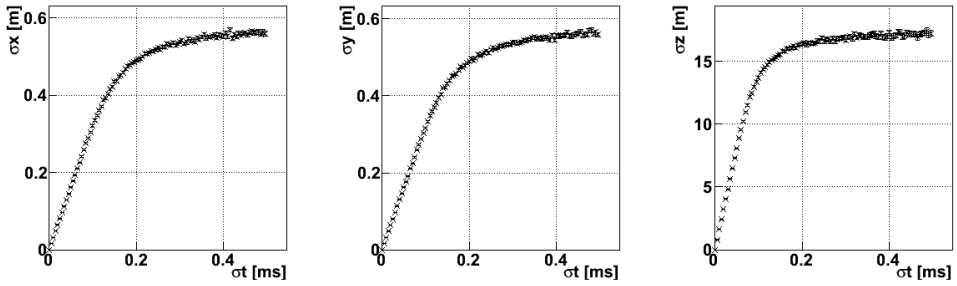

FIGURE 3.4: Accuracy of the probe's position depending on the uncertainties in the signal propagation time. From left to right, the uncertainties on x-, y- and z-coordinate of the probe are displayed.

Since the receivers and transducers can be synchronized with an accuracy of 1 µs, the main error source for the timing is the uncertainty in the signal propagation time. To investigate this, signal propagation time uncertainties up to 500 µs were simulated. The shapes of all curves in Figure 3.4 are similar to those of the transducer position plots. Again, the errors on x- and y-coordinate are below the required accuracy in the simulated range, while the z-error crosses the 1 m threshold at only 5 µs.

Speed of sound

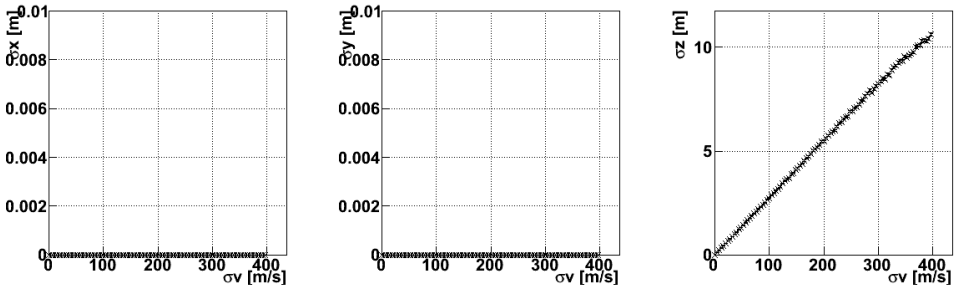

FIGURE 3.5: Accuracy of the probe's position depending on the uncertainties in the speed of sound in ice. From left to right, the uncertainties on x-, y- and z-coordinate of the probe are displayed.

For the speed of sound, uncertainties of up to 400 m/s were considered, corresponding to the variations observed during the field tests. As can be seen in Figure 3.5, at the default probe position in the center of the array there is no error on the x- and y-cooirdnate. This is expected because every change in the speed of sound leads to the same change

in the distance between each transducer and the probe. Hence in these directions these varieties cancel each other out. For the z-coordinate this is not the case and one can observe a linear dependence between the uncertainty on the speed of sound and the error on this coordinate. The limit of 1 m is reached at an uncertainty of 35 m/s, which is less than 1 % of the assumed speed of sound.

3.1.4 Combined uncertainties

After considering all uncertainties separately, the next step is to study the influence of the probe's position relative to the array. For this simulation the default settings are used. The position of the probe is fixed in one direction while the other two are varied from 10 m to 110 m in x and y and -110 m to 10 m in z-direction. Overall, four simulations have been performed with different coordinates of the probe, as summarized in table 3.2. The results for the center-settings are shown in Figure 3.2, while the results for the other settings can be found in Appendix A.

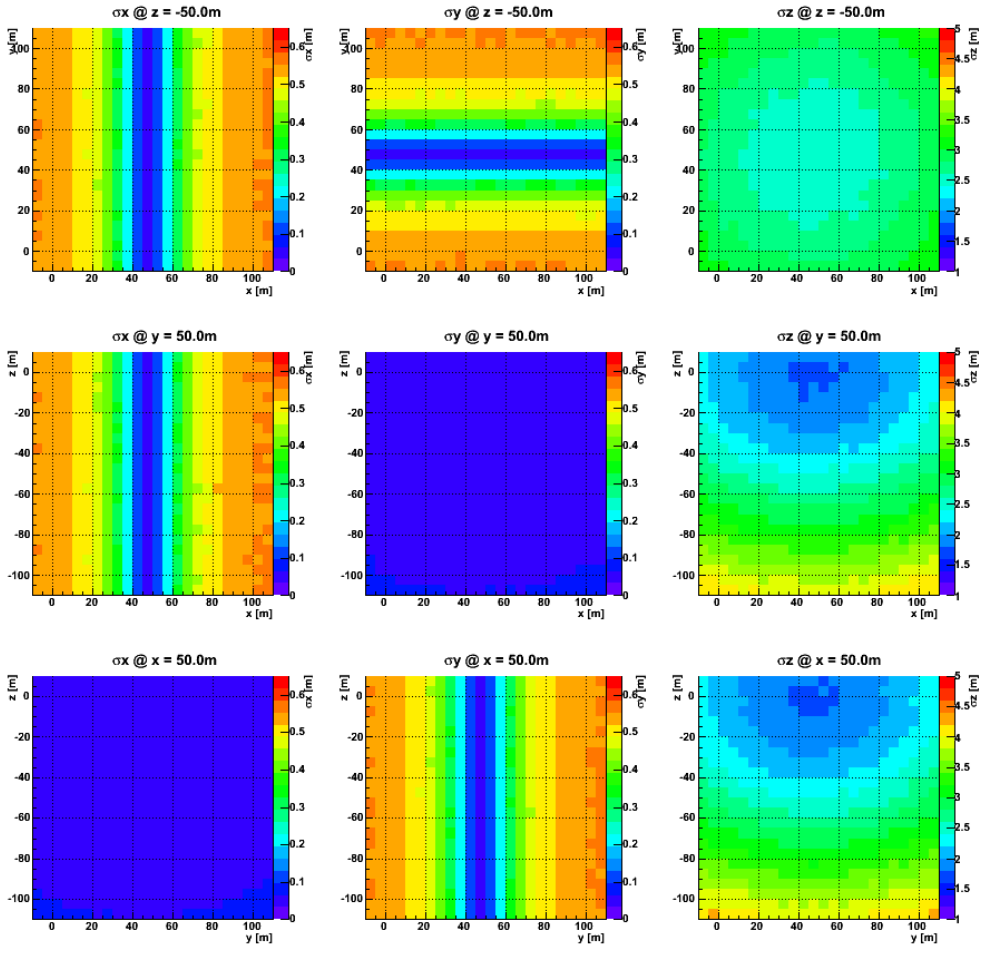

FIGURE 3.6: Accuracy of the probe's position depending on the position of the probe below the transducer array. The values of the uncertainties of transducer position, speed of sound and signal propagation time were the default values described in section 3.1.2. Each row shows the uncertainties of the probes coordinates in one plane. In the top row the $z$coordinate was fixed at -50 m and in the rows below y- and x-coordinate were fixed in the center of the array at 50 m.

As can be seen in the first and second column of Figure 3.6, the uncertainties on x- and y-coordinate depend only on the probe's position in that direction and increase when the probe is moved away from the center of the array. For the z-coordinate, there is a dependency on all three directions. Overall, the most precise determination can be reached when the probe is in the center of the array and at the surface. Every movement away from the center or deeper into the ice leads to an increased uncertainty. Overall, the uncertainties on x and y remain well below 1 m while for z, 1 m is ambitious.

TABLE 3.2: Fixed coordinates for the simulation on the influence of the probes position.

	x [m]	y [m]	z [m]
Center	50	50	-50
Half Center	25	25	-25
Edge	0	0	0
Outside	-10	-10	10

3.1.5 Influence of the transducer geometry

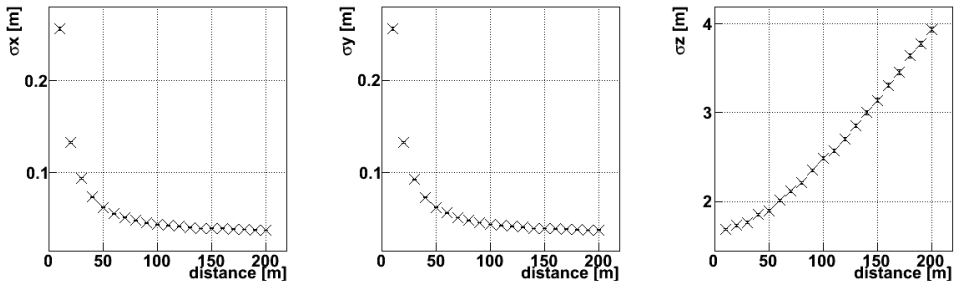

FIGURE 3.7: Accuracy of the probe's position depending on the spacing between the transducers within the array. From left to right the uncertainties on x-, y- and z-coordinate of the probe are displayed.

The last part of the simulation study is on the geometry of the transducer array. The two variables considered are the space between the transducers and their depth range. For both simulations the default settings were used and only the distances between all transducers or respectively the depth of transducer 2 and 3 were varied by multiplying the default geometry by a scale-factor. The results showing the dependency on the spacing are shown in Figure 3.7 while the dependency on the depth is shown in Figure 3.8. Spacing distances between 10 and 200 m and depths ranging from 0.1 m to 4.0 m have been considered.

In both simulations, the accuracy in x- and y-direction increases with larger distances and depths up to a certain point and then remains constant. For the distance dependency this point is reached at roughly 100 m and for the depth dependency already at $\sim$ 30 cm. As expected in case of the dependency on the distance the accuracy in z-direction behaves the other way around. For larger distances the impact of the constant depth difference reduces leading to larger uncertainties on the z-coordinate. The error in the z-direction only remains under 1 m if the spacing is less than 20 m. The impact of the depth range

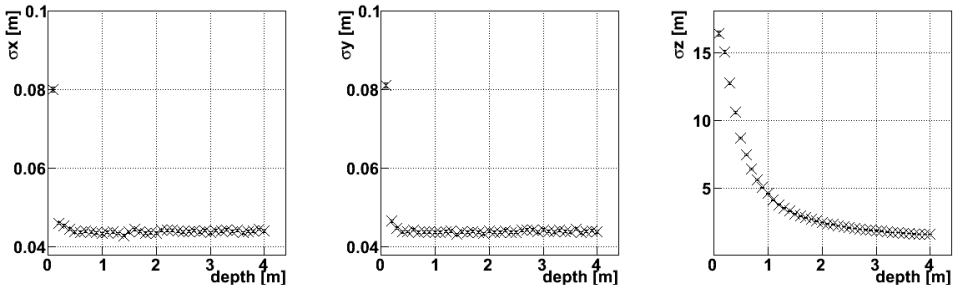

FIGURE 3.8: Accuracy of the probe's position depending on the depth difference of the transducers. From left to right the uncertainties on x-, y- and z-coordinate of the probe are displayed.

on the z-coordinate can also be seen in the last plot of Figure 3.8 where a steep reduction is seen before the curve flattens.

Chapter 4

Acoustic signals

Acoustic signals are mechanical waves propagating through an elastic medium. The acoustic field can be described by the field quantities pressure $\tilde{p}$, density $\tilde{\rho}$ and particle velocity $\tilde{\vec{v}}$. These variables depend on on location $\vec{r}$ and time t and can be expressed as

$$\begin{aligned}\tilde{p}(\vec{r},t) &= p_0 + p(\vec{r},t)\\ \tilde{\rho}(\vec{r},t) &= \rho_0 + \rho(\vec{r},t)\\ \tilde{\vec{v}}(\vec{r},t) &= \vec{v}_0 + \vec{v}(\vec{r},t)\end{aligned}$$

Where p_0, ρ_0 and $\vec{v}_0$ are the static values of the medium and $p(\vec{r},t)$, $\rho(\vec{r},t)$ and $\vec{v}(\vec{r},t)$ describe the perturbations of these quantities.
Because of the large range of these variables, it is convenient to use a dimensionless level L_p, given in dB, to categorize sound sources. In this case the level is given by

$$L_{\tilde{p}} = 20 \cdot \lg\left(\frac{\tilde{p}}{\tilde{p_0}}\right) \tag{4.1}$$

The reference pressure $\tilde{p_0}$ depends on the medium. For air, the standard reference is the auditory threshold of an average human, 20 µPa. In water the reference pressure is 1 µPa. [38]

4.1 Propagation

In the case of an ideal compressible liquid, the propagation of acoustic waves can be described using the Euler equations:

$$\vec{F} = \tilde{\rho}\frac{d\tilde{\vec{v}}}{dt} + \nabla\tilde{p} \qquad \text{(conservation of momentum)} \tag{4.2}$$

$$0 = \frac{\partial\tilde{\rho}}{\partial t} + \nabla(\tilde{\rho}\tilde{\vec{v}}) \qquad \text{(conservation of mass)} \tag{4.3}$$

The speed of sound of the wave, c_s, is given by the pressure-density relation:

$$p = c_s^2 \cdot \rho. \tag{4.4}$$

The acceleration component in equation 4.2 can be rewritten as:

$$\frac{d\tilde{\vec{v}}}{dt} = \frac{\partial\tilde{\vec{v}}}{\partial t} + \left(\tilde{\vec{v}}\cdot\nabla\right)\tilde{\vec{v}}, \tag{4.5}$$

where the first term represents for the local acceleration while the second one represents the convective acceleration.
The perturbations of pressure and density of a sound wave are usually small, so that $\tilde{p} \approx p_0$ and $\tilde{\rho} \approx \rho_0$. For example in case of pressure, the static pressure is $\sim 10^5$ Pa while the perturbations caused by a jackhammer are only about 50 Pa. For small values of $\vec{v}_0$ compared to the local acceleration, the convective acceleration can be neglected and equations 4.2 and 4.3 can be simplified to:

$$\vec{F} = \tilde{\rho}\frac{\partial \vec{v}}{\partial t} + \nabla \tilde{p} \tag{4.6}$$

$$0 = \frac{\partial \rho}{\partial t} + \rho_0 \nabla \cdot \vec{v}. \tag{4.7}$$

In addition these perturbartions are taken to occur quickly, and therefore it can be assumed that no heat is exchanged with the surrounding medium. This means, that the adiabatic relations for gases and liquids can be applied.

$$p = \kappa \frac{p_0}{\rho_0}\rho \qquad \text{(gases)} \tag{4.8}$$

$$p = \frac{1}{\chi p_0}\rho \qquad \text{(liquids)} \tag{4.9}$$

For gases, κ is the adiabatic index and for liquids χ gives the adiabatic compressibility. The speed of the sound wave is then given as $\sqrt{\kappa p_0/\rho_0}$ for gases and $\sqrt{1/(\chi p_0)}$ for liquids.
Assuming there are no external forces and using that the velocity field $\vec{v}$ is irrotational, the above system of equations can be transformed into a set of scalar equations for p and $\vec{v}$:

$$\frac{1}{c^2}\frac{\partial p}{\partial t} - \Delta p = 0 \tag{4.10}$$

$$\frac{1}{c^2}\frac{\partial \rho}{\partial t} - \Delta \rho = 0 \tag{4.11}$$

$$\frac{1}{c^2}\frac{\partial \vec{v}}{\partial t} - \Delta \vec{v} = 0 \tag{4.12}$$

For the velocity, a potential ϕ must exist that fulfills $\vec{v} = -\nabla\phi$. Since p and ρ are also defined by this potential as $p = \rho_0 \partial\phi/\partial t$ and $\rho = \rho_0/c^2 \partial\phi/\partial t$, a sound field is fully described when this potential is known.
For a spherical wave, the potential is given as:

$$\phi(\vec{r}, t) = \frac{\phi_0}{r} \cdot e^{i(\omega t - kr + \varphi_0)},$$

where r is absolute value of the distance, ω the oscillation frequency, k the wavenumber and φ a phase constant. For the sound pressure p a similar equation can be derived:

$$p(\vec{r}, t) = \frac{p_0}{r} \cdot e^{i(\omega t - kr)} \qquad \text{with } p_0 = i\phi_0\omega\rho_0 e^{\varphi_0} \tag{4.13}$$

One should keep in mind, that this description is only accurate for gases and liquids, where acoustic waves are longitudinal waves. [38]

4.1.1 Attenuation

Up to now, only propagation through a lossfree medium has been described. To take attenuation into account, an additional factor α has to be included in equation 4.13:

$$\begin{aligned} p(\vec{r},t) &= \frac{p_0}{r} \cdot e^{i(\omega t - kr)} \cdot e^{\alpha r} \\ &= \frac{p_0}{r} \cdot e^{i(\omega t - \gamma r)} \qquad \text{with } \gamma = -i\alpha + k \end{aligned} \tag{4.14}$$

where γ is the so called complex propagation constant. Generally acoustic attenuation is caused by inner friction, thermal dissipation and molecular absorption.
Inner friction depends mainly on the dynamic viscosity η of the medium. As can be seen from its attenuation coefficient given in equation 4.15, its magnitude is proportional to ω^2. This means the attenuation is proportional to the square of a sound waves frequency f, leading to stronger attenuation for higher frequencies.

$$\alpha_{friction} = \frac{2}{3}\frac{\eta}{\rho_0}\frac{\omega^2}{c^3} \tag{4.15}$$

Thermal dispersion describes the adiabatic changes of state, which are caused by the acoustic wave passing through the medium. As the wave passes through the media small oscillations in temperature are induced. As this thermal gradient diffuses into the media the wave's energy which caused the change in temperature is permanently lost leadig to this thermal dispersion attenuation. The attenuation coefficient for this (given in 4.16) is again proportional to the square of the frequency and also leads to larger losses for higher frequencies.

$$\alpha_{dispersion} = \frac{\kappa - 1}{\kappa}\frac{\omega^2 \nu}{2 C_V \rho_0 c^3}, \tag{4.16}$$

where ν is the thermal conductivity and C_V is the specific heat capacity at a constant volume.
Molecular absorption happens, when the rotational or vibrational degrees of freedom of the media are excited by the acoustic wave. While the energy exchange with the rotational degrees of freedom happens quickly, the transfer to the vibrational degrees of freedom is quiet slow. It therefore takes time for the media to reach thermical equlibrium between translational, rotational and vibrational energy. This time is called relaxation time τ and the attenuation due to this also is dependent on the waves frequency and is given by

$$\alpha_{absorption}\lambda = \pi\epsilon\frac{\omega\tau}{1+\omega^2\tau^2}, \tag{4.17}$$

where ϵ is the fraction of energy exchanged in the relaxation process.

4.1.2 Acoustic waves in solids

In addition to a resistence against volumetric changes, the mechanical properties of solids also cause counterforces against changes of their shape. These forces are called

shear forces and have a strong influence on the propagation of acoustic waves through a solid body.
This mechanical property can be described by two symmetrical second rank tensors σ_{ij}, that represents stress forces and ϵ_{ij} representing mechanical distortions. The relation between these two tensors is given by Hooke's law:

$$\sigma_{ij} = c_{ijkl} \cdot \epsilon_{kl} \tag{4.18}$$
$$\epsilon_{kl} = s_{klij} \cdot \sigma_{ij} \tag{4.19}$$

Where the coefficients c_{ijkl} and s_{klij} are the modulus of elasticity, also called Young's modulus.
When these forces are included, the wave equation is changed to

$$(2\mu + \lambda)\Delta\vec{d} + (\mu + \lambda)\nabla \times (\nabla \times \vec{d}) = \rho_0 \frac{\partial^2 \vec{d}}{\partial t^2}, \tag{4.20}$$

where $\vec{d}$ is the distortion of the body and λ and μ are the so called Lamé constants. λ is a measure for the, to the force, vertical expansion while μ is the shear modulus.
According to the superposition principal $\vec{d}$ can be decomposed into a irrotational part $\vec{d}_L$ and a solenoidal part $\vec{d}_T$:

$$\vec{d} = \vec{d}_L + \vec{d}_T \tag{4.21}$$

Both parts describe two different types of waves. As the indices T and L imply, those types are longitudinal waves in case of the irrotational part and transversal waves for the solenoidal part. When considering both parts separately also one can derive their respective speed of sounds from equation 4.20. For longitudinal waves the speed of sound is determinded to be

$$c_L = \sqrt{\frac{2\mu + \lambda}{\rho_0}}. \tag{4.22}$$

For transversal waves, also called shear waves, the speed of sound is

$$c_T = \sqrt{\frac{\mu}{\rho_0}}. \tag{4.23}$$

According to [38] the ratio c_L/c_T of both speeds of sound is approximately 1.9. Meaning, that the shear waves are expected to take twice as long as the longitudinal waves to arrive.

4.2 Generation and Detection

For the generation and detection of acoustic signals electro-acoustic converters are used. As the name suggests these converters convert acoustical energy into electrical energy or the other way around. Acoustic receivers convert acoustic energy to electricity, while acoustic emitters convert electric potentials to acoustic energy.
There are several different types of electro-acoustic converters, for example electrostatic converters, electrodynamic converters, electromagnetic converters, magnetostrictive converters and piezoelectric converters. All converters used in this work are piezoelectric converters, which are based on the piezoelectric effect.

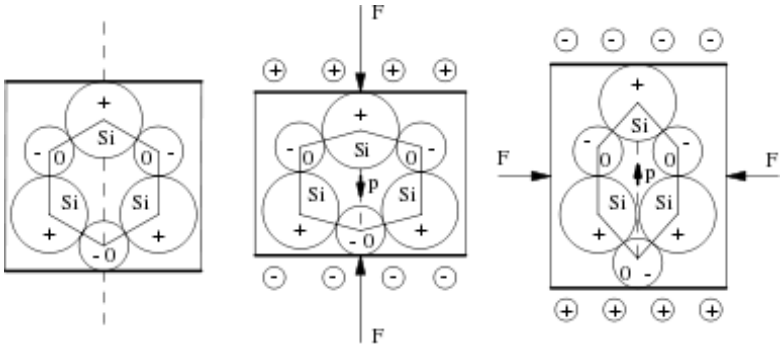

FIGURE 4.1: Priciple of the piezoelectric effect for a SiO_2-crystal [38].

When a piezoelectric material is deformed mechanically, for example by the external pressure of a sound wave, at its surface a detectable electrical polarisation occurs. This effect is called the piezoelectric effect and is mostly observed in crystalline materials. In Figure 4.1 the effect is shown for a SiO_2-crystal. On the left the molecular structure is shown without any applied strain, while in the middle and the right plot strains from different directions are applied. One can see how the center of charge of positive and negative charges get shifted, so that they do not match any more, resulting in the afore mentioned electrical polarisation at the surface. By recording this polarisation, this effect can be utilized to detect the pressure changes caused by acoustic waves.
This effect can also be inverted by applying an electrical current to the material that results in a mechanical deformation of the material. This is called the reziprocal piezo effect and can be used for the generation of acoustic signals. [38]

Chapter 5

Field tests

Throughout the project several field tests have been performed. The goal of these tests was to achieve a better understanding of the propertiies of glacial ice to match the requirements described below and also to improve the system design according to the results. In addition test campaigns on glaciers offer the possibility to test the equippment in an environment as close as possible to the scenario on Enceladus.

5.1 Challenges and requirements of the APS

The main goal for the positioning was to reach a precision below 1 m on the absolute position of the probe over a distance of 100 m.
A Monte Carlo simulation was used to estimate how uncertainties on signal propagation time, speed of sound and position of the transducers influence the positioning of the probe. Details can be found in section 3.1. According to that simulation a dense spacing of the transducers with distances around 20 m is necessary and especially for the determination of the z-coordinate the depth range of the transducers should be as large as possible, but at least 2 m. Also the array should cover the whole drilling area, so that the probe remains within the array at all times. In order to match the 1 m precision for all coordinates it is necessary to know the position of the transducers with an error below 5 cm and the signal propagation time with an precision of 5 µs. The most challenging task is the determination of the speed of sound. According to the simulation already at an uncertainty of 35 m/s the limit of 1 m is crossed. However the simulation does not cover directional dependencies of the speed of sound in the ice, which could lead to an even larger impact of this error source.
On the technical side the signal propagation time measurement requires an accurate time synchronization between the transmitting system on the surface and the receiving system within the probe at an even higher level of 1 µs and a dependably functioning algorithm to determine the arrival time of an acoustic pulse. The determination of the transducer positions requires the usage of a precise positioning system on the surface. During most field tests this system was a differential GPS device with a precision in the sub millimeter range. The determination of the speed of sound is the most interesting challenge for the positioning. There can be large differences between different glaciers and also directional and depth dependent variations on one test-site are very likely. For the purpose of including the directional variations in the positioning algorithm the transmitting system can be used for measurements between the transducers. The depth dependent variations need to be monitored while the probe melts itself deeper into the ice.
The range of the system is physically limited by the attenuation length in ice. In practical life it can be influenced by the used frequency, the coupling between the transducers and the ice, the maximum emitting power, and the choice of the positions of the transducers.

Since the influence of cracks and secluded crevasses is unclear, fissured regions should be avoided and of course a good coupling between transducer and ice has to be established to make sure the energy of the signal is not lost. However the main restriction is the frequency dependent attenuation in ice. In order to reach the maximum range the optimal frequencies of the transducers on the surface and the receivers in the probes head should match. In addition one has to compromise between the resolution of the system, that favors higher frequencies, and the range, which is higher for lower frequencies.

5.2 Test campaigns on glaciers

A list of all field tests performed during the first phase of the project can be found in table 5.1. The temperate glaciers were chosen due to their accessibility and the infrastructure at their location, allowing more extensive measurements with the given resources. The test sites on cold glaciers on the other hand were chosen, because they are expected to be more similar to the conditions expected on Enceladus.

TABLE 5.1: List of the field tests performed during the project.

Field test	Glacier	Year	Temperature
0.0	Morteratsch glacier	2012	temperate
1.0	Morteratsch glacier	2013	temperate
2.0	Canada glacier	2013	cold
2.5	Pers glacier	2014	temperate
3.0	Taylor glacier	2014	cold

When choosing a test site it is important to differentiate between temperate and cold glaciers. The ice on a temperate glacier has a temperature of exactly 0 °C leading to the occurrence of a liquid water on the surface that fills all cracks and holes, while the ice temperature on a cold glacier is well below 0 °C, which is why cracks and holes can be filled with air instead of water leading to different ice properties and a potentially smaller attenuation length.

5.2.1 Temperate glaciers

Throughout the project most field tests have been performed on temperate glaciers. The test sites on these glaciers are located close to each other in the Swiss Alps and are very easy accessible due to the infrastructure that comes with tourism in that region. That means there is accommodation in walking distance to the test sites and helicopter flights are available for the transport of the needed hardware to the test site. Figure 5.1 shows the locations of the test sites in that region.
The first field test was performed on the Morteratsch glacier in June 2012. The main purpose of this field test was to to test hardware under real life settings and the test of different transmitters. In addition the influence of a crack in the ice was investigated, first data on the depth dependency of the speed of sound was taken and a first estimation of the operational range of the system was gained.
The site for the acoustic tests covered an area of $\sim 30 \times 10\ \mathrm{m}^2$ at a height of ~ 2400 m above sea level. For the determination of the hole positions during this first field test only measuring tape with a total length of 5 m was available, which is why a measurement of

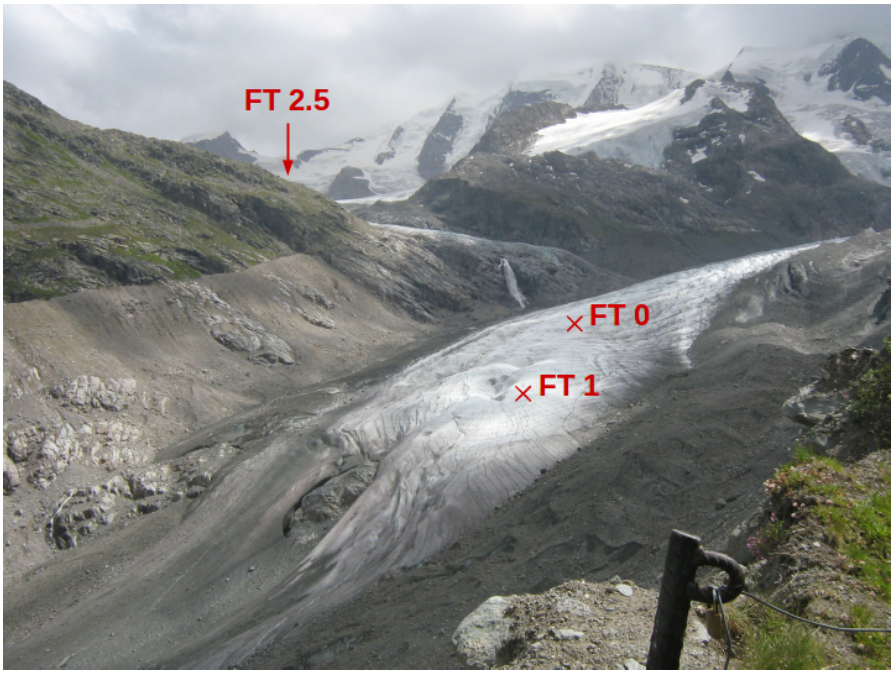

FIGURE 5.1: Locations of all test sites on temperate glaciers in the Swiss Alps.

the absolute 3 dimensional positions of the holes was impossible and only the distances on the surface between neighboring holes were measured. Figure 5.2 shows a sketch of the test site including these measurements and four cracks that were found in the ice of the test site, all perpendicular to the flow direction of the glacier.

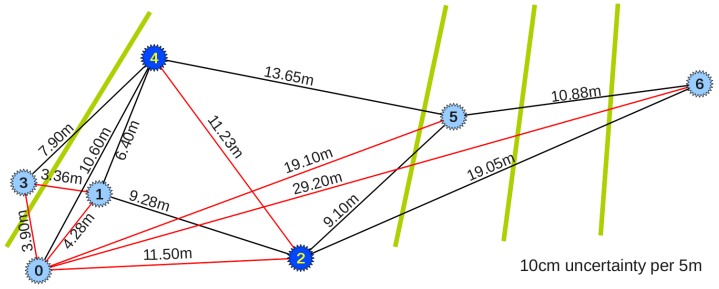

FIGURE 5.2: Map of the test site on the Morteratsch glacier in 2012. The blue circles indicate where holes were drilled, light blue means the hole had a depth of 2 m and dark blue indicates a depth of 5 m. The broad green lines mark the positions of those cracks through the test site that were visible at the surface. Along all thin lines the distances between the holes where measured and the red color of some indicates paths along which also acoustic signals where transmitted.

For the signal generation during field test 0.0 the electronics of the south pole acoustic test setup (SPATS) was used. This box generates signals with frequencies of 30 kHz, 45 kHz and 60 kHz that have a length of 32 periods and are repeated 64 times. Besides the mainly used ITC-1001, also a SQ09 and a Hades sensor were used as acoustic emitters. Details on these will be given in Chapter 6.1. For receiving the signals 4 sensors were mounted on a rail at a distance of 0.5 m from each other. After passing through a

preamplifier (1:200), the signals recorded by these sensors were read out by a digital scope.
The second field test on a temperate glacier took place in May 2013 also on the Morteratsch glacier but closer to the glaciers tongue. It was the first field test with the newly developed and build transducer system consisting of a CTU and 6 FTUs and of course the transducers themselves, that is described in Chapter 2. Besides testing the functionality of the new hardware under real life settings, the aim of this field test was to collect further data on the ice properties. Therefor extensive measurements of signals in different directions and at different depth up to 11 m have been performed in order to gain information on the behavior of the speed of sound. These measurements covered distances up to 72 m expanding the range of the transducer system and allowing a first determination of the attenuation length at a frequency of 17 kHz. In addition a method for the insertion of the transducers in temperate glaciers using water filled holes with an optimal coupling to the ice was developed.

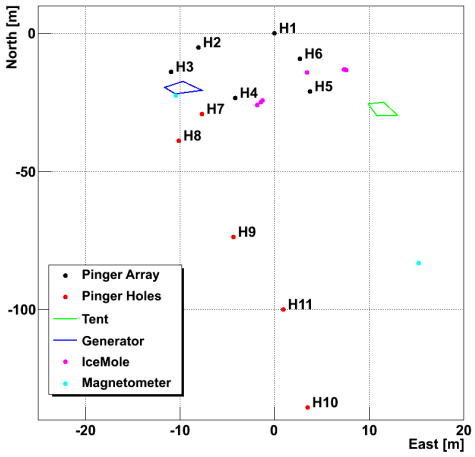

FIGURE 5.3: Map of the test site on the Morteratsch glacier in 2013 including the positions of the operator tent, the generator tent, the magnetometer and the melting positions of the IceMole. The holes 1 to 6 were used for the positioning of the IceMole and had a depth of ~ 0.5 m. The holes 7 to 11 were drilled for ice property measurements and had a depth of up to 12 m.

The test site was located at a height of ~ 2200 m above sea level and covered an area of $\sim 30 \times 120$ m^2. Located next to the test site was a huge crevasse. Here the determination of the hole positions was done using the differential GPS-system provided by the Universität der Bundeswehr München that delivers 3D-coordinates with an excellent accuracy.
The last field test on a temperate glacier was on the Pers glacier in June 2014. The main purpose of this field test was to acquire more data on attenuation in cold ice and to perform more measurements for studying directional dependencies of the speed of sound. In addition the range of the transducer system was extended to the, on Enceladus, required 100 m.
The Pers glacier originates at Piz Palü and joins the Morteratsch glacier below the rock formation Isla Persa, which is a few 100 m above the test site of field test 0.0. This test site was chosen because, due to its higher location, it was still covered with 1 m to 2 m

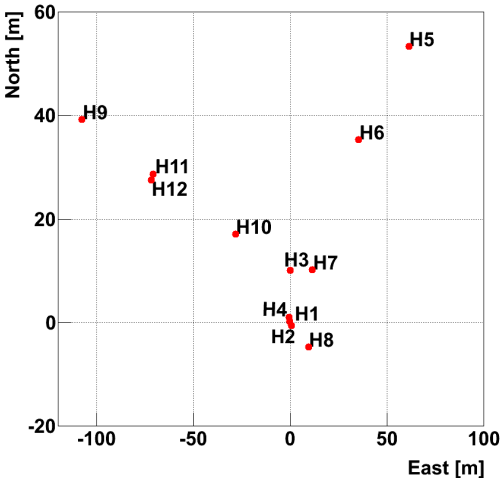

FIGURE 5.4: Map of the test site on the Pers glacier in 2014. Each red point marks one hole for transmitter insertion, numerated from 1 to 12.

of snow during the field test, which could mean that the ice was still colder than 0 °C. It covered an area of $\sim 150 \times 60$ m^2 at an height of ~ 2700 m above sea level.
In parallel to this test another field test was done on the lower situated Morteratsch glacier which included a complete transducer system. Therefor for the tests on the Pers glacier only two transducers were available and a separate preamplifier was used on the receiver side instead of a FTU. Also the determination of the hole positions had to be aquired with a measuring tape and a compass, which lead to non-neglectable uncertainties on the absolute 3D-coordinates of the holes.

5.2.2 Cold glaciers

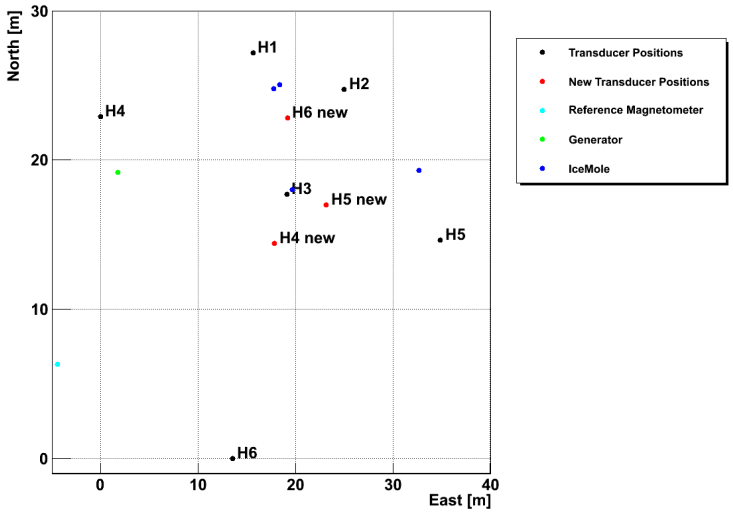

FIGURE 5.5: Map of the test site on the Canada glacier in 2013.

Both cold ice tests took place in the McMurdo Dry Valleys in Antarctica where the ice temperature is at -17°°C [4] and were executed by an Antarctica-operation team. For

the measurement of the hole positions during both cold ice tests the aforementioned differential GPS device was used. For the acoustic measurements during these tests the complete APS as described in Chapter 2 was used.
The first field test on a non-temperate glacier took place on the Canada glacier in Antarctica in 2013. Since this was the first cold ice test the first step was to test the coupling to the ice of frozen in transducers in realistic glacial ice. Once the coupling was sufficient as much data was to be collected in as many different directions and distances as possible in order to gain information on the ice properties such as directional dependencies of the speed of sound, the attenuation length and the range of the system that is limited by the later.
The test site covered an area of $25 \times 35\ \mathrm{m}^2$ and was located ~ 80 m above sea level. A map of the test site can be found in Figure 5.5. As can be seen on the map, half of the transducers were repositioned closer to the trajectory of the probe during the field test.

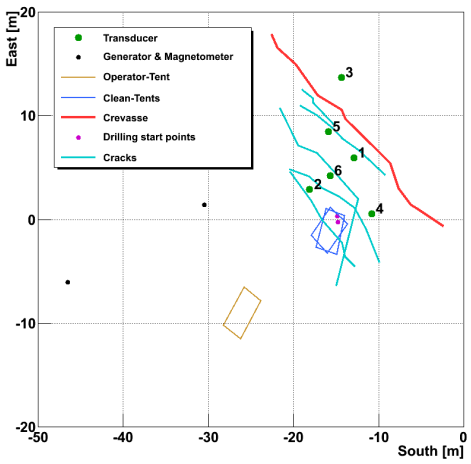

FIGURE 5.6: Map of the test site at the Blood Falls in 2014.

The final field test took place at the Blood Falls in 2014, a place first discovered in 1911 by Griffith Taylor [39]. This test site is especially interesting, since it provides a very similar scenario to the one expected on Enceladus.
As can be seen in Figure 5.7 the name "Blood Falls" originates from the red color of the brine leaking through tiny fractures at the tongue of the Taylor glacier, where the brine flows onto the frozen surface of West Lake Bonney. Unlike G. Taylor first thought the red color is not caused by algae but occurs due to a high concentration of ferric hydroxide in the brine that turns red due to oxidation when in contact with air [40]. The origin of the brine is a subsurface hyper saline lake which lies under ~ 400 m of ice 5 km up the Taylor glacier [41]. That lake was isolated from the Antarctic ocean by a glacier 1.5 million years ago allowing a unique ecosystem to develop that is still undisturbed until today [42]. The geochemical analysis of samples taken from the Blood Falls outflow has shown signs of the existence of autotrophic bacteria who metabolize with iron and sulfur compounds, making the test site especially interesting for microbiologists [43, 44].
The goal of this field test was to take a sample of the brine directly from the crevasse and hand to the US scientists of the MIDGE project. Since the bacteria in the brine are destroyed when in contact with air it is essential to take that sample before it had any contact with air and of course without contaminating the ecosystem. This means the melting probe needs to melt its way to the crevasse, identify the crevasse in time,

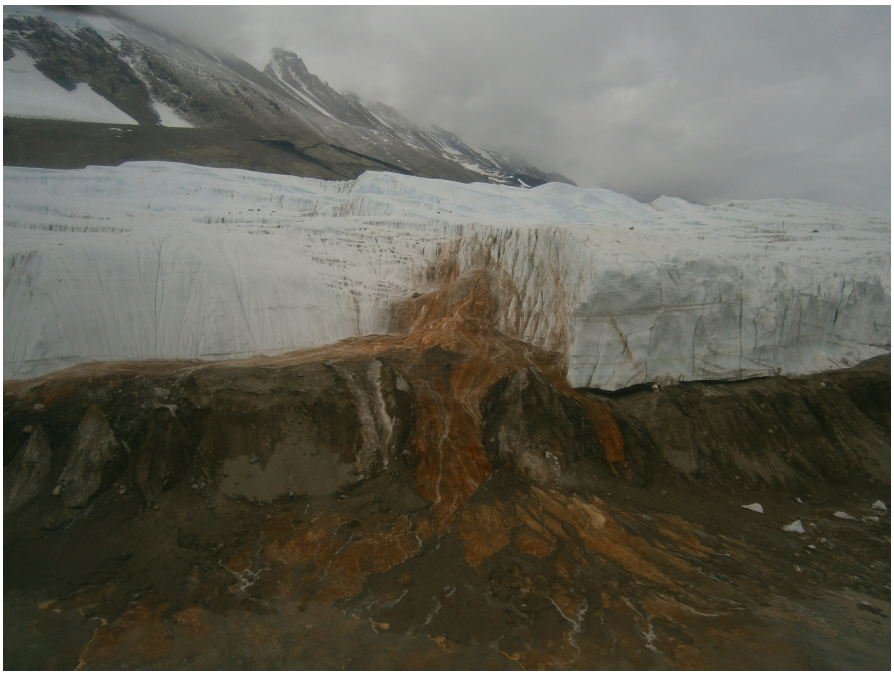

FIGURE 5.7: Photo of the Blood Falls taken from the Helicopter during the test campaign in 2014 [6].

take a sample and return itself and the sample to the surface, making this the perfect test site to show that all systems are functional and able to perform their tasks. For the acoustic positioning system in addition, this was another chance to accumulate more cold ice data [45, 46].

Chapter 6

System tests of the APS

A solid understanding of the systems characteristics is essential to optimize the usage of the transmitter system in the field. In order to achieve this understanding several measurements have been performed, which are described in this chapter. The key points are the comparison of different acoustic transmitters, the understanding of the systems frequency behavior, and last but not least the influence of the coupling between the transmitters and the ice.

6.1 Transducer comparison

The requirement for the transmitter is to be detected by the probe within all of the operating volume. That means it should be omni-directional and have an amplitude as high as possible to cover a volume as large as possible. During the first field test on the Morteratsch glacier in 2012 three transmitters were tested. The first one was a HADES-sensor (Hydrophone for Acoustic Neutrino Destection at South Pole), the second one the comercial hydrophone SQ09 from the Canadien company SENSOR, and the third was the ITC-1001 from the International Transducer Company. As a test medium the ice of the Morteratsch glacier was used.

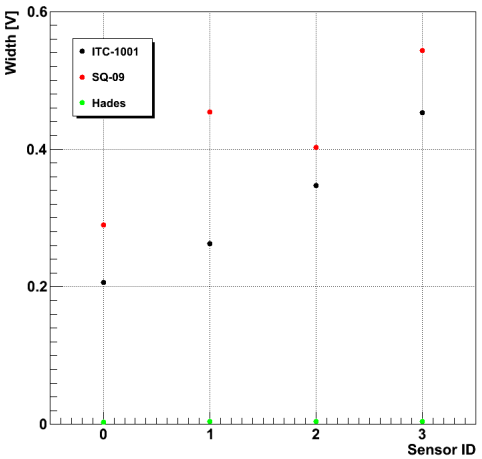

FIGURE 6.1: Comparison of the different emitters investigated during field test 0.0. The data was recorded between holes 3 and 0. The width of the signal against the ID of the 4 sensors used simultaneously in this field test is plotted.

The HADES-sensor was designed for deployment in Antarctica. Therefore, it is designed to handle pressures of up to 100 bar, low temperatures down to −50 °C, and its cylindrical piezo element ensures a good angular coverage. A detailed description can be found in [47].
The SQ09 was chosen because of its broad frequency range and its robustness against temperature and pressure changes. According to its manufacturer it covers a frequency range of 3 Hz down to 20 kHz and is operable at temperatures between −30 °C and +60 °C and up to a depth in water of 2500 m [48].
The frequency range of the ITC-1001 is 2 to 38 kHz and is sufficient for the intended purpose and the operability up to depths in water of 1250 m. In addition it has an omnidirectional response, making it ideal for equally covering the entire site with the sound waves [7].
Figure 6.1 shows the comparison of the emitters tested during field test 0.0. During this field test four sensors were used at the same time. The plot shows the width of the signals, calculated as described in Chapter 7.4.1, on the y-axis plotted against the sensor ID on the x-axis. The HADES-sensor is not well suited for emitting signals and produces much lower outgoing signals than the other two. Although the two hydrophones were operated outside of their ideal frequency range they still produce high signal amplitudes. The values for the SQ09 are even higher than for the ITC-1001. Since both are on the same order of magnitude and the ITC-1001 is an omnidirectional emitter the final decision was to use the ITC-1001 as a transducer for the EnEx project.

6.2 Directional and frequency dependencies of the IceMole-Head

During the field tests between the transducers at the surface, signals were recorded at distances over 100 m. At the same time the recievers in the probe were only able to record signals from transducers that were much closer. One explanation for this could be an insufficient frequency matching between the receivers in the IceMole-Head and the emitters at the surface or directional dependencies of these same receivers.
In order to determine if there are any directional frequency dependencies of the IceMole-Head, frequent changes of the geometry of the system during the measuring campaign are required. This is not possible when all components are frozen in ice. Since the acoustic attenuation in air has proven to be too large, this difficulty was avoided by performing the frequency measurements in water instead.
In all acoustic lab measurements it is important to be able to distinguish between the direct signal and reflections, hence the water volume should be as large as possible.

6.2.1 Setup

The test facility used was the Wuppertal Water Tank, a cylindrical water volume of $\sim 10\,\mathrm{m}^3$ with a height of 2.35 m and a diameter of 2.5 m. The basic geometry of the water tank is shown in Figure 6.2. On top of the tank a walkable wooden platform is installed with a $\sim 1\,\mathrm{m}^2$ opening in the center for insertion of hardware into the water. A more detailed description can be found in [47].
For the measurements within the watertank two different receivers were used, which required slightly different electronics for the readout. Figures 6.3 and 6.4 show a sketch of the electronics for both cases. In all measurements an ITC-1001 was used for sending the signals. In one case a second ITC-1001 was used for receiving and in the other case

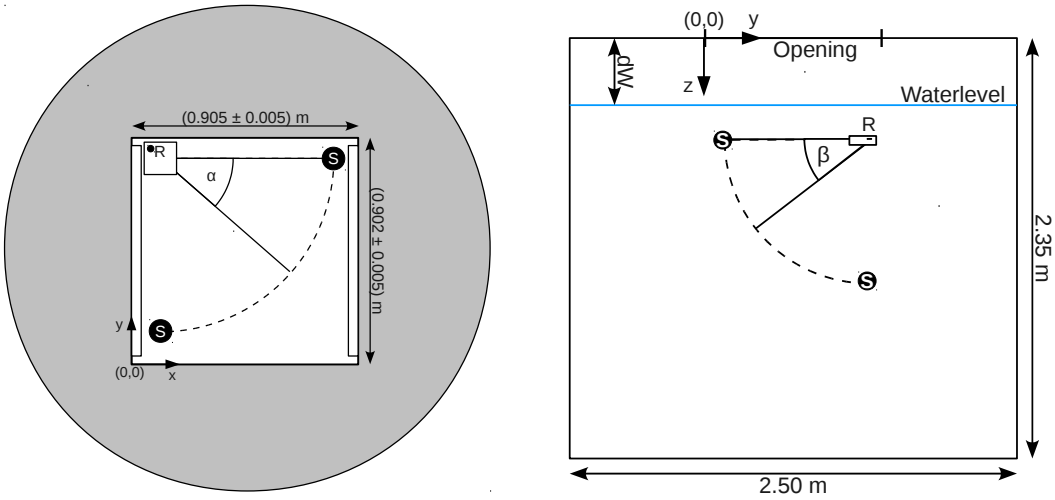

FIGURE 6.2: Setup of the frequency measurements inside the water tank. On the left the geometry for a horizontal scan from above is shown, including the IceMole-head with the receiver R and the ITC-1001 used as the sender S as well as the opening through which all components were inserted in the tank. On the right the geometry for a vertical scan is shown from the side, including the water level within the tank and the coordinate system used for all measurements.

the receiver was a piezo-element mounted in the IceMole-head.
The signals were created by a frequency generator with a given frequency in the range of 3 kHz to 20 kHz with a length given by a gate provided either by a second frequency generator or by an arbitrary function generator. The second frequency generator provided the gate every 1 s and the arbitrary function generator every 0.2 s. The signal coming from the first frequency generator is then passed through the Central Transducer Unit (CTU) to a Frontend Trasducer Unit (FTU) where it gets amplified before being sent to the emitting transducer. Before passing through the CTU it also gets read out by a digital oscilloscope to monitor not only the received signals but also the sent ones.
When an ITC-1001 is used as receiver a second FTU is used for amplifying that signal. From the FTU the signal is sent to the CTU and from there it is read out using the digital oscilloscope. In case the IceMole-head is used as the receiver instead of the FTU and the CTU, a separate preamplifier (1:100) powered by a 12 V battery is used for magnifying the signal before reading it out.

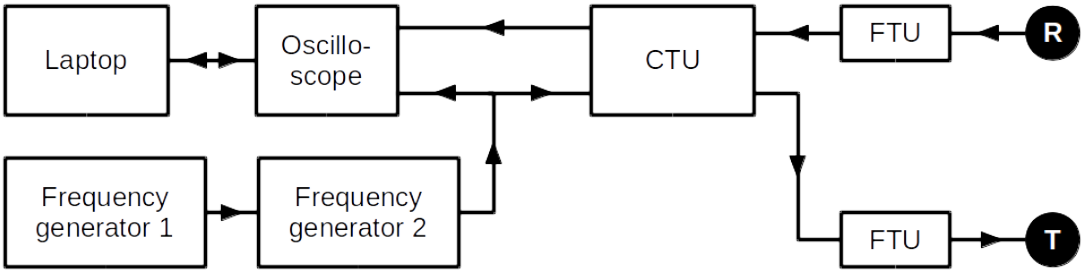

FIGURE 6.3: Scetch of the electronics used in the measurements with an ITC-1001 as receiver within the water tank.

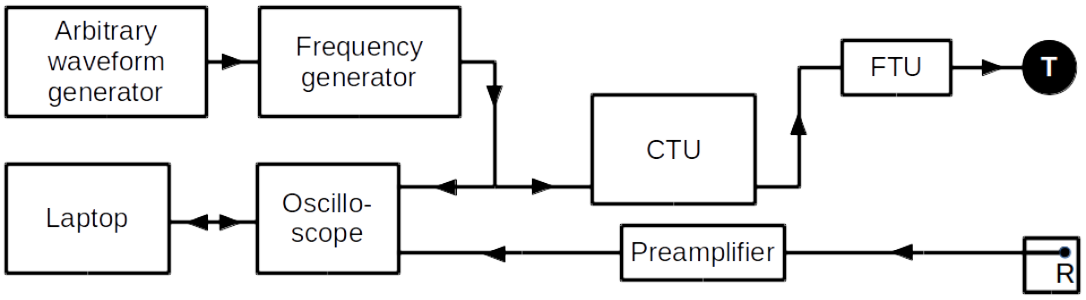

FIGURE 6.4: Scetch of the electronics used in the measurements with the IceMole-head within the water tank.

6.2.2 Electronic frequency response

In order to achieve an understanding of the frequency behavior of the entire system, the electronics frequency behavior has to be determined seperately from the frequency behavior of the actual transducers. To do this all modules forming the electronics were analyzed. The measurements performed to gain such an understanding are described in this section.

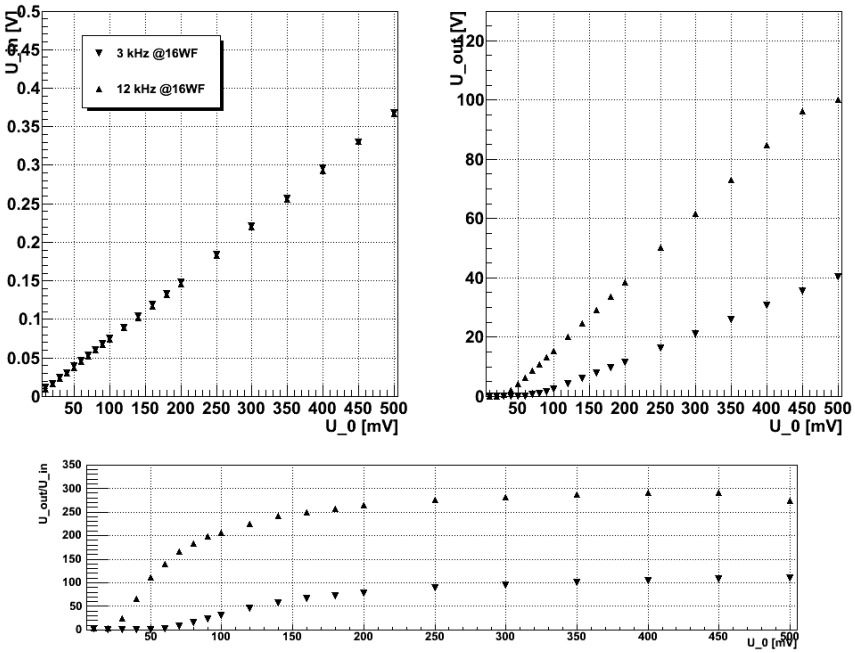

FIGURE 6.5: Influence of the amplitude of the input signal U_0 for 3 kHz and 12 kHz at a signal length of 16 sine waves. The upper left plot shows the dependence of the CTU of U_0, the upper right plot the same for FTU 5, and the lower plot the amplification factor calculated from the ratio of U_{out} and U_{in}.

The first series of measurements addresses the transmitting part of the electronics. The setup of this part is the same as the one described above (see Figure 6.3), however instead of reading out the voltage coming from the receiver the signal is recorded either after the CTU (U_{in}) or after the FTU (U_{out}) in the sending chain. Since the FTU amplifies the

signal to values above the limit of the digital oscilloscope of ±10 V a 10:1-probe head for reading out after the FTU was used.

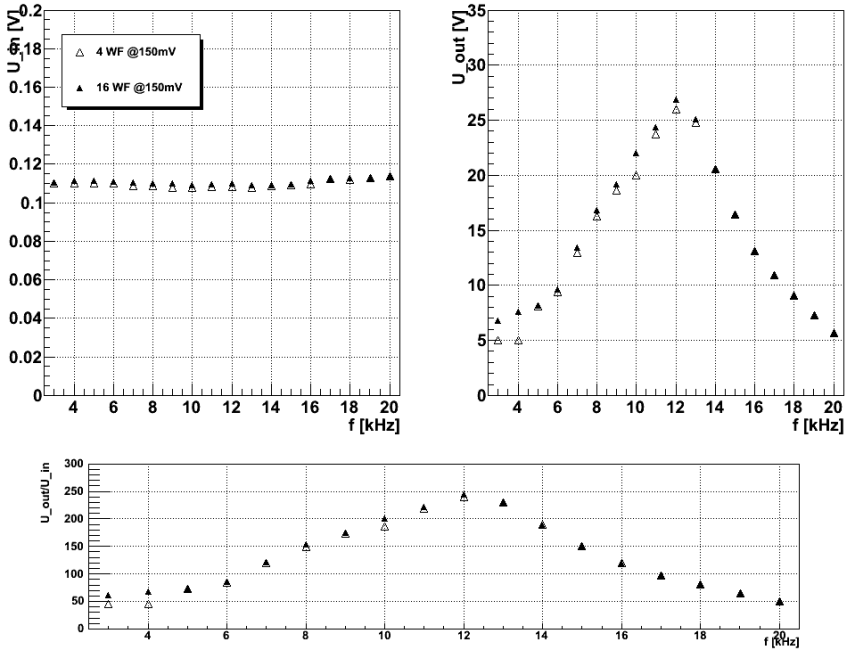

FIGURE 6.6: Influence of the frequency of the input signal for 4 sine waves and 12 sine waves with an input amplitude of 150 mV. Again the data on the left side was measured in between the CTU and the FTU 5 and the data on right side is the signal coming out of the FTU 5. The plot below shows the amplification factor calculated by dividing the output voltage of FTU 5 by the incoming voltage after the CTU.

Figure 6.5 shows the dependency of the input voltage that goes into the CTU for two different frequencies (3 kHz and 12 kHz). As expected the signals coming from the CTU are proportional to the input voltage (see upper left plot). The offset on the x-axis in the upper right plot shows that the FTU needs a minimal input voltage in order to create any output at all. When the voltage is high enough the output of the FTU is also proportional to the input voltage for a fixed frequency. The output of the CTU and the minimal voltage required by the FTU are both different for 3 kHz and 12 kHz. As can be seen in the lower plot, of course only when U_0 exceeds the minimal voltage required by the FTU, an amplification of the signal can be observed. After a transition zone up to ~ 200 mV the amplification factor remains constant for each frequency. This means the system should be operated not below this minimal voltage.
During all field tests this requirement was fullfilled since the U_0 was approximately 1 V. Due to saturation at frequencies around 12 kHz in the watertank the amplitude was reduced to 150 mV.
To further study the frequency dependence of both CTU and FTUs the signals after CTU and FTU were measured for all frequencies between 3 and 20 kHz. For FTU 5 this was done for two different signal lengths (4 and 16 sine waves) with an input voltage of 150 mV. The results are shown in Figure 6.6 and 6.7.
In the upper left plot of Figure 6.6 one can see, that the output signal of the CTU is almost independent of the frequency. The output signal of FTU 5 on the other hand shows a strong frequency dependency with a peak around 12 kHz (see upper right plot).

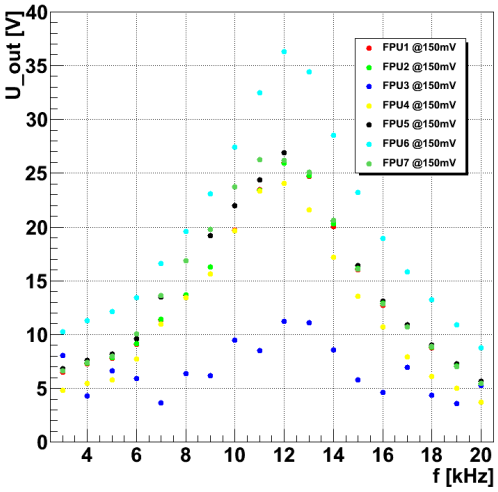

FIGURE 6.7: Comparison of all FTUs in the transmitting direction. All signals were measured after the connected FTU. The input signal had an amplitude of 150 mV and a length of 16 sine waves.

This behavior can also be observed when looking at the amplification factor displayed in the lower plot of Figure 6.6. When comparing the amplitudes for different signal lengths no significant differences could be observed. The differing points at 3, 4, and 10 kHz were caused by an overfluctuation of the first peak of the 16 wave long signal.
Figure 6.7 shows the comparison of the transmitted frequency response of all FTUs. In the case of FTU 3 the noise was as high as most of the signals which made a reliable determination of the signal's amplitude impossible. The frequency responses of the other FTUs are very similar in shape and, except for FTU 6, also in amplitude. For unknown reasons FTU 6 delivers a higher amplitude than the other FTUs, which has to be taken into account when FTU 6 was used during glacier measurements. In order to do so correction factors for all FTUs were calculated using FTU 2 at 17 kHz as a reference. These factors are summarized in Table B.2 in Appendix B and applied to the relevant data sets from field test 1.0. In the lab only FTU 4 was used to avoid saturation.

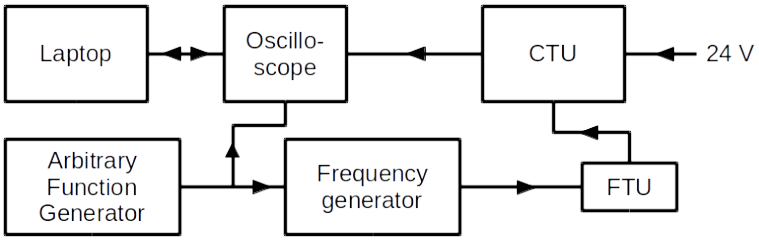

FIGURE 6.8: Scetch of the electronics used for the measurements of the frequency response of the receiving device, in this case our FTU.

The setup for measuring the receiving frequency behavior of all FTUs is shown in Figure 6.8. To measure the behavior of the premaplifier, it was placed between the frequency generator and the oscilloscope, replacing CTU and FTU in Figure 6.8. To adjust for the higher amplitude a 10:1 probe was used on the oscilloscope. Here the arbitrary function generator and the frequency generator were used to simulate received signals with a known frequency and amplitude that are fed into the receiving device. The readout of

these signals is done by a digital oscilloscope and a laptop. The signals created have a length of 16 waves and an amplitude of 10 mV for the FTUs and 50 mV for the preamplifier.

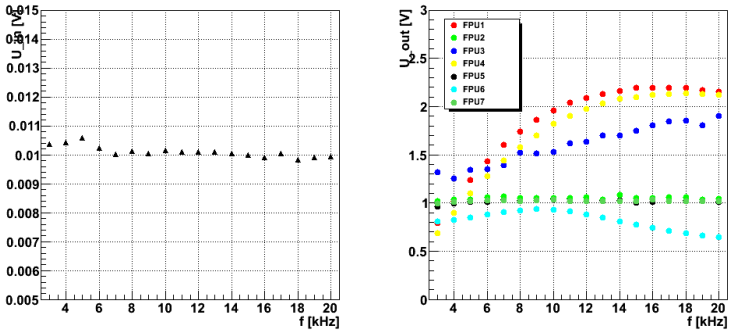

FIGURE 6.9: Comparison of all FTUs in the receiving direction. All signals were measured after the connected FTU. The input signal had an amplitude of 10 mV and a length of 16 sine waves.

The results for the FTUs are shown in Figure 6.9. The left plot shows the signal that is fed into the FTUs and the right plot the signals coming out of the various FTUs. The incoming signal generated by the frequency generator is mostly stable and independent of the frequency. The signals coming out of the FTUs on the other hand show a more individual behavior. While FTU 2, 5, and 7 are stable, the remaining FTUs 1, 3, 4 and 6 all react differently. For FTU 1 and 4 the amplification increases until it becomes stable at frequencies above 12 kHz. FTU 3 shows an almost linear increase in the complete frequency range with a few fluctuations and for FTU 6 the amplification decreases after an initial increase up to 9 kHz. The overall amplification remains below the intended amplification factor of 100 for FTU 6.
Since the FTUs show such individual frequency responses, this has to be taken into account when using them as receivers and comparing amplitudes recorded with different FTUs. This was only the case for the measurements recorded during field test 1.0 on the Morteratsch glacier. The data from the field test was corrected by the correction factors calculated from the data shown in Figure 6.9 using FTU 2 at 17 kHz as a reference point, which are summarized in Table B.3 in Appendix B.

The frequency response of the preamplifier used to read out the piezo mounted in the IceMole-head is shown in Figure 6.10. The measured amplification factor does not match the factor the preamplifier was designed for. According to the manufacturer specifications provided it should amplify signals by a factor of 100, while in reality the factor is closer to 28. However since the signals were still clear and well above the noise, there was no need to correct this on the hardware side. When looking at the frequency response only a small decrease of the amplitude at higher frequencies can be observed, which is not significant and can be neglected in the analysis.

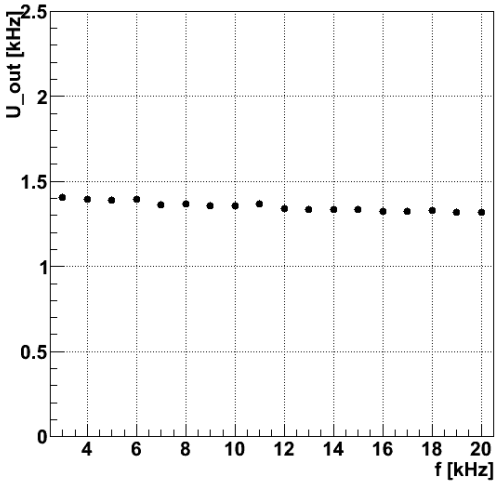

FIGURE 6.10: Frequency response of the preamplifier. All signals were measured after the connected FTU. The input signal had an amplitude of 50 mV and a length of 16 sine waves.

6.2.3 Resonance frequency of ITC-1001

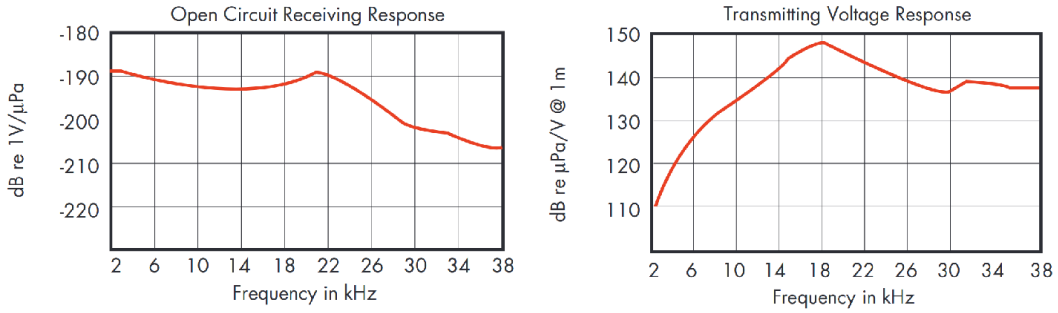

FIGURE 6.11: Frequency response of the ITC-1001. The left plot shows the response for receiving signals and the right plot for sending signals [7].

In addition to the frequency behavior of the electronics it is also neccessary to account for the frequency response of the transmitter. Information on this can be obtained from the datasheet of the ITC-1001 (see Figure 6.11). In the relevant frequency range between 3 and 20 kHz the receiving curve is almost flat, so there are no corrections neccessary. The sending curve shows a peak at 18 kHz. In order to correct all measurements that compare signal amplitudes with different frequencies the correction factors given in Table

B.1 in Appendix B have to be applied. They were obtained from the transmitting curve in Figure 6.11 with 17 kHz as the reference frequency.

6.2.4 Comparison with IceMole head

In order to be able to measure signals with the IceMole-head in water it is neccessary to ensure its watertightness. In this test campaign the head was separated from the probe. Hence the whole head was placed in a plastic bag. To test if this changes the frequency response, the waterproof ITC-1001, with and without two different plastic bags, was placed into the testing facility. Of course it is not possible to compare measurements of the head itself with and without a plastic bag, so these measurements were performed with an ITC-1001 instead. The two options for the plastic bag were commercially available trash bags with different thicknesses. The thinner one was green and the thicker one blue.

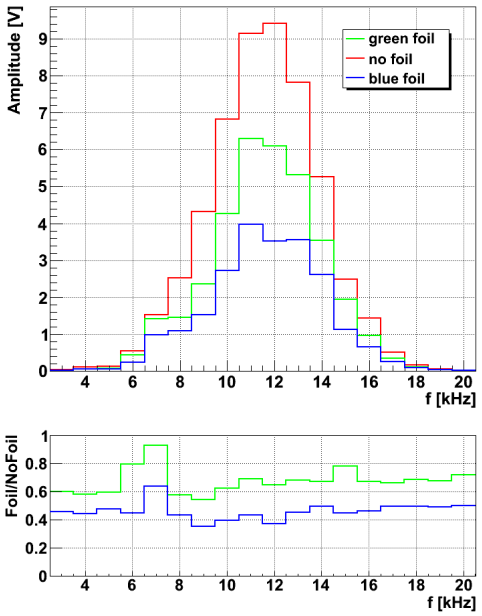

FIGURE 6.12: Influence of the plastic bag on the frequency behavior for the ITC-1001. The upper plot shows the amplitude of the signals against the frequency for different bags and without a bag. In the lowerplot the ratio of the signals with foil and the signals without the foil for all frequencies is diplayed.

As can be seen from the upper plot in Figure 6.12 the frequency profile looks similar to the output profile of the FTUs not only without the foil but also when different bags are used. As expected only a small reduction of the signals height can be observed. The direct comparison of the signals with and without a plastic bag shows a more or less flat behavior, except for a small peak around 7 kHz for both bags. Since the green bag leads to a smaller signal reduction for the measurements with the IceMole-head only the green bag has subsequently been used.

In order to get meaningful information the amplitudes measured with the IceMole-Head or an ITC have to be corrected by a few factors:

$$U_{\text{corrected}} = f_{\text{SendingElectronics}} * f_{\text{SendingITC}} * f_{\text{ReceivingElectronics}} * U_{\text{measured}} \tag{6.1}$$

The first factor $f_{\text{SendingElectronics}}$ stands for the influence of the electronics used to generate the signals that are sent to the emitting FTU. This includes the influence of different transmitting voltages and also frequency dependencies of the transmitting FTUs, which are described above. The second factor $f_{\text{SendingITC}}$ accounts for the frequency response of the actual transducer, here the ITC-1001, as given in its datasheet. The last factor $f_{\text{ReceivingElectronics}}$ reflects the influence of the electronics that process the received signals. That can be either the preamplifier or the FTUs used in receiving mode. Tables containing these factors are given in Appendix B.

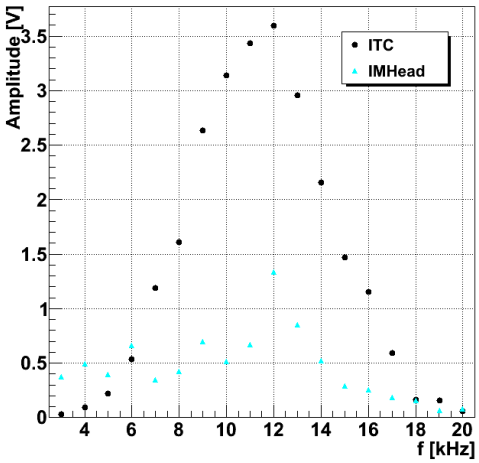

FIGURE 6.13: Comparison of the ITC-1001 with the IM-Head. Shown are the corrected amplitudes of both receivers for different frequencies.

For the comparison of the IceMole-Head with the ITC-1001 as a receiver, in addition the various amplification factors of the FTU (100) and the preamplifier (28) have to be considered. For this the amplitudes measured with the ITC-1001 are multiplied by an additional factor of 28/100. The result in shown in Figure 6.13.
Although the data points were corrected for the frequency response of the sending FTU and the emitter the receiving ITC-1001 still shows a peak at 12 kHz. For the IceMole-Head that peak is not as strong but also visible. One interpretation is, that both receivers are actually more sensitive at this frequency. However, since the known receiving frequency response of the ITC-1001 (Figure 6.11) looks very different this seems unlikely. A more probable reason for this behavior is, that the correction factors are insufficient. Especially the ones for the actual emitter were only read from the graph given in the datasheet, which are not verified and might not be accurate enough.
Despite this inaccuracy it is still safe to say, that the signals received by the piezo mounted in the IceMole-Head are much weaker than the ones recorded with the ITC-1001 for most frequencies. Only at very small and very high frequencies the measured amplitudes are comparable or even higher than the ones of the ITC-1001. This could be an explanation on why the IceMole has not been able to record signals at the largest distances.

TABLE 6.1: Coordinates of the transmitting ITC-1001 in the horizontal (left) and vertical (right) scan of the IceMole-head. The uncertainty in x-, y- and z-direction is 1 cm.

α [°]	x_{ITC} [cm]	y_{ITC} [cm]
0	81	84
15	79	68
30	73	51
45	61	38
60	47	27
75	30	20
90	13	17

β [°]	y_{ITC} [cm]	z_{ITC} [cm]
0	17	55
15	19	73
30	26	89
45	37	103
60	51	114
75	67	121
90	80	123

In order to now investigate directional and frequency dependecies of only the IceMole-Head, it was inserted in the water tank at a fixed position of:

$$x_{\mathrm{IM}} = 13 \pm 1 \text{ cm},$$
$$y_{\mathrm{IM}} = 85 \pm 1 \text{ cm},$$
$$z_{\mathrm{IM}} = 55 \pm 1 \text{ cm}.$$

For adressing different angles, the emitter was then inserted at different positions in the watertank. The coordinates for all measured angles are given in Tables 6.1. For each of these positions one signal for all frequencies from 3 kHz to 20 kHz with a step size of 1 kHz has been recorded.

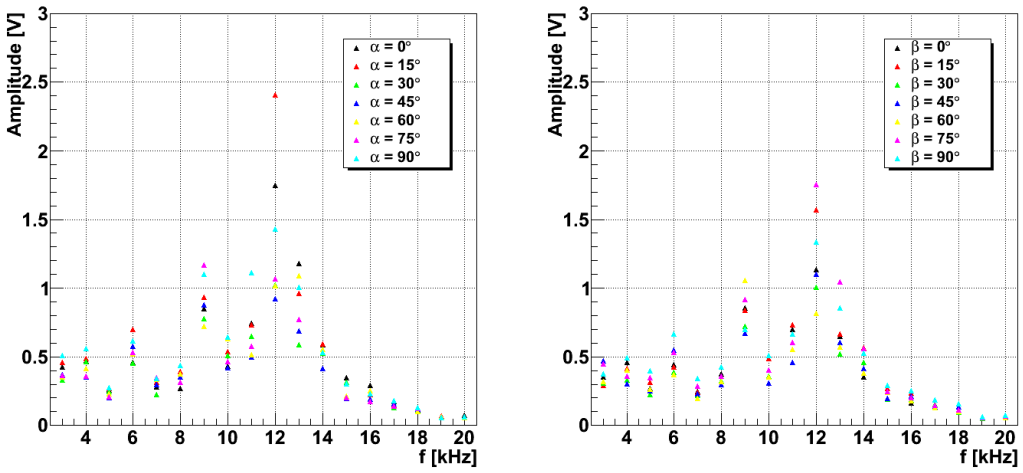

FIGURE 6.14: Frequency dependency of the IceMole-Head for all measured angles. The amplitudes after applying all previously described corrections of the horizontal scan (left) and of the vertical scan (right) are shown.

The resulting amplitudes are shown in the plots in Figure 6.14. As before one can see a peak at 12 kHz in both distributions, which is masking a possible frequency dependency of the IM-Head in this range. The only two other frequencies which are favored besides the main peak are 6 kHz and 9 kHz. At frequencies above the main peak no more

peaks can be observed and the amplitudes gets reduced in agreement with the frequency response of the FTU.

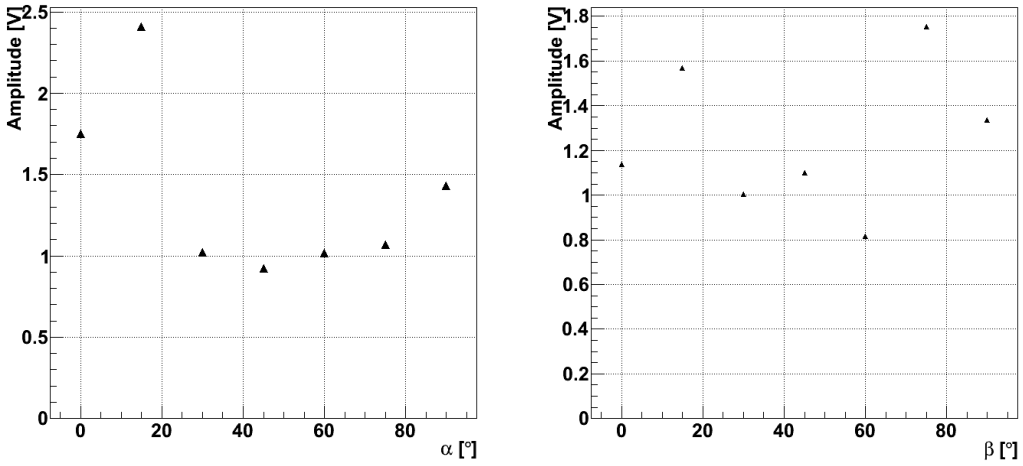

FIGURE 6.15: Directional dependencies of the IceMole-Head at 12 kHz. Left: Horizontal scan. Right: Vertical scan.

For the analysis of the directional dependecies the amplitudes of the measured signals were plotted against the angle at which they were recorded for each frequency separately. For 12 kHz these plots are shown in Figure 6.15 and the plots for all other frequencies can be found in Appendix B. Although most of these plots show fluctuations of more than 50 % depending on the angle, no pattern in dependency of the angle seems to exist. Instead, the measurement seems to be dominated by effects of the small test features, for example reflections of the tank wall or the water surface.

6.3 Coupling to the ice

As phase transitions have a strong effect on acoustic signals, properly coupling the transducer and receiver to the transport medium is necessary. For ice there are two options: Letting the transducers freeze into the medium or using some gel or liquid around the transducer to ensure good contact with the medium. To avoid pollution of the glaciers, especially during field test 3.0 at the Blood Falls, using a gel or liquid other than water was not an option.

6.3.1 Influence of water filled holes on propagation time

During the field test on temperate glaciers the coupling was realized via water filled holes. This has the advantage, that one can be sure that there is no significant amount of air absorbing much of the signal. Therefore this leads to a relatively well defined coupling between transducer and ice. On the other hand inserting a transducer into a water filled hole has the disadvantage that it remains unclear how much water the acoustic signal has to pass through before it enters the ice. Since the speed of sound in water at 0 °C is 1485 m/s [49], much slower than the speed of sound in ice, this has an effect on the total propagation time.
The diameters of the holes during all field tests were between 15 cm and $\sim$ 20 cm. Since the diameter of the transducers was only 10 cm in the worst case, when the emitter is

TABLE 6.2: Influence of the position and direction of the waterhole.

α[°]	90	85	80	75	70	65	60
Δt[ms]	0.0673	0.0676	0.0684	0.0697	0.0717	0.0743	0.0778

touching one wall in a wide hole and the receiver is in the opposite direction, there is a 10 cm distance between emitter and the closest point where the sound could enter the ice. If emitter and receiver are at different heights the soundwaves have to propagate through even more water since the angle between the dircet line and the wall of the hole is increased.
This effect was calculated for angles between 90° and 60°. The changes of the signal propagation time Δt caused by only one hole can be found in Table 6.2. In reality changes twice as big can occur, since both emitter and receiver are inserted in separate holes. Compared to the required accuracy of the propagation time of 1 µs from Chapter 3 this value is far too large. This means, that calculating the position of the IceMole, the propagation time has to be correct for. For the measurements between the transducers the error can be minimized by inserting all transducers at the same depth.

6.3.2 Direct comparison

The transition from transducers in water filled holes to frozen in transducers was studied in the laboratory. For this a rectangular container with a base area of 0.56 m × 0.36 m was filled with water and put into a freezer until the water was completely frozen. Then two holes were drilled into the ice at a distance of 0.36 m. Into the first hole an ITC-1001 was inserted while into the second hole a SQ09 was placed. Both holes were filled with water afterwards. The ITC-1001 was used as the emitter and the SQ09 as the receiver. The signals received by the SQ09 were fed to a suitable preamplifier before being recorded with a digital oscilloscope. Over a time window of ∼ 31 hours signals were recorded at twelve different times to monitor the freezing process. A summary of these times by Data ID is given in Table D.1 in Appendix B.

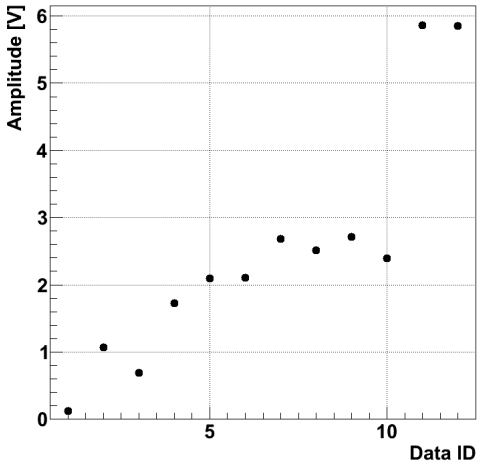

FIGURE 6.16: Amplitudes recorded during the freezing process in the laboratory.

For each of the recorded signals the amplitude was determined. The results are shown in Figure 6.16. During the first ~ 9 h signals were recorded approximately once per hour and although there are some fluctuations overall the signal strengths improves while the water freezes. The first exception is at data point 3. An explanation for this reduction is, that during the freezing process new cracks in the ice are created and through these some of the not yet frozen water can leak out of the holes with the result, that the coupling gets reduced. This is also the reason, that between measurement 9 and 10 the holes were filled with additional water, until the waterline was 4 cm higher. One can see from the plot, that this caused an immediate drop in the signal amplitude within the 10 min between both recordings. Between point 10 and 11 ~ 19 h had passed and the freezing process was completed. Here the maximum amplitude is already reached and waiting 3 more hours does not change the amplitude anymore.
Overall the coupling by frozen in transducers is much more efficient than that by water filled holes, given the contact between ice and transducers is ensured.

6.3.3 Glacier measurements

During field test 2.0 the coupling was actually done by freezing in the transducers (see Figure 6.17), however in contrast to the expectations from the lab-measurements the observed signal strengths was very low. In Figure 6.18 the complete data set for all combinations during this field test are shown. The maximum distance here was 13 m, a distance at which on every other test site pulses with a good signal-to-noise ratio (SNR) could be observed. Here only six combinations of signals are recognizable by the bare eye ($1 \leftrightarrow 6$, $2 \leftrightarrow 5$, $3 \leftrightarrow 4$, $3 \leftrightarrow 5$, $3 \leftrightarrow 6$, $4 \leftrightarrow 5$) and the maximum distance for these combinations is 7.92 m for holes 2 and 5. The signals at greater distances are either lost or their signal quality is to low for a reliable determination of their arrival times. Therefor they are discarded for further analysis.

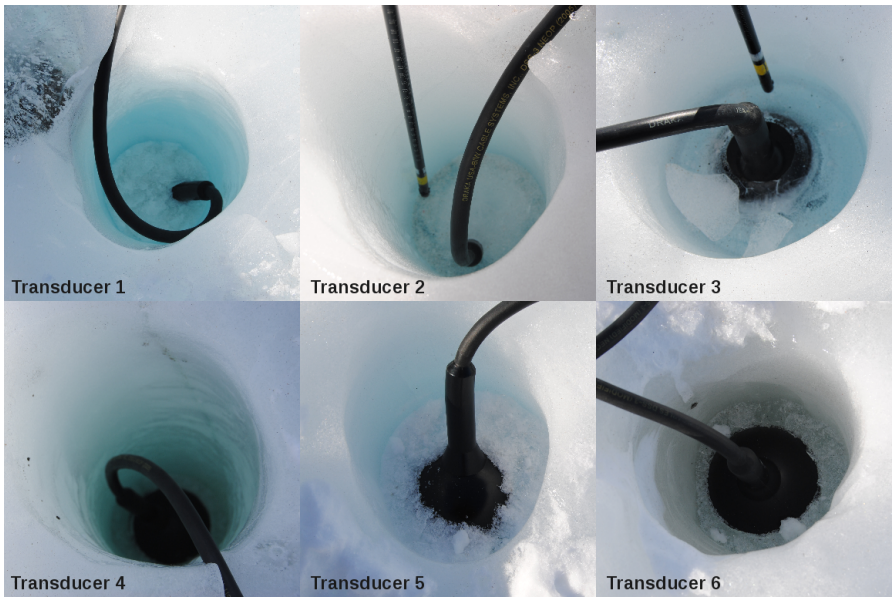

FIGURE 6.17: Coupling of the transducers during field test 2.0.

When looking at the amplitudes of those signals which could be observed they do not get reduced with distances as one could expect and are simply unsorted (Figure 6.19). The only explanation for this is an ill-defined coupling to the ice. If the transducers are

frozen in the ice and the direct contact between the ice and the transducer is disrupted this can lead to large losses and can explain why the pulses are no longer measurable by the other transducers. Since one can never be sure if the contact between transducer and ice is still ensured this form of coupling is not well defined and therefore not superior to water filled holes.

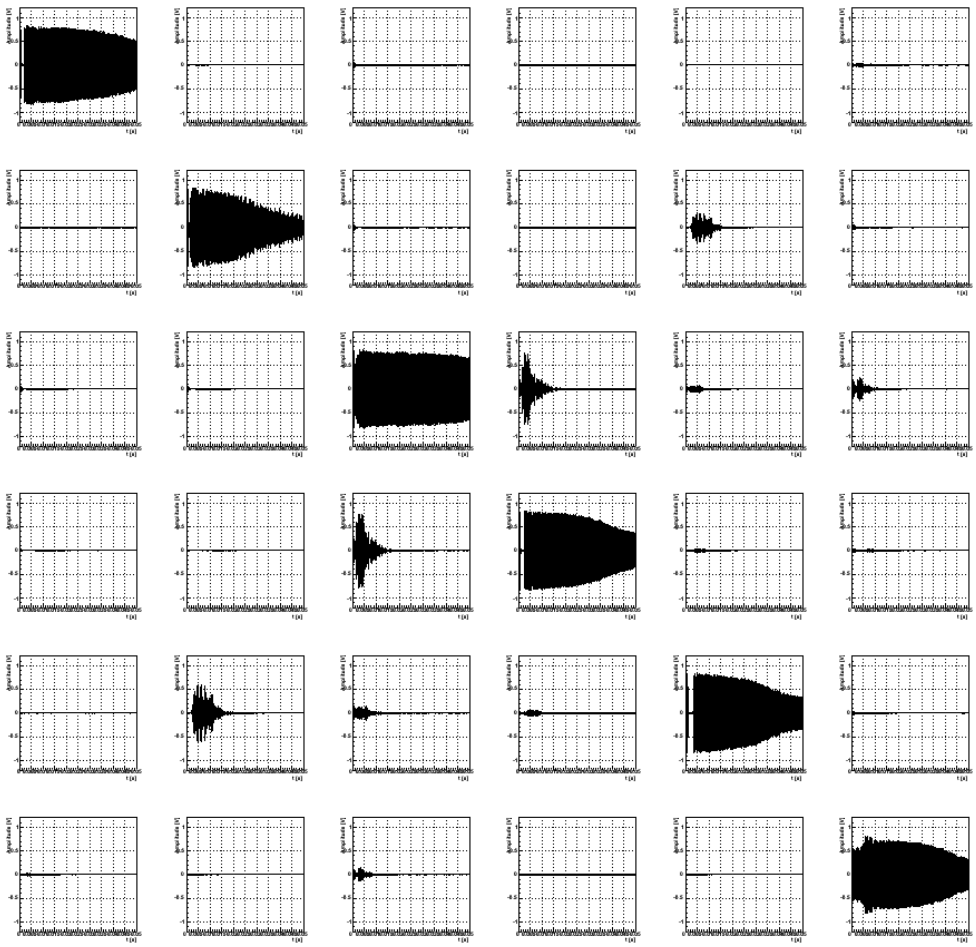

FIGURE 6.18: Complete data set of field test 2.0. The first row shows signals emitted by transducer 1, second those send by transducer 2 and so on. On the y-axis the measured amplitude is given in volt and on the x-axis the time in seconds is plotted.

To further investigate the coupling through water filled holes on a real glacier, nine additional measurements have been performed during field test 2.5. Three of them between holes 7 and 4 and six between holes 4 and 12. During these measurements the depth of either emitter or receiver was varied while the other one remained at maximum possible depth in its respective hole to see if this influences the signal strength and therefore the coupling. For the measurements between hole 7 and 4, and for three of the measurements between 4 and 12, the depth of the emitter was changed. For the other three measurements between hole 4 and 12 the depth of the receiver was unchanged. The widths of the resulting waveforms are given in Figure 6.20.
As one can see from the two measurements with the varying depth of the sending transducer the signal strength increases with the depth. The maximum depth of these holes was 40 cm for hole 7 and 70 cm for hole 12. At that range this is probably still an

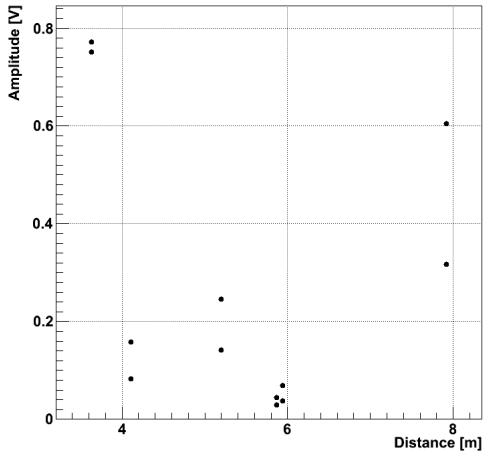

FIGURE 6.19: Signal amplitudes from all visible signals during field test 2.0 sorted by distance.

indication, that the signal strength is increased with the ice quality. So close to the surface it is still possible that the pulses are being transmitted through a firn layer and not yet through clear ice, which means the deeper the transducer is inserted the higher the signal strength gets.

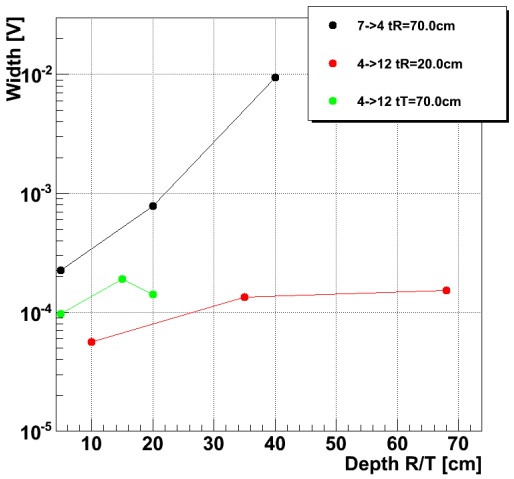

FIGURE 6.20: Signal strength for three hole combination during field test 2.5 with a varying depth of either transducer or receiver.

The third measurement with the varying depth of the receiver shows that after the expected initial increase of the width it gets reduced again, when the receiver hits the bottom of hole 12 at 20 cm. This means, instead of inserting the transducers all the way to the bottom of their holes, it can be an advantage to lift them up a few centimeters and let them float in their holes.

Chapter 7

Measuring ice properties

The scenario described in Section 2.2 requires a solid understanding of the properties of the surrounding ice. Especially for the acoustic positioning system a solid understanding of the expected ice properties is essential. That means information on the directional dependencies and uncertainties of the speed of sound is needed as well as an estimate of the attenuation length in ice, which limits the reach of the system and defines the optimal distance between the transducers.

7.1 Data processing

Due to absorption and scattering effects the signals measured in ice are harder to process than those from water measurements. One has to deal with increased noise and smaller signal amplitudes especially at larger distances. In order to be able to use also data from the largest possible distances a data processing procedure is important, that is functioning even at the largest distances in ice.

7.1.1 Frequency filter and Background subtraction

The steps of the data processing are shown in Figure 7.1. The starting point is the raw waveform returned by the CTU.

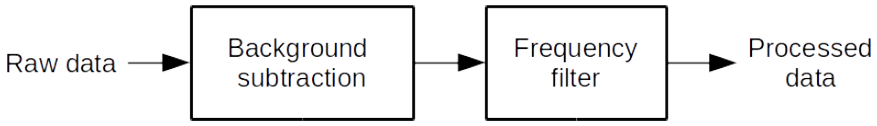

FIGURE 7.1: Steps of data processing. First a the background is subtracted and then a frequency filter is applied.

The first step is to subtract the background. The background is determined for each waveform individually by calculating the sum of all signal heights over all measured points and dividing that sum by the number N of points.
The next step is to get rid of as much noise as possibly by applying digital frequency filters. The design of all filters was done using the WinFilter-software [50]. The filters were designed to let only frequencies in a band of ± 1 kHz around the send frequency pass. First a low-pass and in the second step a high-pass is applied. In order to find the optimal filter several filter options were considered and tested on a clear signal from field test 1.0 (see Figure 7.4).

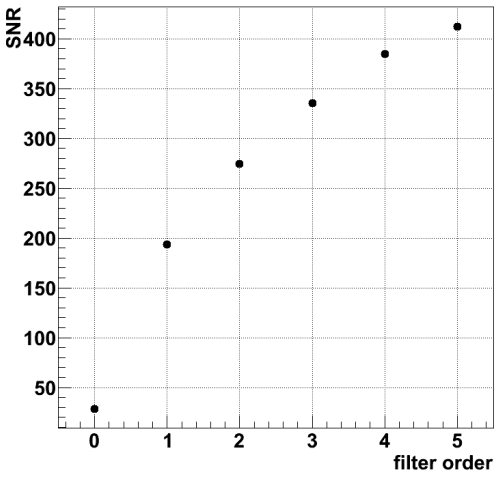

FIGURE 7.2: SNR in dependence of the filter order for the Butterworth filter. The point at order 0 corresponds to the unfiltered signal.

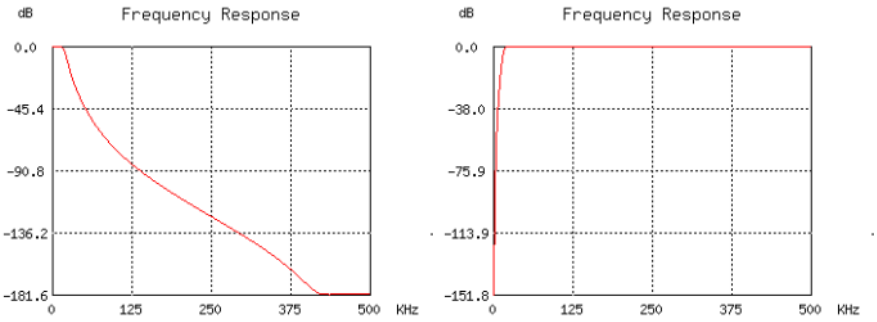

FIGURE 7.3: Example of a Butterworth filter of the order 5 for a sampling rate of 1000 kHz. On the left side the frequency response of a 18 kHz low-pass filter is shown and the right plot shows the frequency response for the respective 18 kHz high-pass filter.

The first choice was between an IIR-filter (Infinite Impulse Response) and a FIR-filter (Finite Impulse Response). When all other parameters where kept the same the IRR-filter produced an eight times higher SNR. The next step is to chose between a Chebychev, a Butterworth and a Bessel filter. A detailed description of these filter types can be found in [51]. The Bessel filter has the widest transition band which is not ideal for the purpose of letting only the send frequency pass. The Chebychev filter is designed to have the steepest slope in the transition zone, but this ideal feature comes with a more bumpy behavior in the actual band-pass and was therefor discarded as an option. The Butterworth filter is designed to be flat in the band-pass region and the steepness of its transition band can be adjusted by a higher filter order until it is sufficiently steep. In Figure 7.2 the improvement of the SNR with an higher filter order is shown. As expected a higher filter order leads to a better signal quality. Due to unstable behavior the filter order could not be increased over 5, which means this is the filter order used. When comparing the Butterworth and Chebychev filter at an order of 5 the SNR for the Chebychev is 429 while the Butterworth leads to an even higher SNR of 591. Therefor overall the decision was to use only Butterworth filters of the order 5, since they improve the signal quality sufficiently.

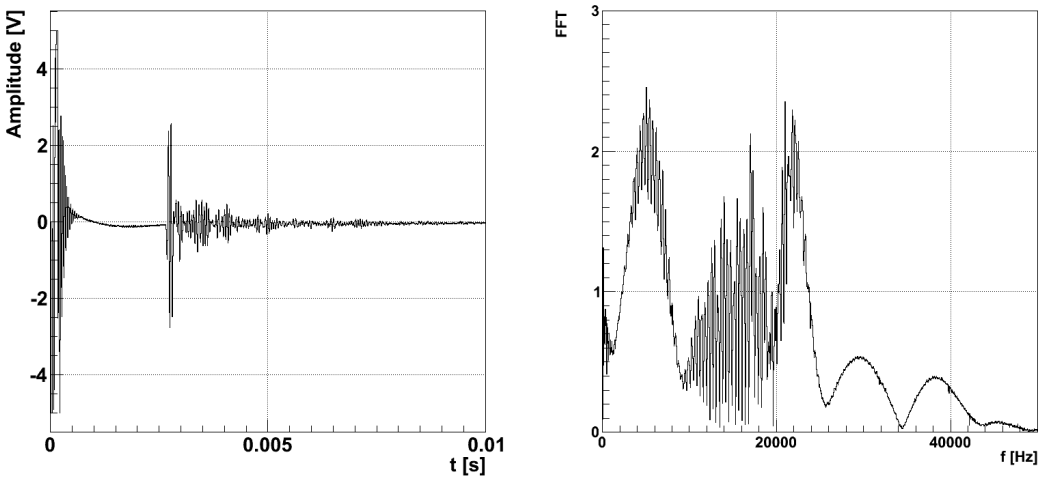

FIGURE 7.4: The left plot shows the signal region of the raw data sample from field test 1.0 that was used for finding the optimal filter. The actual signal begins around 0.0025 s and the pulse that can be seen at the start of the waveform is caused by the electrical connection between the receiver and the sending electronics. The right plot shows the relevant part of the corresponding frequency spectrum. Besides the 17 kHz that were send there are a lot of other frequencies disturbing the signal.

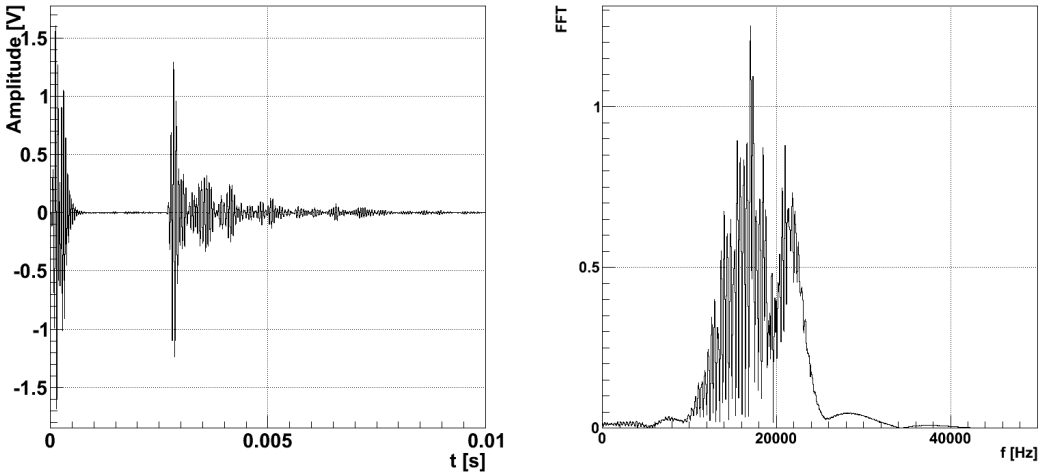

FIGURE 7.5: The left plot shows the processed data sample from field test 1.0 after both the low and the high-pass filter have been applied. Compared to the raw data shown in Figure 7.4 the signal looks much smoother and less disturbed by unwanted frequencies. The right plot shows the corresponding frequency spectrum. As expected only frequencies around 17 kHz remain and everything else is suppressed.

In Figure 7.3 an example of a Butterworth filter pair around a frequency of 17 kHz is shown. Both filters show the expected flat behavior in the passband and a steep transition band.
The comparison of the processed waveform in Figure 7.5 with the raw data in Figure 7.4 one can immediately see that the filter is doing exactly what it is supposed to. Only

frequencies around the send frequency of 17 kHz remain and the signal becomes much clearer, which can also be seen in the SNR that improves from 77 to 591.

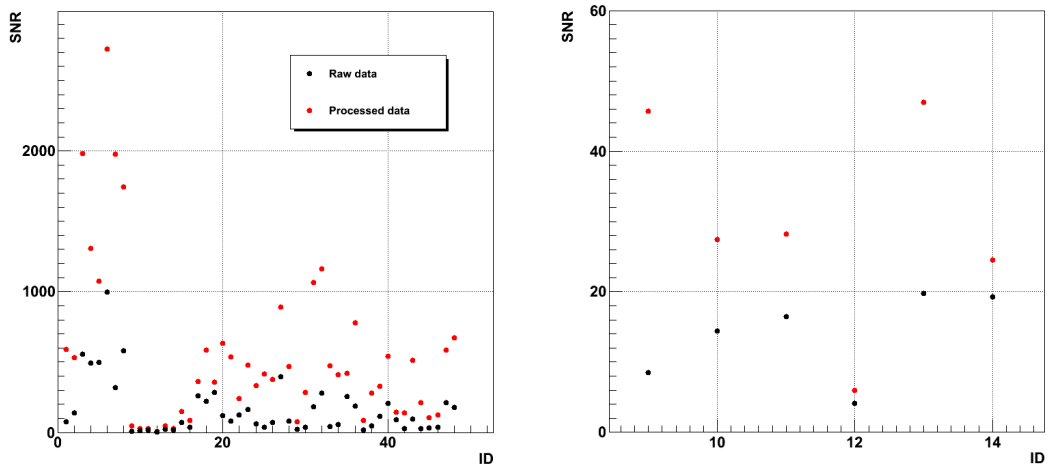

FIGURE 7.6: SNR for several data points from field test 1.0. The right plot shows a zoom of the region between ID 9 and 14.

Although the improvement is not equally large for all data points one can see in Figure 7.6 that there still is a significant improvement for all cases. Even the data points between data IDs 9 and 14, which have a lower SNR to begin with, improve sufficiently for the arrival time determination.

7.2 Influence of cracks

Every glacier is interspersed by cracks as the one shown in Figure 7.7. Although these cracks are very narrow they are still influencing the propagation of the acoustic waves through the ice. To estimate this influence two measures were taken. The first one was a simulation of an acoustic signal passing through such a crack and the second one was the comparison of signals that were recorded at similar distances with and without a crack.

FIGURE 7.7: Picture of a crack that was observed during FT-0.0.

7.2.1 Simulation

The purpose of this simulation is to get an idea of how much the propagation of sound waves is influences by cracks as the one shown in Figure 7.7.
It is done with a Matlab toolbox named k-Wave. k-Wave is a time-domain simulation that uses a numerical model based on equations 4.2, 4.3 and 4.4 [52]. The simulation

solves this coupled first order system of equations. This has three advantages. It allows for a simple inclusion of source terms in the conservation of mass equation as well as in the conservation of momentum. The computaion of pressure and particle velocity is possible on staggered grids, which improves the numerical accuracy. Perfectly matched layers (PML) can be used to absorb waves at the edges of the computational domain. Details on how the underlying model works can be found in [53].
To run a simulation one has to define the geometry of the computational domain, the duration of the simulation and the positions of sensors and sound sources. The geometry is given by the size of the computational domain and a definition of the medium for every cell within the domain. The medium is beeing defined via its speed of sound and its density. The positions of the sensors are beeing defined by a senor mask, which is a matrix of the same size as the computational domain with entries of 1, where particle velocity and pressure shall be recorded. For the source one can choose between the initial pressure distribution as an input or some time-variations of a source mask, which is defined in the same way as the sensor mask and then multiplied with a time dependent function.

This Simulation

For this simulation a computational domain with a size of 60 pixels in x and y and 100 pixels in z was created. Each pixel corresponds to 0.1 mm, resulting in a domain with a size of $0.6 \times 0.6 \times 1.0\,\mathrm{cm}^3$. Each cell within this domain is first declared to be ice and for the crack some of the pixels are then overwritten with the parameters for water or air, depending on the current run of the simulation. The parameters used for all three mediums are given in Table 7.1. As can be seen in the example of a water filled crack with a width of 0.1 mm in Figure 7.8, the crack is located in the middle of the computational domain in the x-y-plane. The PMLs are added automatically at the edges within the domain with a thickness of 10 pixels.

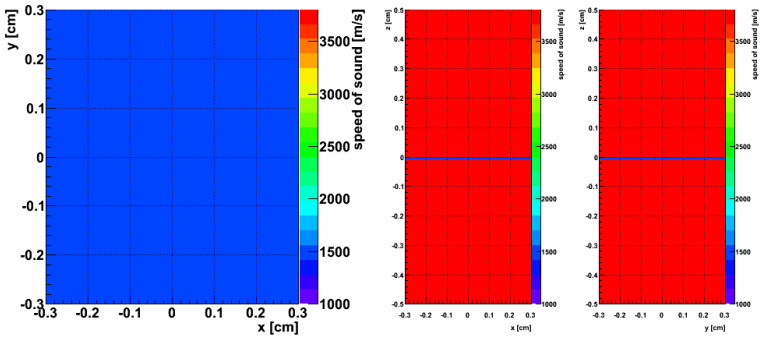

FIGURE 7.8: Velocity distribution in the computational domain for a water filled crack with a width of 0.1 mm. From left to right cross-sections through the center of the 3-dimensional domain are shown for the x-y-plane, the x-z-plane and the y-z-plane.

For the water filled crack, thicknesses varying between 0.1 mm and 1.0 mm were simulated. In addition, one simulation was done with an air filled crack and one without any crack. The positions of the sound source and the sensors were unchanged in all simulation-runs and can be seen in Figure 7.9. The source was choosen as an initial pressure distribution without any predefined time variation as a ball with a radius of 4 pixels located 20 pixels in z from the center of the computational domain and an initial

TABLE 7.1: Parameters for each medium used in the simulation.

Medium	Speed of sound [m/s]	Density [kg/m^3]
Ice	3700	916.7
Water	1485	602
Air	343	1.2

pressure amplitude of 5 Pa. For the sensors two positions were chosen. The first one in the same location as the center of the source and the second one in the same distance in z to the center on the other side of the crack. The duration of the simulation was set to 3 µs, which is enough time for the original acoustic pulse and possible refelctions to pass the second sensor.

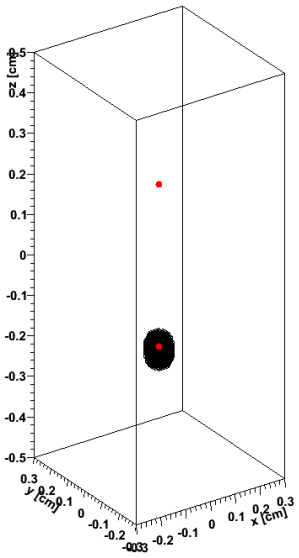

FIGURE 7.9: Geometry of the initial pressure distribution and the positions of the sensors. The black ball in the lower part is the area, where the initial pressure was 5 Pa and the red dots indicate the positions of the two sensors.

Results

The recorded waveforms for the water filled crack can be found in Figure 7.10. The left plot shows the pressure recorded by the sensor at the source for a crack width of 0.1 mm. One can clearly see the initial pressure of 5 Pa that immediately drops to −6 Pa, resulting in a bipolar pulse with a length of 0.2 µs. At approximately 1 µs a second pulse with a much smaller amplitude is visible, which corresponds to the reflection from the crack.
On the right hand side of Figure 7.10 the pulses recorded by the other sensor for different thicknesses of the crack are shown. The black curve is the signal that is recorded by sensor 2 when no crack is blocking the path. The amplitude of this curve can be used as

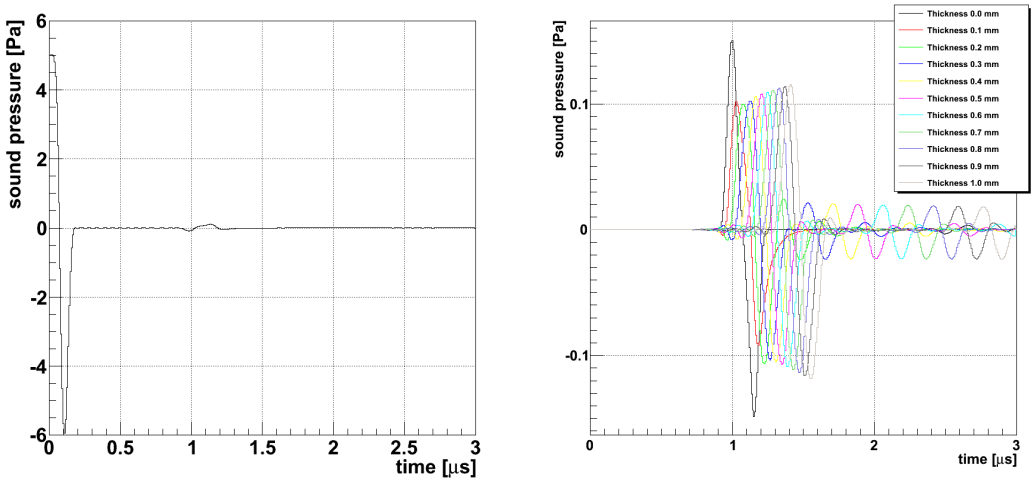

FIGURE 7.10: Waveforms recorded by the two sensors in the the simulation of a water filled crack. Left: Waveform of the sensor at the source. Right: Waeforms of the sensor on the other side of the crack for different widths of the crack.

a reference for the reduction of the signal strength caused by the respective crack. When looking at the other signals one can see, that a wider crack causes a shift of the arrival time towards higher values up to 0.5 µs. This is expected, because of the lower speed of sound in water.
Except for the signal belonging to the crack thickness of 0.1 mm, all other waveforms show a second bipolar pulse arriving even later than the first pulse with a further reduced amplitude. This second signal is caused by the original signals reflection of the second edge of the crack, that is then reflected again at the first wall before exiting the crack towards the second sensor. For a thickness of 0.1 mm this reflection arrives already while the first pulse is still fading. So it only causes a disturbance of the first pulse instead of beeing visible as a separate pulse.

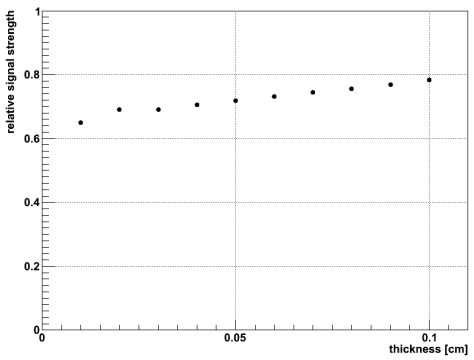

FIGURE 7.11: Relative signal strength of the waveforms recorded after the acoustic pulses have crossed the crack for different thicknesses of the crack.

In Figure 7.11 the relative signal strength, calculated by dividing each amplitude by the reference amplitude of the signal without a crack, of the pulses found in Figure 7.10 is shown. Because the distance the signals propagate through ice gets reduced by the

distance they propagate through water within the crack, a small increase of the signal strength for wider cracks is observed. Compared to the distance the signals propagate through the ice on a real testsite, the width of the cracks is neglectable, so that the influence of this can also be neglected in real measurements. The expected signal strength after a water filled crack therefore is about 65.03% of the signal strength without a crack at the same distance. For a crack that is filled with air, the effect of the crack is much higher and only 5.85% of the signals amplitude remain.

7.2.2 Measurements

For this analysis two combinations from field test 0.0 were picked. The first one without a crack between hole 1 and hole 0 with a distance of 4.28 ± 0.10 m and the second one with a crack between hole 3 and hole 0 at a distance of 3.90 ± 0.10 m. During this field test for each measurement 4 receivers were used and also the positions of the visible cracks on the test site were documented. The recorded waveforms for all 4 receivers for both combinations are shown in Figure 7.12.

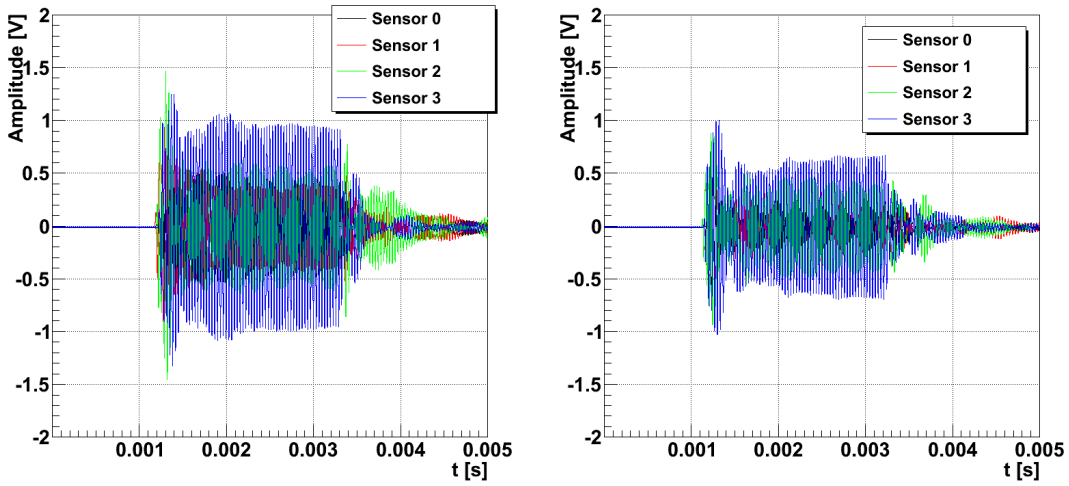

FIGURE 7.12: Comparison of two combinations from FT-0.0, one through a crack and one without a crack in the ice. On the left the signals without a crack are shown and on the right the ones with a crack.

Although the amplitudes of the signals originating in hole 3 are reduced compared to the ones originating in hole 1, both plots still show very clear signals for all receivers. The SNRs for all shown waveforms given in table 7.2, are all above 570 even before applying a frequency filter. For a better comparison the width of the signal region was calculated as described in section 7.4.1. The resulting values are also given in table 7.2. For both combinations the width increases with the sensor ID, meaning it decreases with the depth in the ice. Since the emitter was at a depth of 0.5 m this is probably caused by the increasing distance between emitter and receiver if the receiver is deeper in the ice. As can be seen also from the plots, the widths for the signals propagating through the crack are reduced for all receivers. By calculating the ratio of the widths with a crack and the ones without a crack one can see, that this reduction is pretty constant. The mean reduction for all receivers is 0.67 ± 0.01 and consistent with the range of the reduction obtained in the simulation of a water filled crack.
One should keep in mind, that this value was not corrected with respect to the slightly different distance of the two hole combinations. A correction was not possible, since

TABLE 7.2: Summary of the SNR and width values for the waveforms shown in Figure 7.12 and the ratio between the widths with and without crack.

	SNR		Width		
sensor	no crack	crack	no crack	crack	ratio
0	901	572	0.3147 V	0.2063 V	0.6555
1	626	602	0.3819 V	0.2627 V	0.6879
2	882	824	0.5217 V	0.3475 V	0.6661
3	1147	1095	0.6784 V	0.4531 V	0.6679

the attenuation length could not be determined for this test site. Also the attenuation lengths on the other test sites were determined including the influence of all the cracks present on the respective test site and only for lower frequencies, making these values inapplicable for the data used here.

7.3 Speed of sound

An exact determination of the speed of sound is one of the key points for positioning of the probe with an accuracy below 1 m. It requires a reliable determination of the signal propagation times between the transducers in addition to the measured transducer positions. According to the simulation described in Chapter 3 this determination needs to be accurate to a level of 5 µs.

7.3.1 Arrival time determination methods

This section describes the different methods tested to determine the arrival time of an acoustic signal. The methods are a simple threshold, the use of a cross correlation and the calculation of the Hilbert envelope in combination with a threshold.

Threshold

The idea of this method is finding the first time in the data, where the amplitude exceeds a given threshold. Since signal amplitude and noise vary from signal to signal this threshold is calculated individually for each signal. The most accurate approach is to calculate the threshold as a certain percentage of the maximal amplitude. This percentage should be as low as possible to avoid missing the first oscillations of the signal. In order to ensure the threshold is higher than the noise, the width of the noise is calculated for each waveform individually from a noise region. That region is calculated from the distance between the used holes and two intentionally too high values for the speed of sound, 5500 m/s for the lower limit and 4500 m/s for the higher limit. Only if the threshold is above five times that width this threshold is used. Otherwise the threshold is set to be five times the noise. The arrival time is then given by the first rise over that threshold. Figure 7.13 shows the steps of this method.
During some field tests the data shows a second pulse at the beginning of each waveform (see Figure 7.14). This pulse is caused by electro magnetic noise caused by the generation of the emitted pulse. To avoid this noise and also the noise region only the rise of the signal over the threshold after a certain time is used for the determination of the arrival

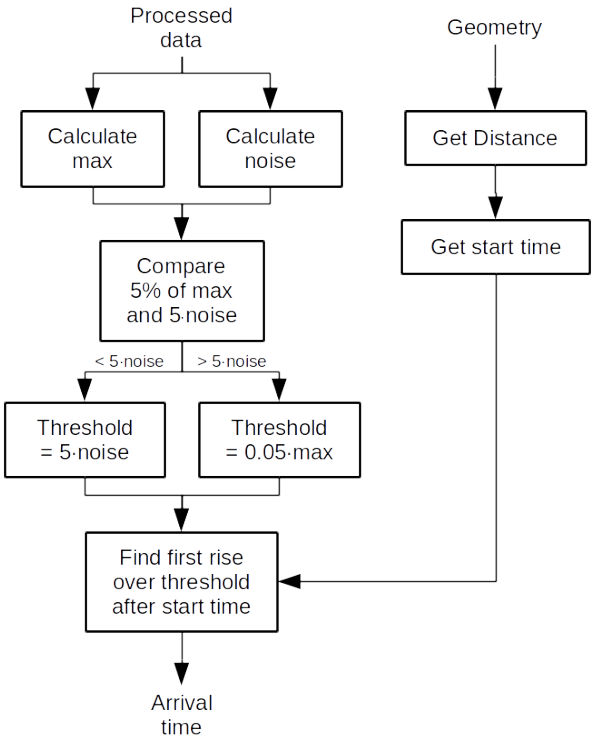

FIGURE 7.13: Steps of the threshold method for the determination of the arrival time.

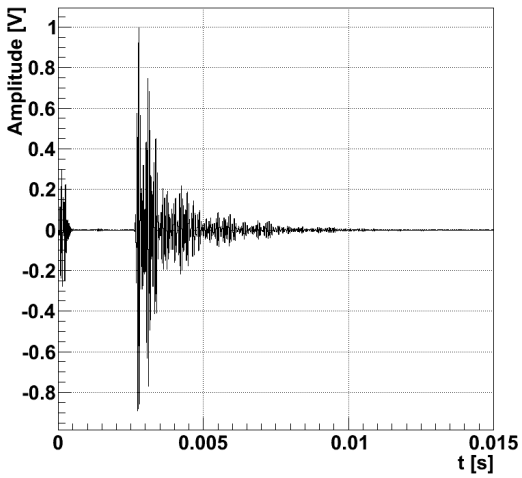

FIGURE 7.14: Complete waveform of a signal send over a distance of 9.90 m from hole 1 to hole 6 at a depth of 0.8 m.

time. This starting point is calculated from the known distance between the two relevant holes divided by the intentionally to high value of the speed of sound of 4500 m/s.
In order to optimize this method the arrival time was determined for two signals for a varying threshold. Once that variation was measured as a percentage of the maximum of the signal and once as a multiple of the noise. The result is shown in Figure 7.15. For the variation of the percentage one can see, that there are several points missing for 35 m-signal. This is because the threshold is lower than the noise, resulting in an arrival

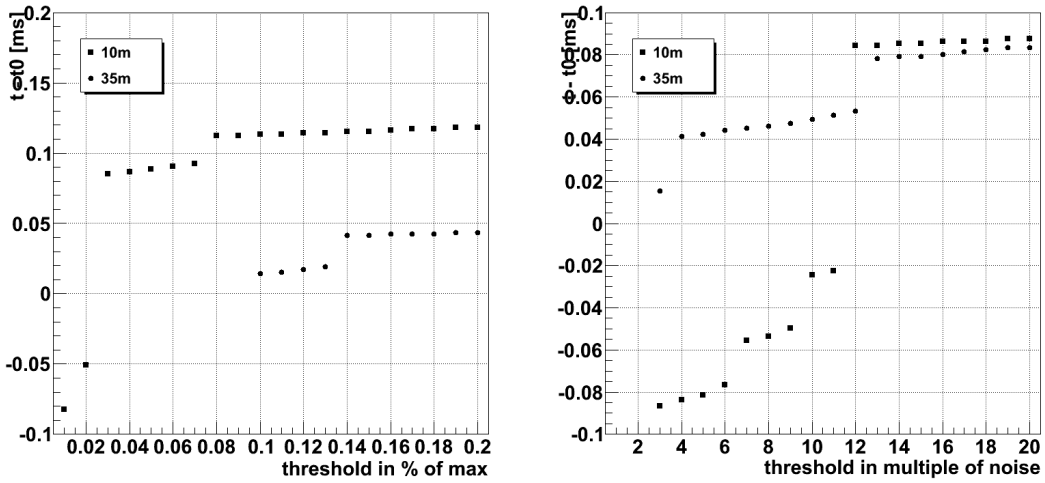

FIGURE 7.15: Optimization of the threshold for test-datasets 1 and 3 for the Threshold method. Left: Difference between the automatically determined arrival time t and the true arrival time t_0 for a threshold from different percentages of the maximum. Right: Same for a threshold from varying multiples of the noise.

time that differs more from the real arrival time than the plot range. That means for larger distances the threshold would have to be above 10% of the maximum. For the 10 m-signal, the best result is obtained when the threshold is only 2% of the maximum. When looking at the variation as a multiple of the noise there are missing data points for both signals. The reason here is again, that the threshold needs to be well above the noise, which is clearly not the case when the multiple is only one or two. Here the result for the 10 m-signal is best at a multiple of 11 and the result for the 35 m-signal is best at 3 and both signals show several random jumps. These jumps occur due to the bipolar shape of the signals and happen when the threshold exceeds the amplitude of an earlier oscillation and detects the next one.
Overall the best result for the 10 m-signal was obtained with 5%/*max*-threshold and the best result for the 35 m-signal with the $3 \cdot$noise-threshold. Due to the random jumps in both threshold-optimization-plots for the automated determination values for the thresholds were chosen that lie on a plateau, namely either 5% of the maximum or 5 times the noise.
To test how well this method works the arrival times t determined automatically were compared with the real arrival times t_0 for all datasets from table 7.3. These "real" arrival times were read by eye directly from the zoomed in waveforms. All deviations remain below 42 ms. In average the absolute value of the deviation is 14.87 µs, which can be seen as a measure of the uncertainty of this method.

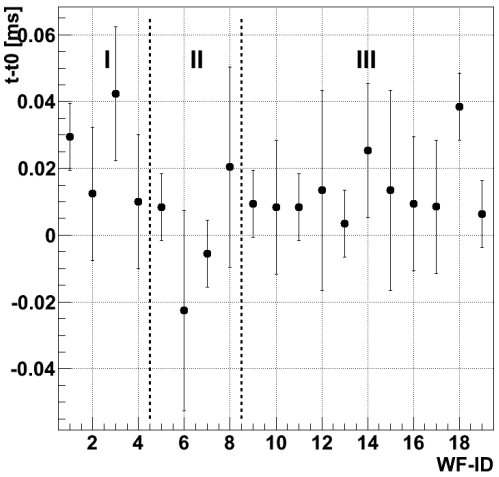

FIGURE 7.16: Difference between the arrival times t derived automatically with the threshold method and the real arrival times t_0 as read from the waveforms. Region I contains the perpendicularly recorded waveforms, region II the parallel ones and region III the ones recorded at random directions.

Cross correlation

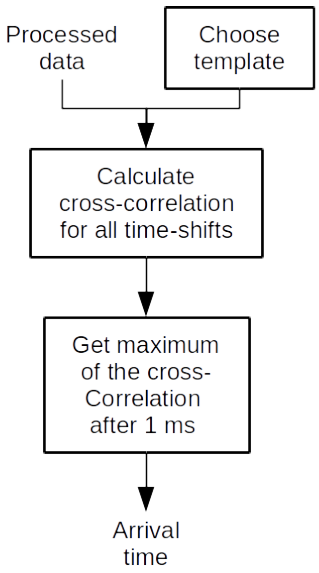

FIGURE 7.17: Steps of the cross correlation method for the determination of the arrival time.

This method is trying to match a template of an expected signal signature to the waveform instead of detecting the beginning of the signal. For this purpose the cross correlation $C(\tau)$ between the signal $S(t)$ and a template $T(t)$ is calculated for all time shifts τ between template and signal.

$$C(\tau) := \int_{-\infty}^{\infty} S^*(t)T(t+\tau)dt \tag{7.1}$$

In our case the signal consists of discrete data points instead of a continuous function. Therefor equation 7.1 has to be transformed into equation 7.2, where S^* is the complex conjugate of the signal.

$$C(j) = \sum_{i=0}^{N} S_i^* T_{i+j} \tag{7.2}$$

Once the cross correlation has been calculated, the arrival time of the signal is known from its maximum absolute value. Due to the aforementioned electromagnetic noise at the beginning of some data sets, again only the maximum after the first 1 ms is considered. The main challenge for this method is to find a suitable template that fits all data sets.
For the template two different approaches were considered. The first one was to use the beginning of a "good" pulse typically from a short distance like ~ 10 m, for example like the one shown in Figure 7.14. The second option is to use simply a sine function of the given frequency that is send to the transducers. In both cases the rest of the template is set to be zero. Examples for both template options can be seen in Figure 7.18.

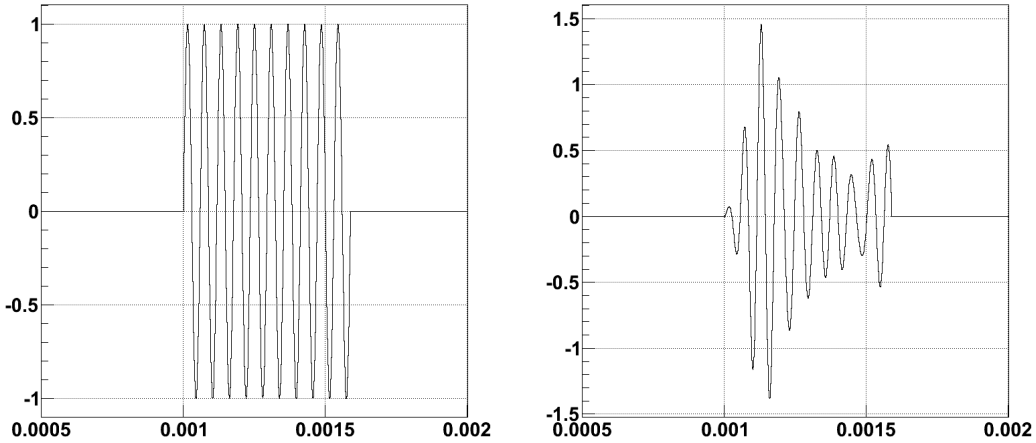

FIGURE 7.18: Examples of the different template options for the cross correlation method. On the left the non-zero part of a template consisting of 10 oscillations of a sine wave with a frequency of 17 kHz is shown and on the right a template made of the 10 oscillations long beginning of a waveform recorded at a distance of ~ 10 m perpendicular to the flow direction of the glacier.

The outcome of the calculation of the cross correlation can be seen in Figure 7.19. The comparison of the signal and the cross correlation shows, that the maximum value of the cross correlation corresponds to the beginning of the processed signal.
Since the shape of the signal is strongly influenced by reflections the length of the non-zero part of the template needs to be optimized. In order to find that optimal length the cross correlation between the template and two data samples was calculated for a varying length of the non-zero part of the template given in number of oscillation periods. One of the data samples was from a short distance of ~ 10 m and the other from a larger distance of ~ 35 m. The resulting arrival times are shown in Figure 7.20.
When looking at the left plot shown in Figure 7.20 the first thing that stands out is the very different behavior of the sine template compared to the two templates based

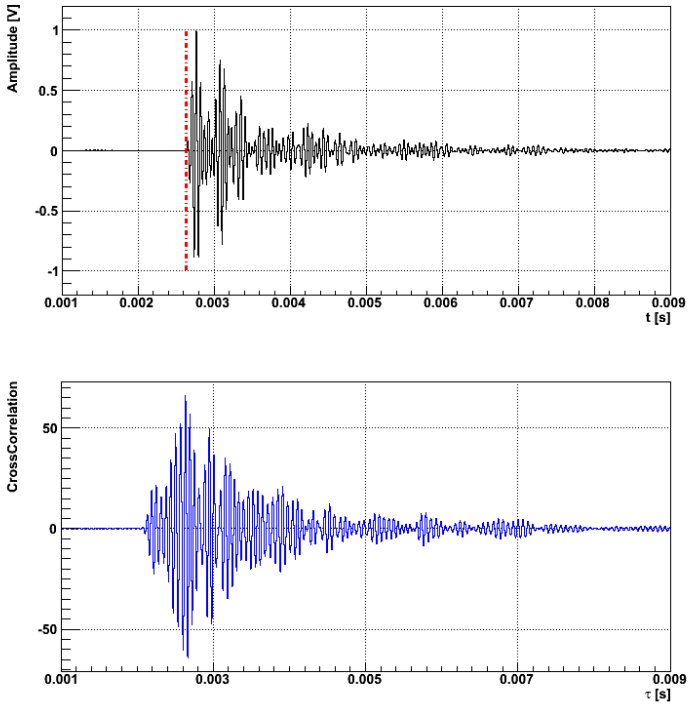

FIGURE 7.19: Example for the determination of the arrival time with the cross correlation method on waveform 1 from table 7.3. The upper plot shows the relevant region of the processed signal. The lower plot shows the cross correlation between that signal and the template from the perpendicular data set at all time shifts. The red line indicates the maximum value of the cross correlation.

on "good" waveforms. While the templates based on data deliver almost the same result and are already stable at a length of only 3-4 oscillation periods the sine template shows large variations and does not stabilize in the considered range. Instead the arrival time shows several linear decreases well below the "true" arrival time before jumping back up to more accurate values. When looking at larger distances (right plot) the sine template first seems to stabilize after 9 oscillation periods but then drifts down after the 14th oscillation period. The other two templates show again a stable behavior at a certain length of the template. In case of the larger distance this is achieved between 5 and 10 oscillation periods. However the results from both templates do not coincide in this case. Possible reasons are the different directions of the propagation of the signals and the usage of different holes for the coupling to the ice. The analyzed waveform was recorded during field test 1.0 between holes 8 and 9 at a distance of about 35 m, which means the propagation was approximately perpendicular to the flow direction of the glacier. The waveforms for the templates were recorded during the same field test between holes 6 and 1 for the perpendicular template and between holes 8 and 7 for the parallel one, both at a distance of about 10 m. Since the result of the template from the same direction is closer to the "true" arrival time than the one from the same hole, the direction seems to be the dominant influence.

For further investigation of the accuracy of this method 19 handpicked waveforms from field test 1.0 have been analyzed. A list of these waveforms and their parameters can be found in table 7.3. The arrival times t_0 given in that table are the ones read directly

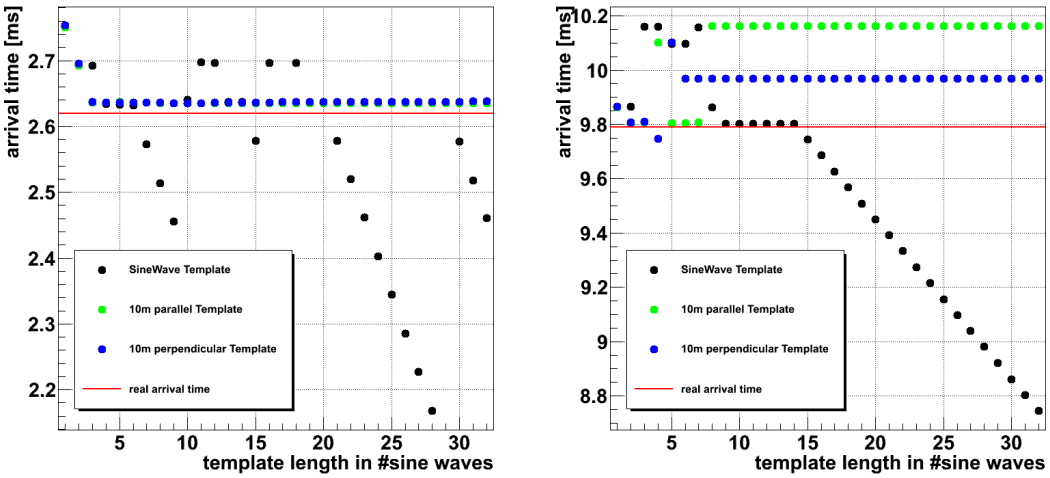

FIGURE 7.20: Comparison of the automatically determined values of the arrival time t with the "real" values (red line) read manually from the waveforms for different length of the non-zero part of the templates. The data for the plot on the left was taken during field test 1.0 between the holes 1 and 6 (10 m) and the one for the right plot between holes 8 and 9 (35 m).

of the waveforms and the speed of sounds are calculated from this arrival time and the distances determined per GPS during field test 1.0. Waveforms 1, 3 and 5 are the ones used also for the optimization of the template length.

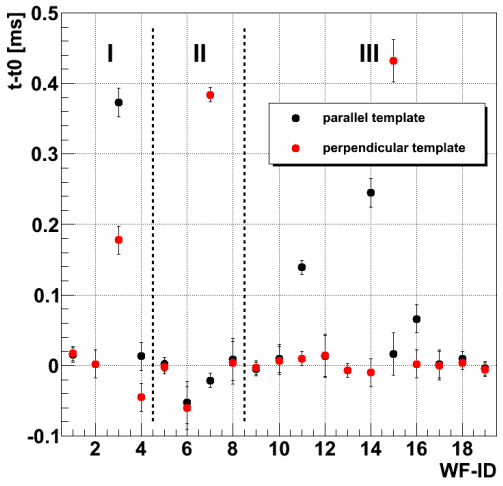

FIGURE 7.21: Difference between the arrival times t derived automatically with the cross correlation method and the real arrival times t_0 as read from the waveforms. Region I contains the perpendicularly recorded waveforms, region II the parallel ones and region III the ones recorded at random directions.

In order to be able to get an impression of how important the choice of the waveform for the template is, the cross correlation for all of these handpicked waveforms was calculated for two different templates both with a length of 15 oscillation periods. Both waveforms

TABLE 7.3: List of datasets used to test the cross correlation method.

Waveform ID	direction	d[m]	t_0[ms]	v_S[m/s]
1	perpendicular	9.90	2.62 ± 0.01	3780 ± 14
2	perpendicular	18.89	5.11 ± 0.02	3697 ± 14
3	perpendicular	35.79	9.79 ± 0.02	3656 ± 7
4	perpendicular	45.04	12.14 ± 0.02	3710 ± 6
5	parallel	9.95	2.70 ± 0.01	3685 ± 14
6	parallel	15.72	4.31 ± 0.03	3648 ± 25
7	parallel	17.67	4.81 ± 0.01	3672 ± 8
8	parallel	23.89	5.86 ± 0.03	4076 ± 21
9	random	9.67	2.64 ± 0.01	3664 ± 14
10	random	21.74	5.89 ± 0.02	3691 ± 13
11	random	9.17	2.52 ± 0.01	3640 ± 14
12	random	20.42	5.58 ± 0.03	3658 ± 20
13	random	11.96	3.28 ± 0.01	3646 ± 11
14	random	11.92	3.23 ± 0.02	3689 ± 23
15	random	16.89	4.63 ± 0.03	3648 ± 24
16	random	14.57	3.95 ± 0.02	3688 ± 19
17	random	8.53	2.39 ± 0.02	3571 ± 30
18	random	15.72	4.25 ± 0.01	3700 ± 9
19	random	11.94	3.24 ± 0.01	3686 ± 11

were from a distance of ~ 10 m. The first one was propagating parallel to the flow direction of the glacier and the second one perpendicular to that direction.
As can be seen in Figure 7.21 the automatically determined arrival times differ from the real values up to 400 µs. Also both templates do not deliver the same result in all cases and this discrepancy can be as large as the deviation from the real arrival time. The uncertainty of this method, defined as the average of the absolute value of the deviation, is 45.86 µs for the parallel template and 56.49 µs for the perpendicular template.

Hilbert envelope

This method is again focusing on the start of the signal. The idea is to isolate the slowly varying envelope from the fast oscillations of the signal and by doing so reducing the methods susceptibility to disturbances of the signal start. The envelope used in this work is the Hilbert envelope, which is given as the absolute value of the analytical signal of the original signal. The steps for calculating the analytical signal and the envelope are described below. An overview of the separate steps for the entire method is shown in Figure 7.22.
The first step is to calculate the Hilbert envelope of the signal. To do this it is necessary to calculate the analytical signal $S_a(t)$ given by equation 7.3.

$$S_a(t) = s(t) + i\tilde{s}(t) \tag{7.3}$$

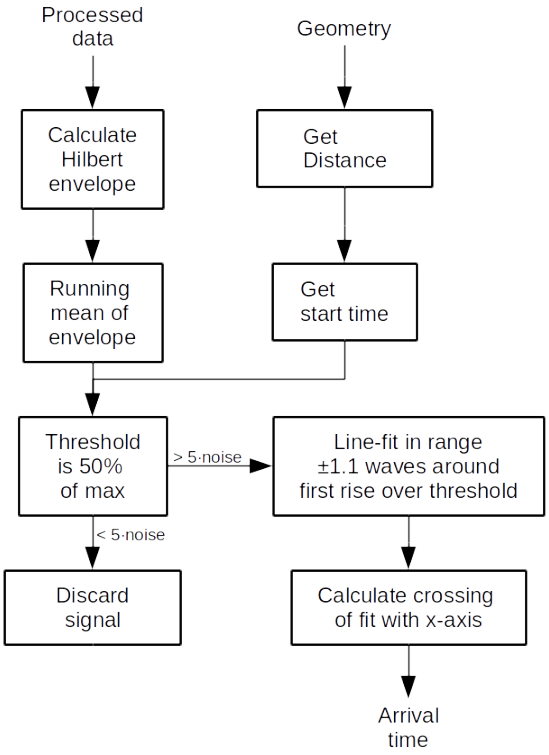

FIGURE 7.22: Steps of the Hilbert method for the determination of the arrival time.

where $s(t)$ is the real signal given by the measured time series and $\tilde{s}(t)$ is its Hilbert transform [54]. The Hilbert transform is defined as:

$$\tilde{s}(t) = \frac{1}{\pi} \int_{-\infty}^{\infty} \frac{s(\tau)}{\tau - t} d\tau \tag{7.4}$$

Since equation 7.4 is not practical if the real signal $s(t)$ is given by a discrete series of real numbers the relationship with the Fourier transform $\mathcal{F}$ given by equation 7.5 is used.

$$\mathcal{F}(\tilde{s})(\omega) = -i \operatorname{sgn}(\omega) \mathcal{F}(s)(\omega) \tag{7.5}$$

The function sgn(ω) is -1 if ω is negative, 0 if ω is zero and +1 if ω is positive. By using Euler's formula $\exp(ix) = \cos(x) + i \sin(x)$ equation 7.5 can be written as

$$\mathcal{F}(\tilde{s})(\omega) = \begin{cases} e^{+i\frac{\pi}{2}} \cdot \mathcal{F}(s)(\omega) & , \omega < 0 \\ 0 & , \omega = 0 \\ e^{-i\frac{\pi}{2}} \cdot \mathcal{F}(s)(\omega) & , \omega > 0 \end{cases} \tag{7.6}$$

This means that the Fourier transform of the Hilbert transform can be obtained from the Fourier transform of the real signal by shifting the phase by $+\pi/2$ for the negative frequency components and by $-\pi/2$ for the positive frequency components [55]. After all shifts are applied the Fourier transform is used backwards to obtain the normal Hilbert transform that is needed for the analytical signal in equation 7.3.
The envelope is then calculated as the absolute value of the analytical signal by equation

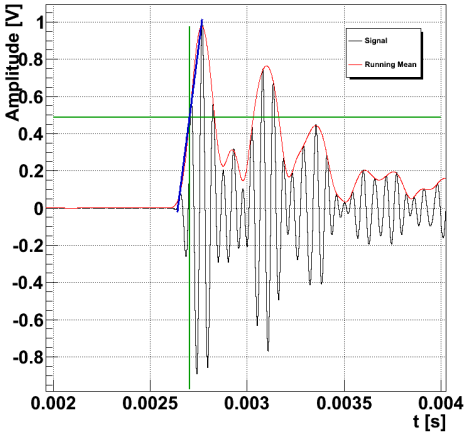

FIGURE 7.23: Example for the determination of the arrival time with the Hilbert method on a waveform from FT-1 at a distance of ~ 10 m.

7.7.

$$|S_a(t)| = \sqrt{s(t)^2 + \tilde{s}(t)^2} \tag{7.7}$$

The next step is to calculate the running mean with a window of 20 bins of that envelope in order to further suppress disturbances from the environment. Instead of just looking at the first rise over a threshold here a linear fit can be used. The range for this fit is determined by the signals first rise over 50% of the maximum amplitude of the envelope and picking a suitable interval around this time. The optimization of this interval can be seen in Figure 7.24. After the linear fit has been done the point where it becomes zero gives the determined arrival time t of the signal.
For the optimization of the fit range the arrival time was determined for all 19 test data sets from table 7.3 with a varying range from 0.1 to 2 periods every 0.1 periods. For each waveform the range with the result closest to the real arrival time was stored (see right plot in Figure 7.24). The average value of these ranges is calculated to be 1.09 ± 0.42 and therefor 1.1 periods of the sent signal is used as the default fit-range in this method.
In summary calculating the threshold as the percentage of the maximum works well for clear signals and calculating the threshold as a multiple of the noise only works for noisy signals. In order to distinguish between both in all cases first the threshold is calculated as 5% of the maximum. Then this value is compared with 5 times the width of the noise and if the current threshold is lower than 5 times the noise it is replaced by it. The last step is to determine the first rise over the threshold after the start time. That start time is again calculated from the distance of the transducers and the clearly too high value for the speed of sound of 4500 m/s.
This method has been applied to all test-datasets from table 7.3 and the result is shown in Figure 7.25. The differences between true arrival time t_0 and the time t from the Hilbert-method is below 0.035 ms for all datasets. The uncertainty on the automatically determined arrival time here is 8.96 µs.

Comparison

Of the three tested methods for the automated determination of the arrival time the cross-correlation method delivers the least accurate results. With an uncertainty of about 50 µs this method can not compete with the other two options. Although the

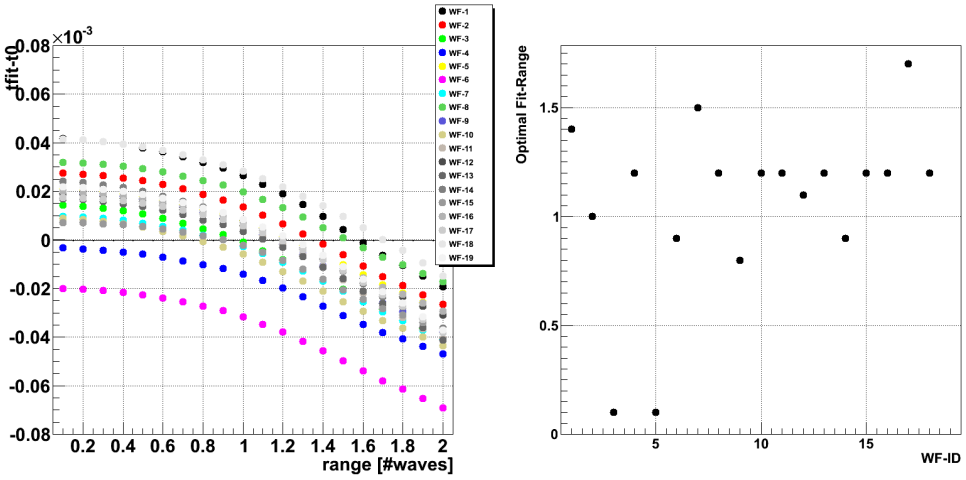

FIGURE 7.24: Optimization of the fit-range for all test-datasets for the Hilbert method. Left: Difference between the automatically determined arrival time t and the true arrival time t_0 for different fit-ranges. Right: Optimal fit-range for each test-dataset. The average of these values gives the optimal fit-range for this method.

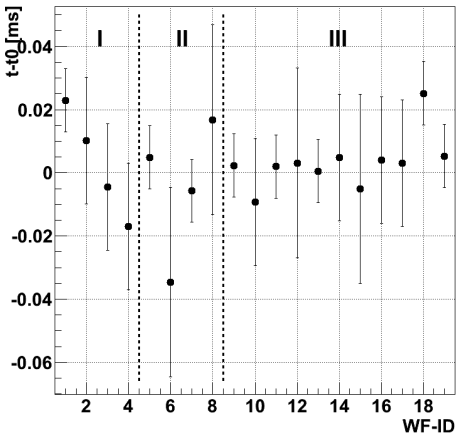

FIGURE 7.25: Difference between the arrival times t derived automatically with the Hilbert method and the real arrival times t_0 as read from the waveforms. Region I contains the perpendicularly recorded waveforms, region II the parallel ones and region III the ones recorded at random directions.

uncertainties of the threshold method and the Hilbert method are similar the uncertainty of the Hilbert method is better by a factor of 1.66 and is therefor used for the analysis of all in-ice measurements.

7.3.2 Results

Directional dependency

For the analysis of the directional dependency of the speed of sound the data from field tests 1.0, 2.5 and 3.0 is used. During field test 0.0 the absolute 3 dimensional positions of the holes remain unknown, disqualifying these measurements for this analysis and during

field test 2.0 the coupling of most transducers was not sufficient to record acoustic signals, making a directional analysis impossible.

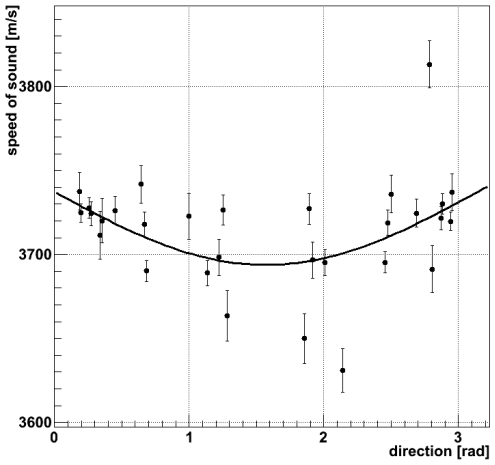

FIGURE 7.26: Speed of sound in dependence of the direction on the glacier for the array measurement during field test 1.0 including a sine fit.

During field test 1.0 the best data for a directional analysis was taken within the transducer array (holes 1-6) that was installed for the positioning of the ice mole. These holes had a similar depth between 0.45 m and 0.97 m and were uniformly distributed. The result of these measurements is shown in Figure 7.26. This is the only field test were a weak directional variation of the speed of sound was observed. The χ^2/ndf for the sine fit shown in the plot is 5.72, while the χ^2/ndf for a flat line is 8.49. Both values are too high to be evidence for a suitable model. The reason for this is, that the error bars reflect only the influence of the determination of the speed of sound and the measurement of the positions of the probe. Hence systematic errors, e.g. due to coupling, remain unaccounted for, making the calculation of a likelihood unrealistic. Nevertheless, due to its smaller χ^2/ndf value, the sine fit seems to describe the data better. The reduction of the speed of sound according to that fit is about 5% at 1.57 ± 0.04 rad, which corresponds to the flow direction of the glacier at the test site.
Figure 7.27 shows the speed of sound for all recorded waveforms in dependency of the direction. The two clusters are caused by the geometry of the holes that was focused on only two main directions (parallel and perpendicular to the flow direction). Here the absolute spread of most data points is 7%. The two outliers towards higher speed of sound can be explained by the presence of stones next to holes and the ones towards lower speed of sound by the presence of snow directly in front of the holes. The comparison of the two clusters shows no significant difference between them both, meaning that on this test site no directional dependency of the speed of sound was observed.
Although there were six transducers deployed during field test 3.0 only data from 5 of them was usable. Transducer 3 was located on the other side of the crevasse and was therefor acoustically cut off from the other transducers. In addition the coupling of transducer 2 was not sufficient to receive signals or send them properly. The only clear signals from transducer 2 were observed by transducers 4 and 5. Transducer 6 was too close to distinguish between the electromagnetic cross talk and the acoustic signals recorded by transducers 1 and 5 were not clear enough for a reliable determination of the

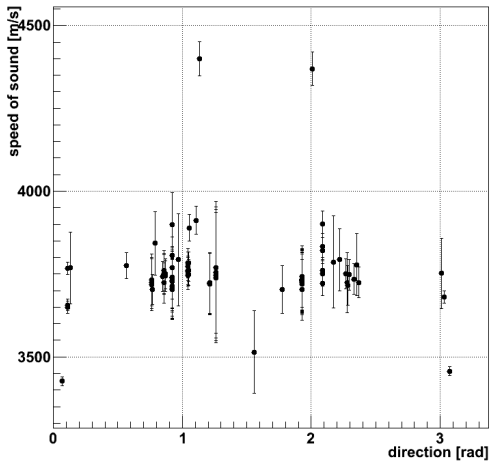

FIGURE 7.27: Speed of sound in dependence of the direction for all data samples from field test 2.5.

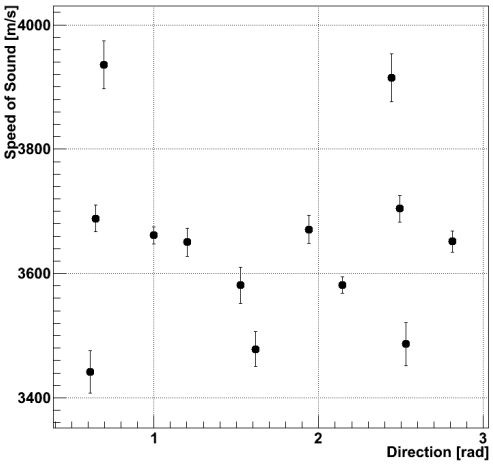

FIGURE 7.28: Speed of sound in dependence of the direction for 18 kHz and an sending voltage of 5 V from field test 3.0.

speed of sound. The result for the rest of the combinations and a frequency of 18 kHz in shown in Figure 7.28. Here the absolute spread is 15% , which is the biggest spread observed during all field tests. However here again no directional variation could be recognized.

Depth dependency

Since glaciers grow by snow falling on them that is compressed by pressure over time, it is plausible, that the speed of sound can vary with depth in the ice. The first depth dependent measurements have been performed at field test 0.0 on the Morteratsch glacier. During this field test a total of 7 holes was drilled. Five with a depth of 2 m and two with a depth of 5 m. Unfortunately during this first field test instead of measuring the 3D-coordinates of each hole only the distances between some of the holes were measured (see Figure5.2). As can be seen in Figure 7.29 for the determination of the real distance

between the emitter and the receiver also the difference in height of the two holes is needed. Since this was not determined during the field test it is not possible to determine the real speed of sound from any data obtained during this test campaign. However if one assumes, that the difference in height h is zero one can still qualitatively determine how the speed of sound changes with depth or frequency.

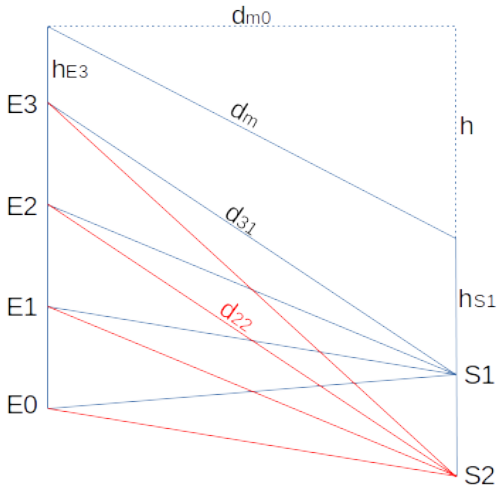

FIGURE 7.29: Determination of the distance between the emitter position E_i and the different receivers R_i.

The second thing that needs to be considered is, that neither emitter nor receiver had direct contact to the ice. The coupling was done by inserting both in water filled holes with a diameter of roughly 15 cm, which means that the acoustic signals have to pass through an unknown amount of water before they reach the intersection between water and ice. Due to the lower speed of sound of water this leads to an underestimation of the speed of sound. As can be seen in Figure 7.30 this effect is especially significant at short distances.
In section 6.3 was calculated that this effect can change the signal propagation time for a single hole by ~ 0.0673 ms, based on the geometry of the hole and assuming emitter and receiver are placed at the same depth. Since there are always two holes involved in a single transmission, changes of 0.1346 ms of the signal propagation time are realistic. When assuming, that the real speed of sound in ice is about 3500 m/s over a distance of 5 m this time difference leads to an underestimation of the speed of sound of 301 m/s. At 10 m the reduction of the speed of sound is only 157 m/s and at 20 m the difference is only 81 m/s.
As explained below, the spread of the data points at a given distance can be explained by the same effect.
The influence of the water in the holes is even bigger when emitter and receiver are located at different depth. Depending on the insertion depths, the angle in which the pulse strikes the intersection between ice and water changes and with that also the amount of water that has to be crossed. For an angle of 60° the change of the signal propagation time is 0.0778 ms, leading to an effect that is expected to be 15 % higher than the one for transducers at the same depth. Since the speed of sound in water is significantly lower than in ice, the signals arrive later if more water has to be crossed, leading to an even bigger underestimation of the speed of sound for big differences in insertion depth of emitter and receiver.

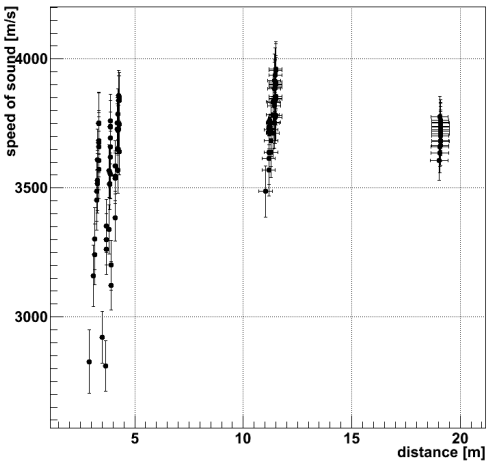

FIGURE 7.30: Speed of sound depending on the distance during FT-0.0 at 30 kHz.

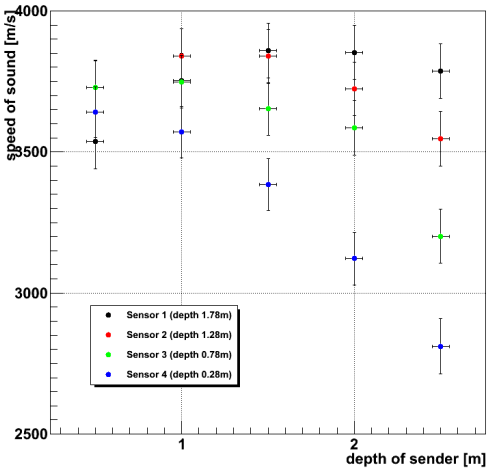

FIGURE 7.31: Speed of sound for different insertion depth of the emitter in hole 1 for fixed insertion depth of the 4 receivers in hole 0 during FT-0.0 at a frequency of 30 kHz.

This behavior can be seen in Figure 7.31, where the speed of sound is shown for a fixed pair of holes from field test 0.0. The emitter was inserted in hole 1 at different depth while the four receivers were inserted in hole 0 at fixed depths. Receiver 4 was closest to the surface at a depth of 0.28 m, the next receiver was 0.5 m deeper and so on. For each receiver the maximum speed of sound was measured when the emitter was closest to their own depth and the differences between the receivers are largest when the emitter is deeper than all of them at a depth of 2.5 m.
As can be seen also in Figure 7.32 this effect has a smaller impact when the distance between the two holes is increased. The distance between hole 1 and 0 was only 4.28 m while the distance between 2 and 0 was 11.50 m and between 5 and 0 even 19.10 m.
For this reason for the determination of the speed of sound only data points that were recorded with emitter and receiver at the same insertion depth were used. For field test

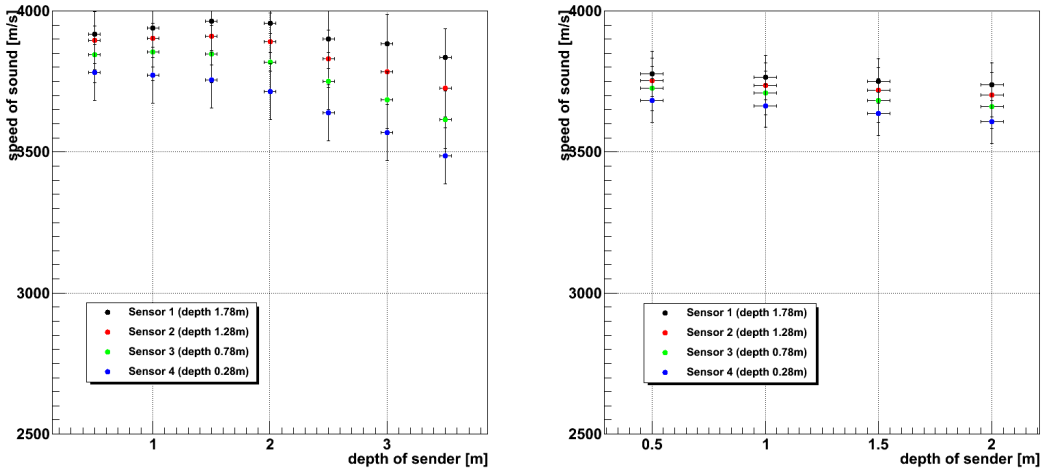

FIGURE 7.32: Speed of sound for different insertion depth of the emitter in hole 2 (left) or hole 5 (right) for fixed insertion depth of the 4 receivers in hole 0 during field test 0.0 at a frequency of 30 kHz.

0.0 and 1.0 suitable measurements were performed. The result for field test 0.0 can be seen in Figure 7.33 and the one for field test 1.0 in Figure 7.34.

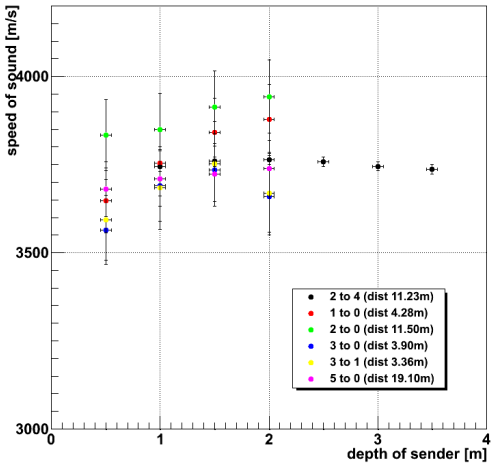

FIGURE 7.33: Speed of sound versus the transducer depth for field test 0.0 at 30 kHz.

During field test 0.0 there were suitable measurements from 6 different combinations. The signals that were recorded between holes 6 and 0 were too week and could not be detected in the data files. Already at depths of up to 6 m the speed of sound shows variations of up to 250 m/s and is bigger for shorter distances (holes 1 to 0, 3 to 0 and 3 to 1). The dependency of the distances most likely is again caused by the impact of the uncertainty due to the unknown amount of water the acoustic waves have to cross before they enter the ice. When looking at larger distances only a variation of ~ 100 m/s can be observed.
During field test 1.0 there were measurements from three different hole combinations of hole 7, 8 and 9 up to a depth of 7 m. The other holes were not deep enough. The

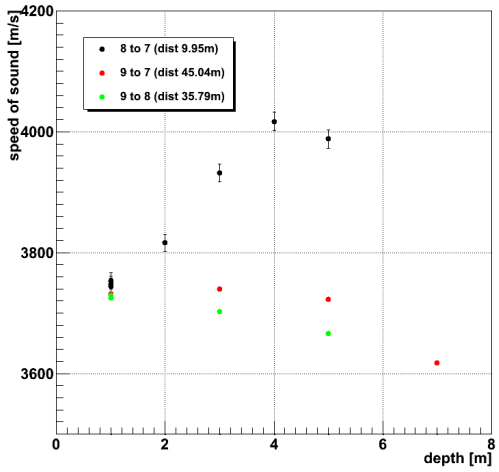

FIGURE 7.34: Speed of sound versus the transducer depth for field test 1.0.

highest variation here was with a value of ~ 350 m/s bigger compared to the previous filed test. However this was only observed for signals between hole 8 and 7 and the absolute variation of the other combinations was similar to larger distances from field test 0.0 again ~ 100 m/s. One explanation for the different behavior of signals between 8 and 7 could be the unknown shape of the hole. When looking at the map one can see, that the direction for this combination is different than the other two directions. So if one of the holes is not as vertical as assumed in the analysis but tilted in one direction this would lead to an miscalculation of the true distance in one direction and therefor cause a different height profile of the speed of sound.
In summary we can only say, that there seems to be a correlation between the speed of sound and the depth in the glacier that causes variations of up to 350 m/s. In order to estimate how much of this is caused by the structure of the ice and not by the geometry of the holes more information on the shape of each hole and the positions of the transducers in the holes would be needed.

Temperature dependency

TABLE 7.4: Average speed of sound for all field tests.

Field test	Speed of sound	Ice
0.0	3730 ± 60 m/s	temperate
1.0	3661 ± 26 m/s	temperate
2.0	3519 ± 3 m/s	cold
2.5	3677 ± 165 m/s	temperate
3.0	3589 ± 163 m/s	cold

Table 7.4 summarizes the average speed of sound for all field tests. The uncertainties given are the RMS of the respective distributions. A high variety of the error on the speed of sound is observed. Especially for field test 2.0 the spread is quiet small. During

this field test only two valid data points were recorded and they did not differ much from each other, leading to the unplausible small error on the average speed of sound. An explanation for the bigger variance for field test 2.5 and 3.0 could be, that the averaged data for these field tests covered a larger range of frequencies and was recorded with a higher geometric variance of the hole combinatins.
However the most important observation here is, that systematically the speed of sound on alpine temperate glaciers was about 100 m/s higher than on glaciers in Antarctica. Whether this is due to the higher temperature or caused by the presence of water in the ice on temperate glaciers remains unclear.

Frequency dependency

Systematic frequency dependent measurements have been performed only during field test 2.5 and 3.0.
During field test 2.5 only data at four different frequencies was usable (5.0 kHz, 7.5 kHz, 10.0 kHz and 18.0 kHz). The average speed of sound for all data recorded at each frequency is summarized in table 7.5.

TABLE 7.5: Average speed of sound in dependency of the frequency for field test 2.5.

f [kHz]	Speed of sound [m/s]
5.0	3653.06 ± 179.30
7.5	3774.57 ± 38.71
10.0	3766.50 ± 31.92
18.0	3748.71 ± 17.72

The first thing that catches the eye is, that the uncertainty for the speed of sound at 5 kHz is much larger than for the other frequencies. The reason for this is, that at 5 kHz a lot of the waveforms were recorded at very shallow depths of below 29 cm. At these depths the sound waves have to cross through a layer of fluffy snow, which reduces the speed of sound. The combination with data taken deeper in the ice leads then to larger fluctuations of the speed of sound. When looking only at the data points with depths greater than 29 cm the average speed of sound is 3786.23 ± 52.43 m/s. As one can see the uncertainty is then in the same order of magnitude as for the other frequencies and also the value itself is a little higher than before.
The other thing that can be observed is, that the speed of sound shows a small reduction towards higher frequencies. When using a linear fit on the data in table 7.5 a reduction of only -2.55 ± 2.84 m/s is observed. Although this reduction is consistent for all frequencies, if the firn data at 5 kHz is excluded, it is to small to be significant. This can also be seen from the χ^2/NDF for this fit, which is 0.01. The uncertainties of all measured velocities are to big for a reliable statement about the frequency dependency, so all measured velocities still agree with each other within their uncertainties.
As already described in section 7.3.2, during field test 3.0 usable waveforms were not available for every combination of holes. When looking at the result for all valid combinations shown in Figure 7.35, one can immediately see that there are large fluctuations of the speed of sound of several hundred m/s for some of the combinations (1 and 6, 2 to 6, 5 and 6). To check the consistency of the data the signals emitted between two holes in opposite directions can be compared. For all possible combinations shape and

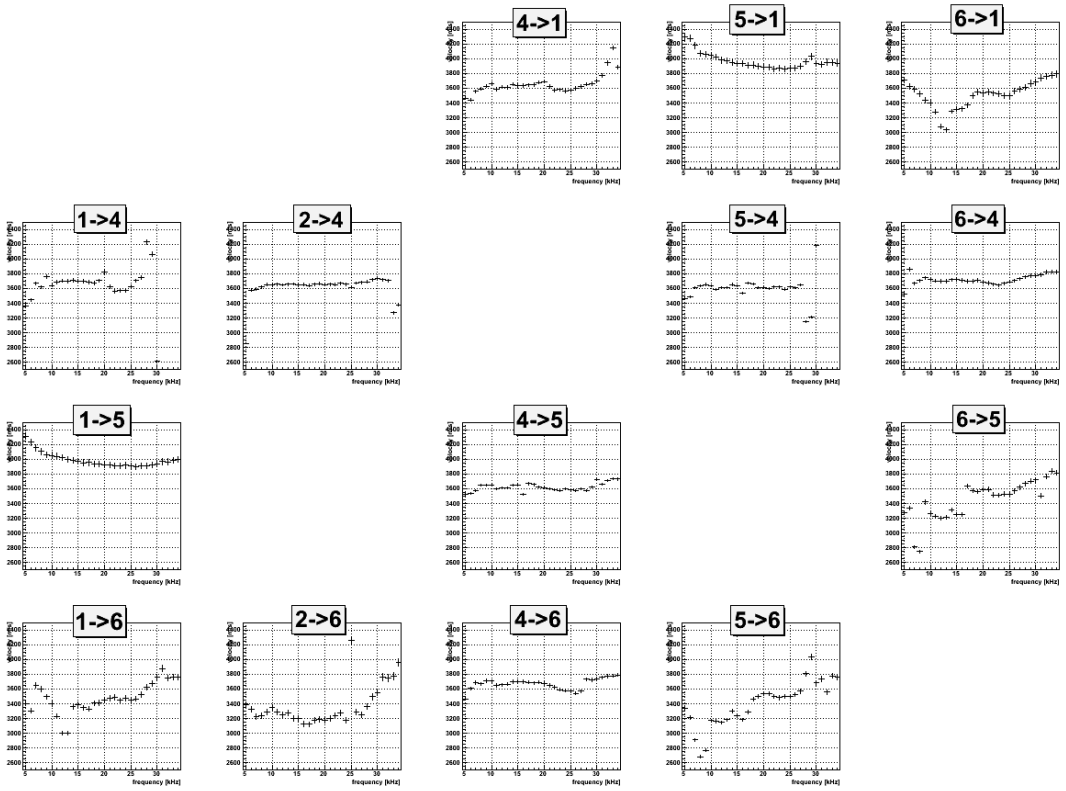

FIGURE 7.35: Speed of sound versus frequency for all valid (see section 7.3.2) combinations during field test 3.0. The x- and y-axis is the same for all plots.

magnitude of the fluctuations are similar up to 25 kHz, where the fluctuations tend to get even bigger. The reason for the rising fluctuations is the reduced quality of the signals at higher frequencies that can lead to a faulty determination of the speed of sound. There are two reasons for this reduction of the signal quality. The first one is, that the amplitudes of the emitted signals is lower for higher frequencies and the second reason is due to the attenuation in ice, which is increasing for higher frequencies.
When comparing all patterns up to 25 kHz no global pattern can be observed. In Figure 7.36 the speed of sound is shown for all frequencies up to 25 kHz in dependence of the distance and in dependence of the propagation direction. In case of the direction again no pattern can be observed. In case of the distance one can see, that the largest spreads are present at small distances, which is a hint, that the coupling has a high influence here.
In summary we can only say, that there is a high chance, that the frequency has an impact on the measured speed of sound, but this influence is dominated by the specific configuration of the transducers in the ice (coupling, maybe obstacles) and not globally by the ice quality of the test site.

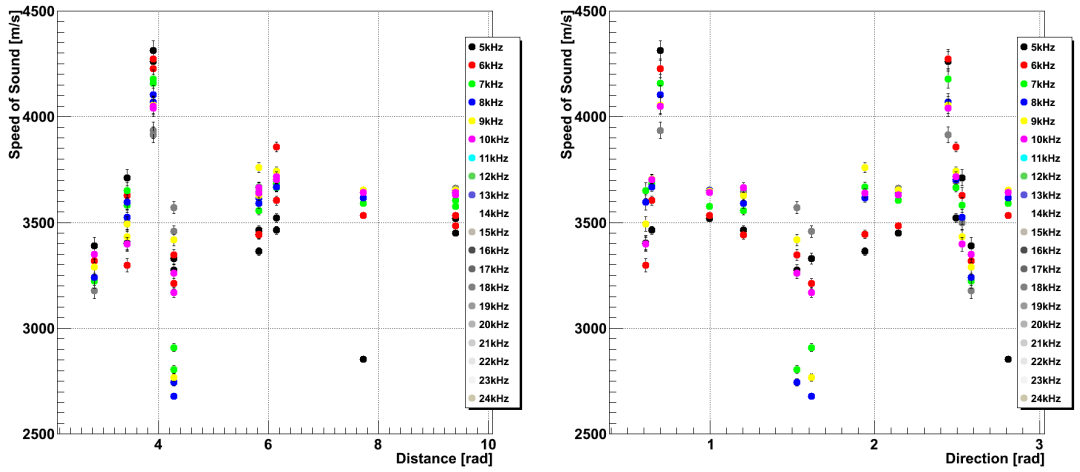

FIGURE 7.36: Speed of sound for frequencies 5 – 24 kHz against distance (left) and direction (right) during field test 3.0.

7.4 Attenuation

The attenuation of acoustic signals in ice is one of the limiting factors for the range of the system. Therefore the determination of the attenuation length was one of the goals during the field tests.

7.4.1 Methods for estimation of the energy content

A reliable method for the estimation of the energy content of an acoustic signal is needed. To find one, four different approaches were pursued and tested. The first was to take the measured amplitude of the signal, the second to consider the area underneath the curve, the third to use the signal to noise ratio and the last one to calculate the width of the signal. To estimate how stable each method is, the respective parameter is calculated for several waveforms from a similar configuration, meaning similar distance, similar coupling, same frequency and same sending amplitude. The method with the lowest fluctuation of its parameter for these waveforms is considered the most stable. A list of the used waveforms including the respective configurations can be found in Table 7.6. All datasets were recorded during field test 1.0 with a frequency of 17 kHz, an amplitude of 75 V and coupling to the ice via water filled holes.

Amplitude

As illustrated in Figure 7.37 this method simply calculates the difference between the maximum and minimum amplitude of the waveform and uses half of this as a measure for the energy content of the signal. The main drawback of this method is its susceptibility for disturbances by superpositions caused by reflections at the surface of the glacier or other obstacles in the ice.
When looking at the datasets from Table 7.6 a relative spread of 21.08% is found for the amplitudes.

TABLE 7.6: Datasets used for stability estimations of attenuation methods.

ID	Distance [m]	Depth emitter [m]	Depth receiver [m]
1	9.95	1.00	1.00
2	9.95	1.00	1.00
3	9.90	0.85	0.80
4	9.17	0.68	0.97
5	9.67	0.97	0.80
6	9.17	0.97	0.68
7	9.90	0.80	0.85

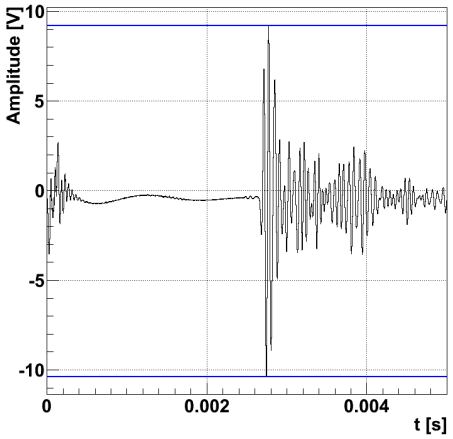

FIGURE 7.37: Waveform from field test 1.0 with maximum and minimum values illustrated by the blue lines for the amplitude method.

Area beneath the curve

The second attempt was to look at the area beneath the signal. For this a signal region is defined. The start of the signal is given by the arrival time derived from the Hilbert method. Since even the envelope of the signal shows large oscillations the end can not simply be defined by a drop beneath a certain threshold and is instead defined by the arrival time of the signal plus the duration of the sending sequence. For field test 1.0 this length about 1.2 ms since 20 oscillations were send at a frequency of 17 kHz (see Figure 7.38). The area beneath the curve in that region is then estimated by adding up all recorded values in that region.
The relative spread for all the datasets from Table 7.6 for this method is 20.98%. This is very similar to the result obtained from the amplitude method, probably because this method is also very sensible to the disturbance by reflections.

Signal to noise ratio

As indicated by the name signal to noise ratio (SNR) this method needs to calculate the signal strength and the noise. In order to do so a noise and a signal region are defined. The signal region is the same as used for the area method and the noise region is the same as described in the Threshold method (Section 7.3.1), which is used also in

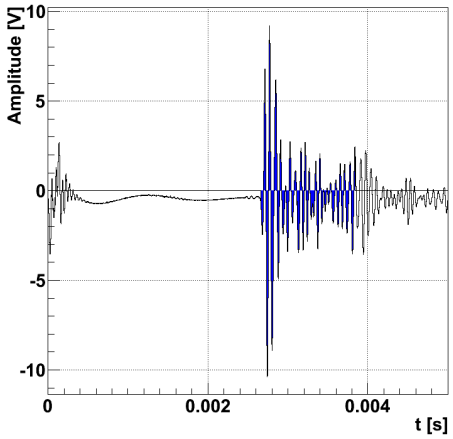

FIGURE 7.38: Waveform from field test 1.0 with the area beneath the curve illustrated in blue for the area method.

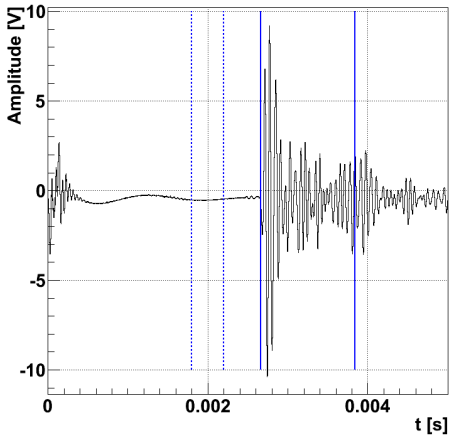

FIGURE 7.39: Waveform from field test 1.0 with noise and signal regions for the SNR method. The noise region is illustrated by the dashed lines and the signal region by the solid lines.

the Hilbert method (Section 7.3.1). Both regions are shown for an example waveform in Figure 7.39. The signal strengths for both regions are then calculated as the width, defined by the RMS, in the respective regions and the SNR is then derived as follows:

$$\mathrm{SNR} = \frac{RMS_{signal}}{RMS_{noise}} \tag{7.8}$$

Here the relative spread turns out to be 35.97%. This value reflects the impact of the noise. Depending on the time and exact location the noise can vary a lot and therefore explains, why the SNR is not well suited to estimate the signal strength at this point.

Width of the signal

The last attempt was to look only at the signal region. The definition of this region remains unchanged and the signal strength is again calculated from the width, given by the RMS of the waveform in that region.

For this method the relative spread for all datasets in Table 7.6 is 18.75%. Although this value is still quiet high this is the best measure of the signal strength that could be found and is therefore used for all determinations of the attenuation length. This can also be seen in Figure 7.40, where the relative deviation of all datasets for all methods is shown. As expected for the most stable method the points of the width method are in average closest to 1.

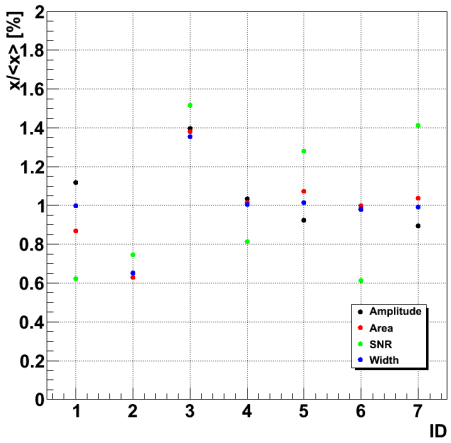

FIGURE 7.40: Relative deviation of the datasets from Table 7.6 for all methods for the determination of the signal strength. Depending on the method x can be either amplitude, area, SNR or width.

7.4.2 Results

Frequency dependency

For the determination of the attenuation length λ only measurements from field test 1.0 and 2.5 were usable. The data from field test 0.0 was not suitable because an exact measurement of the positions of the transducers is missing. During field test 2.0 only two of the recorded waveforms were usable, which is not sufficient for a measurement of the attenuation length, which leaves field test 3.0. During this field test the coupling was done by freezing the transducers to the ice, which leads to a not very well defined coupling between the transducer and the ice (see Section 6.3).
Even when the coupling is realized through water filled holes, as done during field test 1.0 and 2.5, it is still a huge source of uncertainty for the signal strength. In order to estimate this and other influences the variance of the spread of the widths for all waveforms within a certain distance is calculated. From this the relative uncertainty of the width at that distance is obtained. This relative uncertainty is assumed to be independent from the distance. So then it can be used to calculate the absolute uncertainty for the width of each waveform by multiplying its width with the relative uncertainty.
For field test 1.0 the range between 15 and 25 m is used leading to a factor of 0.47. For field test 2.5 there were two suitable ranges. The first one between 10 and 20 m, giving a relative uncertainty of 0.26 and the second one between 30 and 45 m, leading to a factor of 0.96. The average of both factors is 0.61, which is the relative uncertainty used for all data points from field test 2.5.

Since the width of the signal is proportional to the sound pressure $p(d)$ we can use equation 4.14 to determine the attenuation length λ given by the inverse of the attenuation coefficient k. Equation 4.14 can be transformed to this equation:

$$\log p(d) * d = \log p_0 - kd \tag{7.9}$$

When we plot $\log \text{width}_{\text{signal}} * d$ against the distance d and do a linear fit of these data points, the attenuation coefficient is therefor given by the gradient of the fit.

TABLE 7.7: Attenuation lengths from the fits.

f [kHz]	k [1/m]	λ [m]	χ^2/NDF
Pers glacier (FT-2.5)			
5.0	0.0320 ± 0.0037	31.3 ± 3.7	4.40
7.5	0.0558 ± 0.0047	17.9 ± 1.5	3.39
10.0	0.0462 ± 0.0048	21.7 ± 2.2	3.45
18.0	0.0688 ± 0.0048	14.5 ± 1.0	3.76
Morteratsch glacier (FT-1.0)			
17.0	0.0682 ± 0.0104	14.7 ± 2.2	3.76

Figure 7.41 shows the results of all suitable datasets. On the left side the comparison between the measurement on the Morteratsch glacier in 2013 and the measurement at 18 kHz on the Pers glacier in 2014 is shown and on the right side the comparison of different frequencies measured only on the Pers glacier. The resulting attenuation lengths are summarized in Table 7.7.

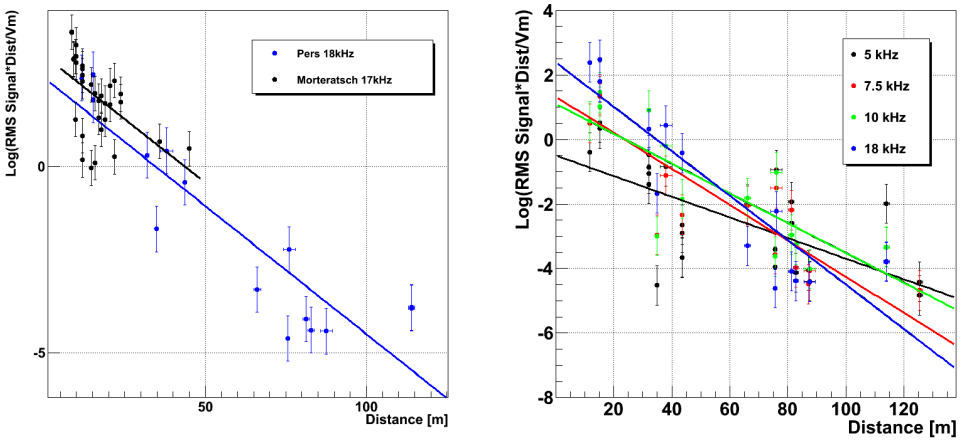

FIGURE 7.41: Left: Comparison of the attenuation on Morteratsch and Pers glacier at a similar frequency. Right: Attenuation for different frequencies on the Pers glacier.

When comparing the result for the attenuation length on the Morteratsch glacier with the value of 11.4 ± 2.2 m [56] obtained on the same test site by the group from the RWTH Aachen, one can easily see, that the values do not agree with each other within their uncertainties. The different results occur due to the usage of amplitudes by the RWTH Aachen instead of the width of the signals and also by the data selection. While

the RWTH Aachen used every single data point measured during the field test, in this work only those combinatins were used where a well defined coupling to the ice could be assumed.
The results for the Morteratsch and the Pers glacier at a similar frequency agree with each other well within their uncertainties. Between the two test sites there were two significant differences. One being that the Pers glacier was still covered in 1 m to 2 m of snow during the test campaign, which may lead to colder and therefor dryer ice. The other is that the test site on the Morteratsch was very close to a giant crevasse in a region where the ice could be more fissured than at the test site on the Pers glacier. Apparently neither of these differences has a big impact on the attenuation length.
When looking at the comparison of the different frequencies there is a clear tendency of more attenuation at higher frequencies. The attenuation length at 18 kHz is only half of the attenuation length at 5 kHz and the values for the intermediate frequencies are, although not in the right order, somewhere in the middle. This means that in order to achieve a higher range of the system smaller frequencies should be used.

Chapter 8

Conclusion

The goal of this thesis was the development of the emitting part of an acoustic positioning system and in addition to study the feasibility of acoustic positioning during a lander mission to the Saturns moon Enceladus.

The system developed for this purpose is based on trilateration and consists of a central transducer unit, that controls the 6 frontend transducer units that are connected the actual transducers. To test the hardware under real life conditions a total of five field tests have been performed.

For the estimation of the influence of possible uncertainty sources, as the accuracy on the positions of the transducers, the uncertainty on propagation time and on the speed of sound, a Monte Carlo simulation has been conducted. The result of this simulation beeing that, in order to achieve an uncertainty on the probes position below 1 m the positions of the transducers have to be known with an accuracy of 5 cm, the propagation time with an accuracy of 5 µs and the speed of sound with an accuracy of 35 m/s. Also the transducers have to be placed from each other at a distance of at least 20 m.

The coupling between the transducers and the ice was identified as one of the key aspects of the system. Two different options were tested. The first one was the coupling through water filled holes and the second one was to let the transducers freeze into the ice. While the coupling through water filled holes has prooven to provide a better defined transition of the acoustic waves into the ice, it also results in larger uncertainties on the measured speed of sound in ice due to the geometry of the holes. When the transducers are frozen in, the measurement of the speed of sound is more accurate, but when the direct contact between the transducer and the ice is interrupted by air, this form of coupling can easily lead to a complete loss of the signal. On Enceladus the temperature on the surface leaves only frozen in transducers as an option, which is even riskier there. Since, in case the direct contact to the ice is lost, the gap would not even be filled with air.

For the determination of the signal propagation time, three methods were developed and compared. The first method was the usage of a threshold based on the maximum amplitude and noise of the each waveform. The second one was to use the cross-correlation between the signals and a template and the third was to use a threshold on the Hilbert envelope of the waveform. This third option has prooven to be the most accurate method with an accuracy of 9.51 µs.
Using this method, directional, depth, temperature and frequency dependencies of the speed of sound in glacial ice were investigated. Most test sites did not show a correlation between the flow direction of the glacier and the speed of sound. Only during field test

1.0 a reduction of 5% in flow direction was observed. The depth dependent measurements have shown a variation of the speed of sound of up to 10%. When comparing the results from test sites on temperate and cold glaciers, on cold glaciers a 3% lower average speed of sound has been measured. For the dependency on the frequency a high variation has been observed. However this variation is depending on the geometry of the setup, rather than beeing a global property of the ice.

Four different attributes of a waveform have been tested for the determination of the attenuation length in ice. The first one was the maximum amplitude of the signal, the second one the area underneath the curve, the third one the SNR and the last one the width of the amplitude distribution of the waveform. The width turned out to be the most stable and was hence used in all attenuation measurements. The measured attenuation lengths vary between 14.5 m and 31.3 m and are depending on the frequency of the emitted pulses. When comparing different test sites for the same frequency the measured attenuation lengths agree with each other.

Appendix A

Uncertainties of the probe position

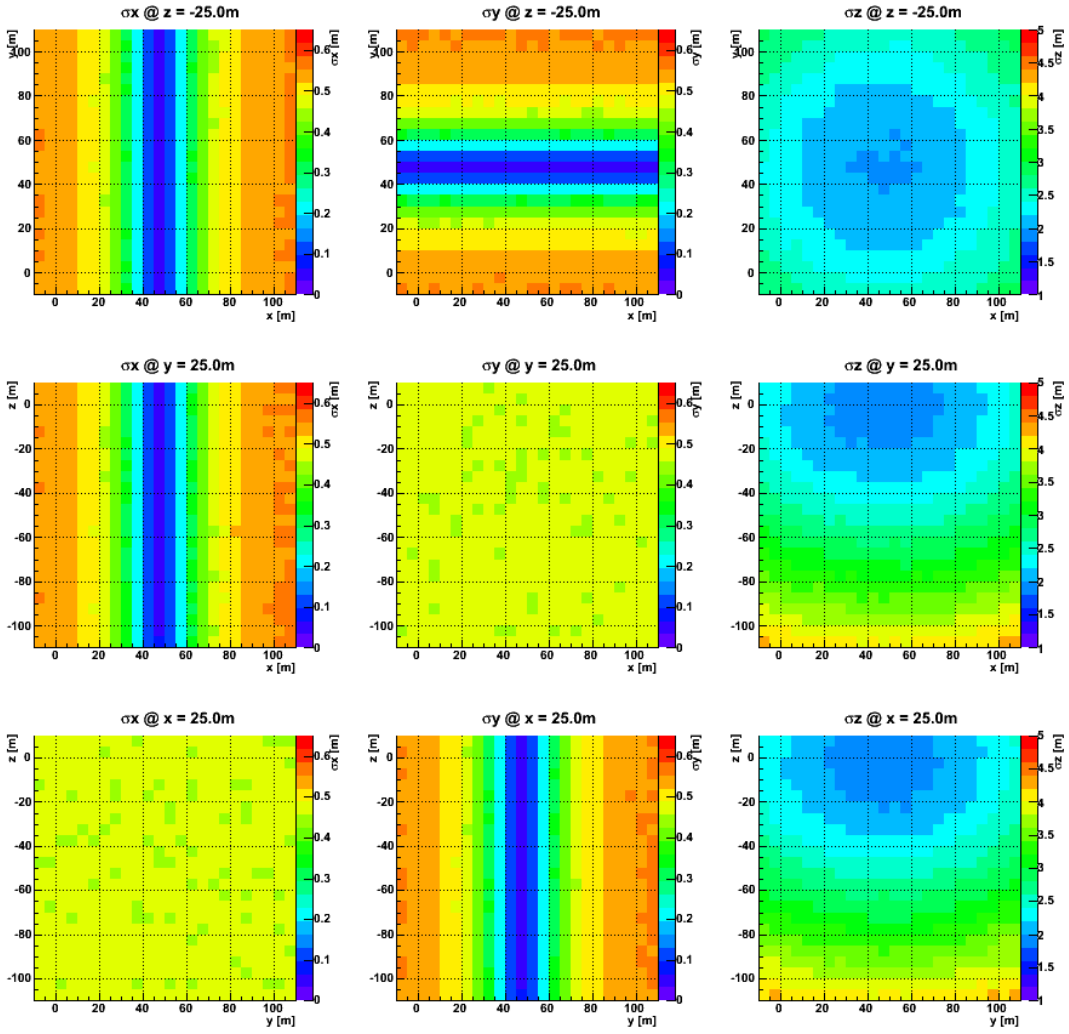

FIGURE A.1: Accuracy of the probes position depending on the position of the probe under the transducer array. The values of the uncertainties of transducer position, speed of sound and signal propagation time were the default values described in section 3.1.2. Each row shows the uncertaities of the probes coordinates in one plane. In the top row the z-coordinate was fixed at -25 m and in the rows below y- and x-coordinate were each fixed in the center of the array at 25 m.

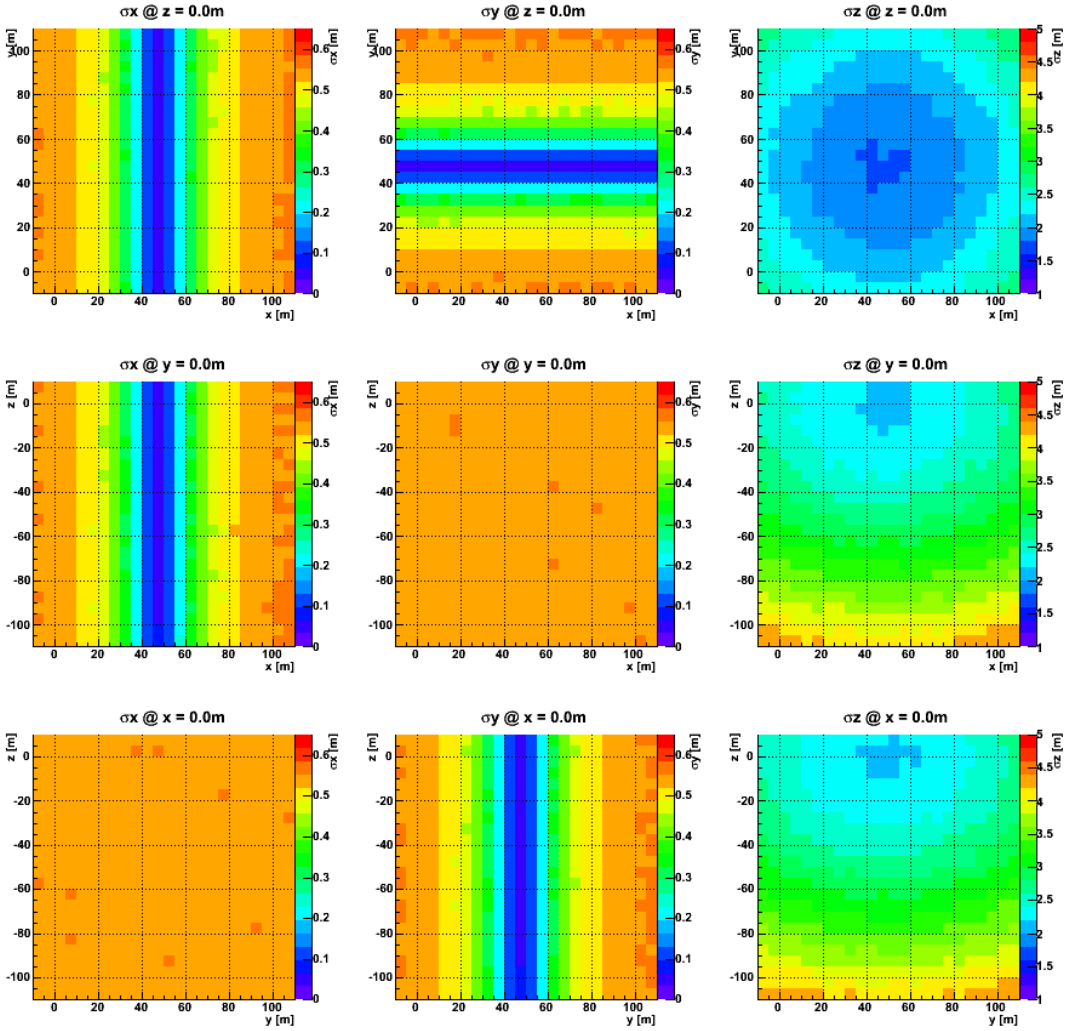

FIGURE A.2: Accuracy of the probes position depending on the position of the probe under the transducer array. The values of the uncertainties of transducer position, speed of sound and signal propagation time were the default values described in section 3.1.2. Each row shows the uncertaities of the probes coordinates in one plane. In the top row the z-coordinate was fixed at 0 m and in the rows below y- and x-coordinate were each fixed in the center of the array at 0 m.

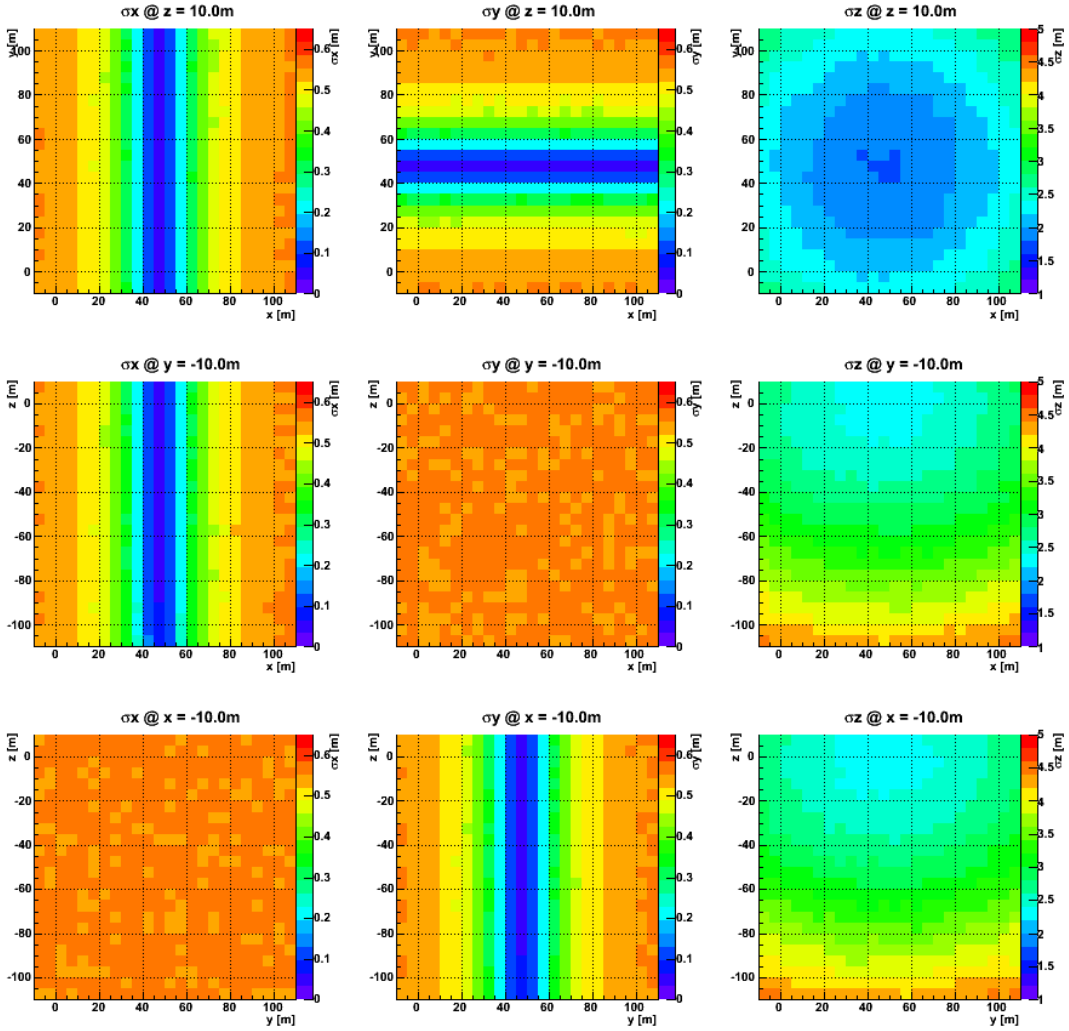

FIGURE A.3: Accuracy of the probes position depending on the position of the probe under the transducer array. The values of the uncertainties of transducer position, speed of sound and signal propagation time were the default values described in section 3.1.2. Each row shows the uncertaities of the probes coordinates in one plane. In the top row the z-coordinate was fixed at -10 m and in the rows below y- and x-coordinate were each fixed in the center of the array at -10 m.

Appendix B

Correction factors

TABLE B.1: Correction factors obtained from the transmitting frequency response of the ITC-1001.

Frequency [kHz]	Voltage Response [dB *re* µPa/V @ 1 m]	Correction factor
3	115	1.2783
4	120	1.2250
5	123	1.1951
6	127	1.1575
7	129	1.1395
8	131	1.1221
9	133	1.1053
10	135	1.0889
11	137	1.0730
12	138	1.0652
13	140	1.0500
14	143	1.0280
15	145	1.0138
16	146	1.0068
17	147	1.0000
18	148	0.9932
19	147	1.0000
20	146	1.0068

TABLE B.2: Correction factors of the transmitting direction of all FTUs.

f [kHz]	FTU 1	FTU 2	FTU 3	FTU 4	FTU 5	FTU 6	FTU 7
3	1.9833	1.9479	1.6087	2.6940	1.8977	1.2555	1.9513
4	1.7735	1.7633	2.9859	2.3647	1.7015	1.1456	1.7424
5	1.6592	1.6409	1.9558	2.2189	1.5820	1.0640	1.6184
6	1.4244	1.4114	2.1763	1.6645	1.3459	0.9605	1.2825
7	1.1382	1.1290	3.5144	1.1796	0.9585	0.7778	0.9452
8	0.9456	0.9409	2.0261	0.9594	0.7661	0.6591	0.7646
9	0.7936	0.7916	2.0801	0.8269	0.6719	0.5584	0.6516
10	0.6557	0.6569	1.3608	0.6579	0.5869	0.4709	0.5435
11	0.5494	0.5509	1.5151	0.5526	0.5298	0.3971	0.4920
12	0.4965	0.4976	1.1500	0.5372	0.4802	0.3553	0.4931
13	0.5232	0.5211	1.1634	0.5980	0.5143	0.3750	0.5139
14	0.6435	0.6363	1.5083	0.7506	0.6272	0.4526	0.6259
15	0.8071	0.7988	2.2263	0.9511	0.7862	0.5568	0.8012
16	1.0169	1.0000	2.7763	1.2024	0.9836	0.6820	1.0052
17	1.2075	1.2051	1.8548	1.6255	1.1823	0.8142	1.2017
18	1.4698	1.4593	2.9443	2.1232	1.4258	0.9736	1.4550
19	1.8303	1.8289	3.6295	2.5870	1.7757	1.1804	1.8337
20	2.3810	2.3903	2.4544	3.5054	2.2937	1.4688	2.3768

TABLE B.3: Correction factors of the receiving direction of all FTUs.

f [kHz]	FTU 1	FTU 2	FTU 3	FTU 4	FTU 5	FTU 6	FTU 7
3	1.3234	1.0272	0.7935	1.5190	1.0905	1.3001	1.0489
4	1.0242	1.0118	0.8343	1.1675	1.0519	1.2746	1.0327
5	0.8437	1.0088	0.7798	0.9501	1.0348	1.2333	1.0254
6	0.7318	0.9864	0.7731	0.8207	1.0390	1.1934	1.0186
7	0.6532	0.9830	0.7532	0.7272	1.0151	1.1558	1.0218
8	0.6019	0.9997	0.6902	0.6630	1.0199	1.1318	1.0243
9	0.5637	0.9992	0.6908	0.6150	1.0179	1.1190	1.0207
10	0.5346	0.9955	0.6841	0.5755	1.0069	1.1277	1.0135
11	0.5144	0.9957	0.6458	0.5502	1.0065	1.1513	1.0276
12	0.5011	0.9903	0.6393	0.5312	1.0248	1.1895	1.0263
13	0.4915	1.0101	0.6149	0.5160	1.0179	1.2396	1.0261
14	0.4839	0.9679	0.6173	0.5044	1.0194	1.2958	1.0278
15	0.4783	0.9973	0.5987	0.4987	1.0422	1.3537	1.0249
16	0.4773	1.0000	0.5815	0.4948	1.0384	1.4067	1.0091
17	0.4778	0.9885	0.5670	0.4918	1.0313	1.4723	1.0279
18	0.4778	0.9892	0.5657	0.4905	1.0197	1.5256	1.0246
19	0.4820	1.0145	0.5807	0.4926	1.0298	1.5719	1.0305
20	0.4856	1.0043	0.5511	0.4941	1.0383	1.6171	1.0276

Appendix C

Scan IceMole-Head

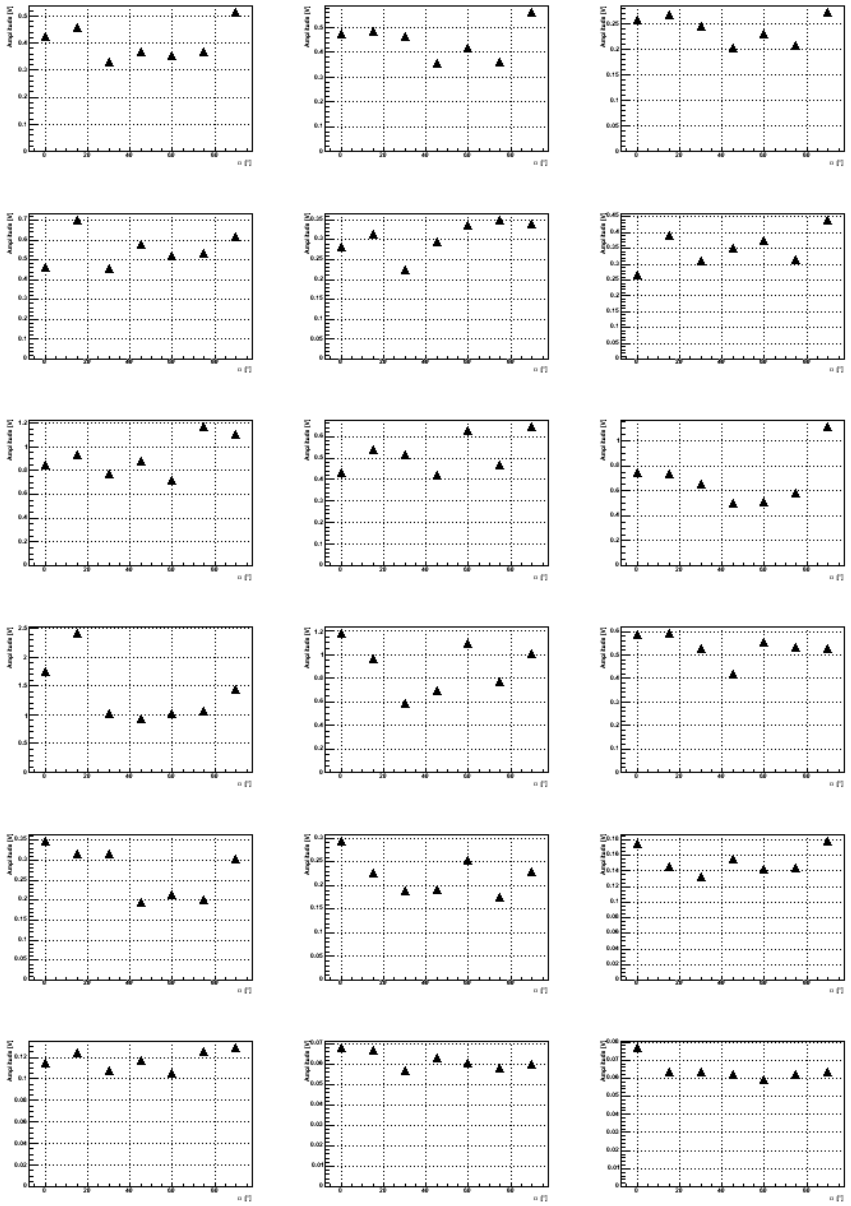

FIGURE C.1: Horizontal scan of the IceMole-Head for frequencies between 3 kHz and 20 kHz. In each plot the amplitudes for all measured angles for one frequency is shown.

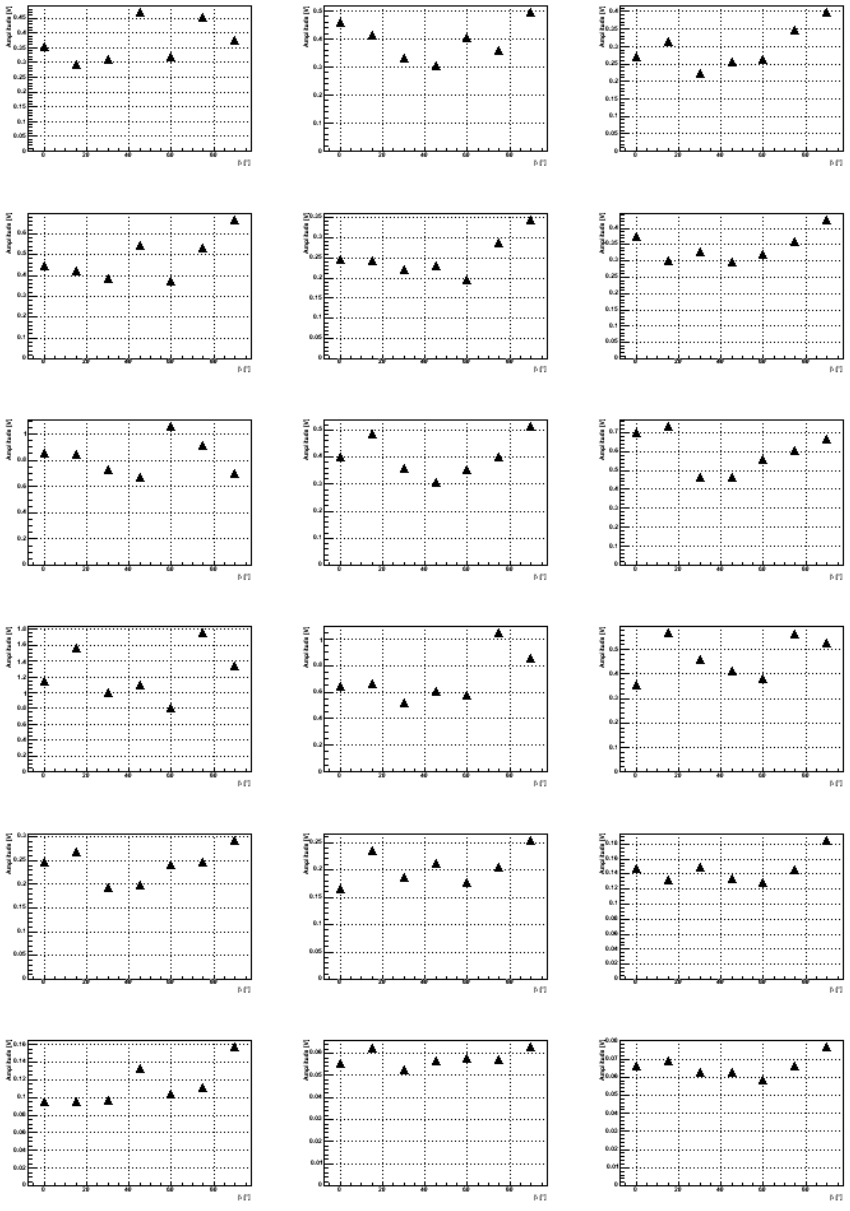

FIGURE C.2: Vertical scan of the IceMole-Head for frequencies between 3 kHz and 20 kHz. In each plot the amplitudes for all measured angles for one frequency is shown.

Appendix D

Freezing process measuring times

TABLE D.1: Measuring times of the data recorced during the freezing process in the laboratory.

Data ID	Time
1	00:00
2	00:40
3	01:30
4	03:10
5	04:50
6	05:10
7	06:10
8	07:30
9	08:30
10	08:40
11	27:30
12	30:50

Appendix E

Additional speed of sound plots

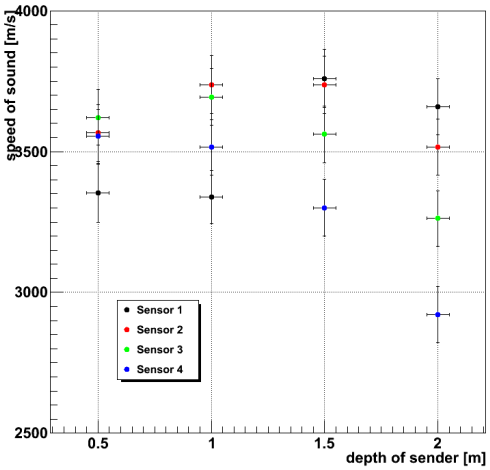

FIGURE E.1: Speed of sound for different insertion depth of the emitter in hole 3 for fixed insertion depth of the 4 receivers in hole 0 during field test 0.0 at a frequency of 30 kHz.

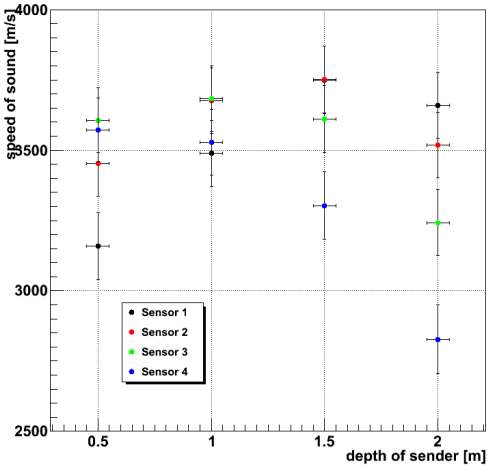

FIGURE E.2: Speed of sound for different insertion depth of the emitter in hole 3 for fixed insertion depth of the 4 receivers in hole 1 during field test 0.0 at a frequency of 30 kHz.

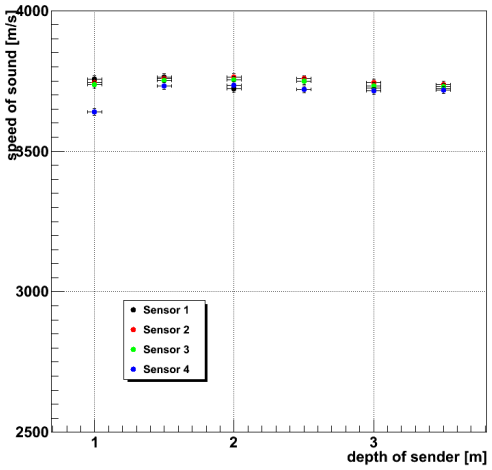

FIGURE E.3: Speed of sound for different insertion depth of the emitter in hole 2 for fixed insertion depth of the 4 receivers in hole 4 during field test 0.0 at a frequency of 30 kHz.

Bibliography

[1] *Cassini Solstice Mission: Galleries.* http://saturn.jpl.nasa.gov/photos/?subCategory=22. Accessed: 2015-09-22.

[2] CICLOPS, *Jet Spots in Tiger Stripes*, Mar., 2008. http://www.ciclops.org/view.php?id=4917.

[3] C. Porco, D. DiNino, and F. Nimmo, "How the geysers, tidal stresses, and thermal emission across the south polar terrain of Enceladus arerelated," *The Astronomical Journal* **148** no. 3, (July, 2014) . http://dx.doi.org/10.1088/0004-6256/148/3/45.

[4] J. Kowalski *et al.*, "Navigation Technology for Exploration of Glacier Ice With Maneuverable Melting Probes," *Cold Regions Science and Technology* **123** (Mar, 2016) 53–70.

[5] H. Niedermeier *et al.*, "Navigation system for a research ice probe for antarctic glaciers," *Position, Location and Navigation Symposium - PLANS 2014* (2014) . http://ieeexplore.ieee.org/xpl/articleDetails.jsp?arnumber=6851461.

[6] C. Espe, "Internal Note.".

[7] International Transducer Corporation, *Model ITC-1001 Spherical Omnidirectional Transducer*, Nov., 2016. http://pdf.directindustry.com/pdf/international-transducer/itc-1001/25344-402773.html.

[8] J. B. Plescia and J. M. Boyce, "Crater numbers und geological histories of Iapetus, Enceladus, Tethys and Hyperion," *Nature* **301** no. 5902, (Feb, 1983) 666–670.

[9] C. Porco *et al.*, "Cassini Observes the Active South Pole of Enceladus," *Science* **311** no. 5766, (Mar., 2006) 1393–1401. https://science.sciencemag.org/content/311/5766/1393.

[10] S. J. Peale, "Tidally induced volcanism," *Celestial Mechanics and Dynamical Astronomy* **83** no. 1/2, (2003) 129–155.

[11] G. Schubert *et al.*, "Enceladus: Present internal structure und differentiation by early und long- term radiogenic heating," *Icarus* **188** no. 2, (June, 2007) 345–355.

[12] NASA Press Release, "Cassini Tastes Organic Material at Saturn's Geyser Moon," March, 2008. https://www.nasa.gov/mission_pages/cassini/media/cassini-20080326.html.

[13] "NASA Solar system exploration: Enceladus." http://solarsystem.nasa.gov/planets/enceladus/facts. Accessed: 2015-09-23.

[14] R. C. Durst, P. D. Feighery, and K. L. Scott, "Why not use the standard internet suite for the interplanetary Internet," *Interplanetary Networking Special Interest Group* (2000) . http://www.ipnsig.org/reports/TCP_IP.pdf.

[15] *Wikipedia Außerirdisches Leben*. https://de.wikipedia.org/wiki/Au%C3%9Ferirdisches_Leben. Accessed: 2019-06-19.

[16] A. Wolszczan and D. A. Frail, "A planetary system around the millisecond pulsar PSR1257 + 12," *Nature* **355** (Jan., 1992) 145–147.

[17] *Exoplanet catalog*. http://exoplanet.eu/catalog. Accessed: 2015-10-07.

[18] *SETI Institute*. http://www.seti.org. Accessed: 2015-09-23.

[19] *James Webb Space Telescope*. http://jwst.nasa.gov/science.html. Accessed: 2015-10-05.

[20] C. F. Chyba and K. P. Hand, "ASTROBIOLOGY: The Study of the Living Universe," *Annu. Rev. Astron. Astrophys.* **43** no. 2, (Apr., 2005) 1–44.

[21] N. Kitadai and S. Maruyama, "Origins of building blocks of life: A review," *Geoscience Frontiers* (2018) 1117–1153. https://www.sciencedirect.com/science/article/pii/S1674987117301305?via%3Dihub.

[22] National Research Council, *The Limits of Organic Life in Planetary Systems*. Washington, DC, 2007. https://www.nap.edu/catalog/11919/the-limits-of-organic-life-in-planetary-systems.

[23] *Encyclopaedia Britannica: Habitable zone*, Nov., 2015. https://www.britannica.com/science/habitable-zone. Accessed: 2015-11-13.

[24] D. P. Cruikshank, "Near-infrared studies of the satellites of Saturn and Uranus," *ICARUS* **41** no. 2, (1980) 246–258.

[25] A. J. Verbiscer, R. G. French, and C. A. McGhee, "The opposition surge of Enceladus: HST observations 338-1022 nm," vol. 173, pp. 66–83. Jan., 2005.

[26] *Cassini Solstice Mission*. http://saturn.jpl.nasa.gov/science/moons/enceladus. Accessed: 2015-09-22.

[27] J. S. Kargel and S. Pozio, "The Volcanic and Tectonic History of Enceladus," *ICARUS* **116** no. 2, (Feb., 1996) 385–404.

[28] J. R. Spencer, J. C. Pearl, M. Segura, F. M. Flasar, A. Mamoutkine, P. Romani, B. J. Buratti, A. R. Hendrix, L. J. Spilker, and R. M. C. Lopes3, "Cassini Encounters Enceladus: Background and the Discovery of a South Polar Hot Spot," *Science* **311** no. 5766, (Mar., 2006) 1401–1405.

[29] R. H. Brown *et al.*, "Composition and Physical Properties of Enceladus' Surface," *Science* **311** no. 5766, (Mar., 2006) 1425–1428.

[30] S. Charnoz, L. Dones, L. W. Esposito, P. R. Estrada, and M. M. Hedman, *Origin and Evolution of Saturn's Ring System*, ch. 17, pp. 537–575. 2009.

[31] Committee on Principles of Environmental Stewardship for the Exploration and Study of Subglacial Environments, Polar Research Board, and Division of Earth and Life Studies, "Exploration of antarctic subglacial aquatic environments: Environmental and Scientific Stewardship," *THE NATIONAL ACADEMIES PRESS* (2007) .

[32] Norththrop Grumman, *LN-200 FOG Family*, Jan., 2016.

[33] C. J. Harvey, J. M. Pilcher, R. J. Eckersley, M. J. Blomley, and D. O. Cosgrove, "Advances in Ultrasound," *Clinical Radiology* **57** no. 3, (Mar., 2002) 157–177.

[34] J. A. Jensen, "Medical ultrasound imaging," *Progress in Biophysics and Molecular Biology* **93** no. 1-3, (Jan., 2007) 153–165.

[35] B. W. Drinkwater and P. D. Wilcox, "Ultrasonic arrays for non-destructive evaluation: A review," *NDT & E International* **39** no. 7, (Oct., 2006) 525–541.

[36] U. Naumann, "Internal Note." Oct, 2012.

[37] William S. Murphy Jr. and W. Hereman, "Determination of a position in three dimensions using trilateration an approximate distances,". http://inside.mines.edu/~whereman/papers/Murphy-Hereman-Trilateration-1995.pdf.

[38] R. Lerch, G. M. Sessler, and D. Wolf, *TechnischeAkustik*. Springer, 2009.

[39] O. S. University, "Explanation Offered For Antarctica's 'Blood Falls'," *ScienceDaily* (Nov., 2003) .

[40] R. F. Black, M. L. Jackson, and T. E. Berg, "Saline Discharge from Taylor Glacier, Victoria Land, Antarctica," *The Journal of Geology* **73** no. 1, (Jan., 1965) 175–181. http://www.jstor.org/stable/30066388.

[41] A. Hubbard *et al.*, "Evidence for subglacial ponding across Taylor Glacier, Dry Valleys, Antarctica," *Ann. Glaciol.* **39** (2004) 79–84.

[42] J. A. M. et al., "A contemporary microbially maintained subglacial ferrous "ocean"," *Science* **324** no. 5925, (April, 2009) 397–400.

[43] J. A. Mikucki and J. C. Priscu, "Bacterial Diversity Associated with Blood Falls, a Subglacial Outflow from the Taylor Glacier, Antarctica," *Applied and Environmental Microbiology* **73** no. 12, (June, 2007) 4029–4039.

[44] D. Pollard and R. M. DeConto, "Modeling West Antarctic ice sheet growth and collapse through the past five million years," *Nature* **458** (Mar., 2009) 329–332.

[45] J. A. Mikucki, C. M. Foreman, B. Sattler, W. B. Lyons, and J. C. Priscu, "Geomicrobiology of Blood Falls: An Iron-Rich Saline Discharge at the Terminus of the Taylor Glacier, Antarctica," *Aquatic Geochemistry* **10** (2004) 199–220.

[46] W. B. Lyons *et al.*, "Groundwater seeps in Taylor Valley Antarctica: an example of a subsurface melt event," *Annals of Glaciology* **40** no. 1, (Jan., 2005) 200–206(7).

[47] B. Semburg, *HADES - an acoustic sensor for neutrino detection in ice*. PhD thesis, Feb., 2011.

[48] Sensor Technology LTD, *SQ09 Transmit/Receive Hydrophones*, 2012.

[49] H. Kuchling, "Taschenbuch der Physik,".

[50] A. Kundert, *Winfilter*. http://www.winfilter.20m.com.

[51] D. F. Elliott, ed., *Handbook of Digital Signal Processing*. Academic Press, San Diego, 1987. http://www.sciencedirect.com/science/article/pii/B9780080507804500217.

[52] B. E. Treeby and B. T. Cox, "k-Wave: MATLAB toolbox for the simulation and reconstruction of photoacoustic wave-fields," *J. Biomed. Opt.* **15** no. 2, (2010) 021314.

[53] B. Treeby, B. Cox, and J. Jaros, *k-Wave User Manual*, Nov, 2015. http://www.k-wave.org/manual/k-wave_user_manual_1.0.1.pdf.

[54] J. H. Justice, "Analytic Signal Processing in Music Computation," *IEEE Transactions on Acoustics, Speech, and Signal Processing* **27** no. 6, (Dec., 1979) 670–684.

[55] D. Zwillinger, "Standard Mathematical Tables and Formulae," *CRC Press LLC* (2003) 399–402.

[56] S. Zierke, *Entwicklung eines Verfahrens zur akustischen Ortsbestimmung einer Einschmelzsonde für die Suche nach außerirdischem Leben auf dem Saturnmond Enceladus*. PhD thesis, 2019.

Acknowledgement

This work would not have been possible without the help and encouragement of a lot of people.

First of all, I want to thank Prof. Dr. Klaus Helbing for giving me the opportunity to be part of the Astroparticle group Wuppertal and to work in this interesting project. Besides his active support, especially during field tests, I appreciated his patience towards the end of my thesis.

I am grateful to Prof. Dr. Gisela Anton for accepting to be the second reviewer of this work.

Many thanks to Uwe Naumann for his continuous technical support and many fruitful discussions on the design of the system. It has always been a pleasure working with him.

Furthermore, I want to thank Frederik Lauber, Stephanie Hickford and Eric Mayotte for their valuable input while proofreading this thesis and for the comments and discussions that were very helpful to clearify some topics.

I am also thankful to Ingrid Schaarwächter for her support in all administrative matters and for always having an open ear, even beyond work related topics.

To all colleages from the Astroparticle group I am grateful for the great working atmoshere and many pleasent hours full of discussions during Mettings, BBQs and coffee breaks. I am glad I got to meet you all and happy to have found many friends among you.

Last but not least I want to thank my friends and family for their encouragement and patience in the last few months. Especially I am grateful to Sven, who always has my back, for his support and for not holding my mental absence in the last few months against me.